Cold Atom Interferometry for enhancing the Radio Science gravity experiment

A Phobos case study

Michael Plumaris

Technische Universiteit Delft

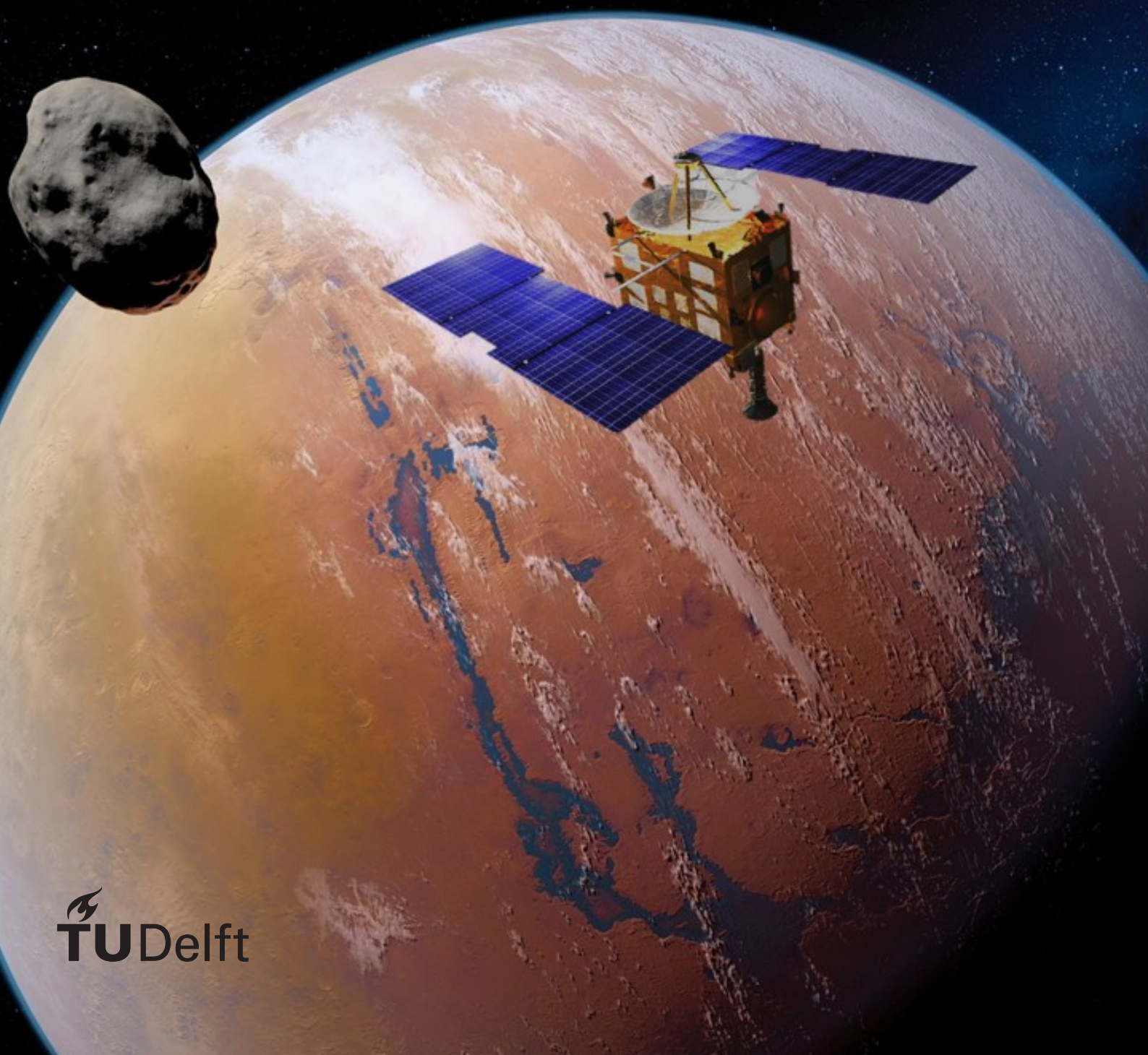

TU Delft

Cold Atom Interferometry for enhancing the Radio Science gravity experiment

A Phobos case study

by

Michael Plumaris

to obtain the degree of Master of Science
at the Delft University of Technology,
to be defended publicly on Monday December 20, 2021 at 9:00 AM.

Student number:	4537629	
Project duration:	April 4^{th}, 2021 – December 6^{th}, 2021	
Thesis committee:	Prof. dr. L.L.A. Vermeersen	Committee chair
	Dr. ir. C. Siemes,	Supervisor
	Dr. ir. D. Dirkx,	Supervisor
	Dr. A. Menicucci	External examiner
	Dr. O. Carraz	Additonal examiner

An electronic version of this thesis is available at http://repository.tudelft.nl/.

The cover image is an artist impression of Phobos in the foreground of Mars (image credit: Picture Press RM) and the Hayabusa spacecraft (image credit: JAXA)

TU Delft

Preface

This thesis represents the closing piece of my life as a student at the TU Delft. Throughout these five years I have met some truly inspirational people whom I would like to thank, as they have made this journey a thoroughly enjoyable one.

My deepest appreciation goes to Christian and Dominic, the best supervisor duo I could have asked for. Thank you for your constructive (and complementary) feedback, your encouragement, your understanding but especially for the time you dedicated to guiding my future steps. Whatever ends up happening, I will never forget the trust and opportunities you have given me. You have truly inspired me to pursue academic research, and I one day hope to be fostering education and scientific exploration as you do.

I would like to thank Olivier C. for guiding me through the maze of Cold Atom Interferometry and for arranging visits to ESTEC in spite of the difficult situation, as they have been definitively worthwhile. I am also grateful to Olivier W. for the guidance in selecting the most promising candidate for my mission. I'm sorry Enceladus didn't make it, but perhaps we shall see a comeback in the near future. Finally, I am thankful to Sebastien for his valuable insight on this complex yet fascinating moon. I feel truly privileged for the guidance offered by this team of experts.

Speaking of experts, I have to spare a word for the experts in distraction and amusement: Tommi, Marta, Fede, Lavi, Ludo, I am grateful for having you in my life ever since I was 6 years old. Thank you (space) Jonas and Guido for the good times we shared inside and outside the Faculty. I would also like to thank my housemates for your emotional support and comforting welcome, especially (Earth) Jonas and Kevin for your cheeky humour and devotion to sports, and Gaia for your laid back attitude. Andrea, thank you for reminding me of the important things in life, and for the rest as well.

Thank you to my parents for your unwavering love and support. I am appreciative for your patience in listening to my progress, in spite of you having little to no clue of what I'm saying. Thank you Gala for being like a sister to me. Thank you Giorgio for your extraordinary and playful nature. Finally, thank you to my grandmother for always encouraging me as best you can. Come sai, sei la migliore (e unica) nonna che ho.

Michael Plumaris
Delft, December 2021

Abstract

This thesis aims to consolidate the growing potential of inertial sensors based on Cold Atom Interferometry (CAI) with the desire to explore small bodies in the solar system. It follows the conceptual study carried out at the European Space Agency, during which the Martian moon Phobos was identified as the most suitable candidate for a pioneering CAI mission. CAI-based Gradiometry (CG) was selected to strengthen the Radio Science (RS) experiment for gravity field recovery. This would provide key evidence in constraining Phobos elusive origin, thus contributing to our understanding of terrestrial moons and of the solar system as a whole.

Keplerian orbits are prohibited by Mars dynamical dominance, hence quasi-satellite orbits were sought as means of orbiting Phobos in the relative sense. Their robustness with regards dynamical model uncertainties and the associated maintenance budgets to avert crash or escape were evaluated. The tracking observables and gradiometry measurements were simulated for a mission duration of one week. A covariance analysis was adopted to evaluate the contribution of RS and CG in the gravity field solution. The favourable observational geometry and the small characteristic period of the gravity signal add to the competitiveness of Doppler observables. Provided that empirical accelerations can be modelled below the nm/s^2 level, RS is able to infer the 6x6 spherical harmonic spectrum to an accuracy of 0.1-1% w.r.t. the homogeneous interior values. If this correlates to a density anomaly beneath the Stickney crater, RS would suffice to constrain Phobos' origin. Yet, in event of a rubble pile or icy moon interior (or a combination thereof) CG remains imperative, enabling an accuracy below 0.1% for most of the 10x10 spectrum. Nevertheless, technological advancements will be needed to alleviate the current logistical challenges associated with CG operation. Finally, by resolving C_{20} & C_{22} and providing an independent estimate for libration, the proposed mission strategy is set to enhance Phoboss ephemeris via dynamical fitting. This would facilitate a return to the moon and provide additional clues on its orbital evolution.

The dynamical environment of Phobos is quite extreme, but in many ways similar to that of other small moons. Hence the methodology outlined in this work may serve as a foothold to contemplate the role of CG in bolstering the geodesic investigation of future exploratory missions to small moons, particularly those of the Giant planets, which are targets for robotic exploration in the coming decades.

Contents

Nomenclature

Abbreviations and Acronyms

ABM	Adams-Bashforth-Moulton
BS	Burlich-Stoer
CAI	Cold Atom Interferometry
DP	Dormand Prince
CG	CAI-based Gradiometry
CoM	Centre of Mass
GMEE	Gauss Modified Equinoctial Elements
GOCE	Gravity field and steady-state Ocean Circulation Explorer
MMX	Martian Moons Exloration
MEX	Mars Express
MoI	Moments of Inertia
MOT	Magneto-Optical Trap
PF	Pareto Front
QSO	Quasi-Satellite Orbits
RK	Runge-Kutta
RFK	Runge-Kutta-Fehlberg
RS	Radio Science
TRL	Technological Readiness Level
USM-EM	Unified State Model - Exponential Map
USM-MRP	Unified State Model - Modified Rodrigues Parameters
USM-Q	Unified State Model - Quaternions
VLBI	Very-Long Baseline Interferometry

Reference Frames

BFF	Body-Fixed (Reference) Frame
GRF	Gradiometer Reference Frame
IRF	Inertial Reference Frame
LNOF	Local North-Oriented (Reference) Frame

Latin Symbols

C_r	Radiation pressure coefficient [-]
C_{nm}, S_{nm}	Spherical harmonic coefficients [-]
d	Baseline separation [m]
$\overline{euc}$	Coverage index [-]
GM	Gravitational parameter [$m^3.s^{-2}$]
h	Integrator step size [s]
$\boldsymbol{H}$	Partials matrix
$\boldsymbol{H_c}$	Partials matrix for the consider parameters
I_{xyz}	Moment of Inertia [$kg.m^2$]
k	Effective wave vector [m^{-1}]
k_2	Degree 2 Love number [-]
k_b	Boltzmann constant [$m^2kg.s^{-2}K-1$]
m	Harmonic order [-]
m_{at}	Atomic mass [kg]
n	Harmonic degree [-]
p	Porosity [-]
$\boldsymbol{P}$	Covariance matrix
$\boldsymbol{P_C}$	Consider covariance matrix
$\overline{P}_{nm}$	Normalised Legendre functions [-]
R	Reference radius [m]
r	Orbital radius [m]
$\boldsymbol{r}$	Position vector [m]
t_m	Measurement time [s]
t_{int}	Integration time for Doppler data [s]
T_k	Atomic temperature [K]
T	CAI interrogation time [s]
T_c	Characteristic period [s]
$\boldsymbol{v}$	Velocity vector [$m.s^{-1}$]
V	Gravitational potential [J]
V_{xx}	Gravity gradient along x axis[s^{-2}]
$\boldsymbol{v}_t$	Transverse velocity [$m.s^{-1}$]
$\boldsymbol{v}_{rec}$	Recoil velocity [$m.s^{-1}$]
$\boldsymbol{W}$	Weights matrix

Greek symbols

θ	Longitudinal libration [deg]
θ_m	Tilt mirror actuation angle
λ	Longitude [deg]
λ_n	Stability index [-]
ρ	Density [$kg.m^{-3}$]
$\hat{\rho}$	Radial unit vector
σ	Formal error
σ_γ	Gradiometric sensitivity [$s^{-2}.\sqrt{Hz}$]
$\sigma_{\Delta\phi}$	Sensitivity to phase readouts [rad]
σ_ρ	Range data accuracy [m]
$\sigma_{\dot{\rho}}$	Doppler data accuracy [$m.s^{-1}$]
$\boldsymbol{\Phi}$	State transition matrix
ϕ	Latitude [deg]
ϕ_{acc}	Accumulated phase shift [rad]
Ω_{orb}	Orbital frequency [$rad.s^{-1}$]
Ω_{xyz}	Orbital frequency around axis [$rad.s^{-1}$]
Ω_m	Orbital frequency of tilt mirror [$rad.s^{-1}$]
Ω_{sid}	Sidereal period [$rad.s^{-1}$]

1

Introduction

Gravity field measurements play a fundamental role in exploratory missions to small bodies, insofar as they help predict their dynamical behaviour and -in combination with shape models- reveal their internal mass distribution, shedding light on formation theories leading to their accretion (Lissauer and de Pater, 2013). This is especially true for irregular bodies with high degrees of interior heterogeneity, whereby a thorough description of the gravity field is needed to execute proximity operations. Radio Science (RS) stands out as the established method for interplanetary gravity recovery via detection of its gravitational signatures on the spacecraft's trajectory. Nonetheless, the weak signatures of small bodies, coupled with the prominent influence of confounding accelerations hinder the attainable resolution of the gravity field solutions.

Ongoing maturement in quantum technology (Bongs et al., 2019 and references therein) has promoted Cold Atom Interferometry (CAI) as a strong contender for the next generation of gravity sensors (Haagmans et al., 2020). Leveraging on the wave-particle duality of atoms, CAI uses quantum interference to measure their reactivity to inertial forces. The sensitivity scales quadratically with the measurement time, which is drastically extended in microgravity as the atoms are in free-fall. This has encouraged numerical studies assessing their potential as spaceborne gravity gradiometers (Carraz et al., 2014; Douch et al., 2018; Trimeche et al., 2019) benchmarking the recovered gravity field solution to that obtained via the Gravity field and steady-state Ocean Circulation Explorer (Rummel et al., 2010). In fact, GOCE has highlighted the main drawbacks of electrostatic-based gradiometers, notably their poor accuracy at low frequencies and their complex time-varying calibration (Siemes et al., 2019). These issues are mitigated with CAI-based Gradiometry (CG) as its working principle and lack of mechanical parts guarantee absolute measurements with an intrinsic long-term stability and repeatability, suppressing the need for re-calibration (Barrett et al., 2014).

In light of the above considerations, Phobos is examined as a science case for a thorough gravity field investigation. Astronomical observations and the RS experiments from Mars EXpress (MEX) flybys in 2010 and 2013 (Witasse et al., 2014) provided constraints for Phobos' mass (Pätzold et al., 2014) and topography (Willner et al., 2014), with the corresponding density suggesting a fractured and porous moon filled with either water-ice or voids or a combination thereof. These clues prompted studies (Dmitrovskii et al., 2022; Guo et al., 2021; LeMaistre et al., 2019; Yang et al., 2019) linking its geodesic observables to various formation hypotheses. Indeed, the origin of Phobos -and its twin Deimos- remains elusive, with hypotheses of an asteroidal capture (Pajola et al., 2013), disruption of a common parent (Bagheri et al., 2021, co-accretion (Safranov et al., 1986), or post-collisional re-accretion of ejecta material (Canup and Salmon, 2018). Ambiguities associated with each theory make it impossible to converge towards a definite answer, yet the latter would contribute to our understanding of terrestrial moons and of the solar system as a whole (Rosenblatt, 2011). Moreover, in the prospect of human explorer missions projected for the 2030s, these moons could serve as staging bases for refuelling transiting spacecraft, teleoperating critical machinery and developing habitable infrastructure ahead of planetary landings (Nallapu et al., 2020). In essence, Phobos' physical properties are known just well enough to define a mission strategy, whilst maintaining strong grounds for a geodesic investigation. Its small-body nature suggests that CG can significantly bolster the RS gravity field solution, and therefore constitutes a suitable framework for this study.

It is worth mentioning that the Japanese Martian Moons Exploration (MMX) mission (Campagnola et al., 2018), envisaged for launch in 2024, plans to explore Phobos and return >10g of regolith material just >2cm beneath the surface (Usui et al., 2020). Nonetheless, the MMX instrument configuration is geared towards

remote observations rather than geodesic sensing. And whilst a detailed laboratory sample analysis might pinpoint the most likely formation hypothesis, it is unclear whether such samples will be representative for the entire body. In fact, different spectra (red and blue) have been observed on the two hemispheres of Phobos (Rosenblatt, 2011) which could be attributed to spatial/compositional variations in its surface properties or perhaps to a fine layer of alien material (Pieters, 2010). Hence, detailed measurements of its deep interior will serve to interlink MMX's remote and in-situ observations to paint a more comprehensive picture of Phobos' origin.

1.1. Research Questions

This research aims to investigate the potential of CG in strengthening the RS experiment for gravity field recovery of small bodies, using Phobos as a science case. To this end, the main research question is formulated as follows: **Leveraging on the advantages entailed by small-body environments for Gradiometers based on Cold Atom Interferometry, to what extent can these instruments strengthen the radio science geodesic experiment to constrain Phobos origin?** This has been partitioned into numerous sub-questions, serving as guidelines to the research effort:

- **Given Phobos' challenging dynamical environment, what are the possible orbital strategies, and how do these rank in terms of maintainability?**
- **How does the choice of orbit influence the geodesic solution obtained via RS and CG?**
- **To what extent can RS alone constrain Phobos' origin?**
- **What is the optimal CG instrument configuration to reinforce the geodesic solution obtained via RS?**
- **Based on the present study, is it possible to draw generic conclusions on the applicability of CG in other small-body missions?**

1.2. Report Outline

The core of this thesis is written in the form of a journal paper available in Chapter 2. The extensive answers to the research questions and recommendations for future work follow in Chapter 3. The choice of numerical integrators and propagators has been justified in Appendix A. The steps taken to validate the adopted methodology are outlined in Appendix B. Finally, the orbit sensitivity analysis and the associated maintenance budgets are presented in Appendix C.

2

Journal Paper

The core of this thesis has been written in form of a journal paper. The manuscript is hereby provided using the required template.

Cold Atom Interferometry for enhancing the Radio Science gravity experiment: a Phobos case study

Michael Plumaris[a]

[a]*Delft University of Technology, Kluyverweg 1, Delft, 2629HS, , The Netherlands*

Abstract

Interplanetary missions have relied on Radio Science (RS) for recovering gravity fields via detecting their signature on the spacecraft's trajectory. Yet the weak gravitational fields of small bodies, coupled with the prominent influence of confounding accelerations, hinder the efficacy of this method. Meanwhile, quantum sensors based on Cold Atom Interferometry (CAI) have demonstrated absolute measurements with an inherent stability and repeatability, reaching the utmost accuracy in microgravity. This work addresses the potential of CAI-based Gradiometry (CG) as a means to strengthen the RS gravity experiment for small-body missions. Phobos represents an ideal science case as astronomic observations and recent flybys have conferred enough information to define a robust orbiting strategy, whilst promoting studies linking its geodesic observables to its origin. A covariance analysis was adopted to evaluate the contribution of RS and CG in the gravity field solution, for a mission duration of one week.

The favourable observational geometry and the small characteristic period of the gravity signal add to the competitiveness of Doppler observables. Provided that empirical accelerations can be modelled below the nm/s^2 level, RS is able to infer the 6x6 spherical harmonic spectrum to an accuracy of 0.1-1% w.r.t. the homogeneous interior values. If this correlates to a density anomaly beneath the Stickney crater, RS would suffice to constrain Phobos' origin. Yet, in event of a rubble pile or icy moon interior (or a combination thereof) CG remains imperative, enabling an accuracy below 0.1% for most of the 10x10 spectrum. Nevertheless, technological advancements will be needed to alleviate the current logistical challenges associated with CG operation. This work also reflects on the sensitivity of the candidate orbits with regards to dynamical model uncertainties, which are common in small-body environments. This brings confidence in the applicability of the identified geodetic estimation strategy for missions targeting other moons, particularly those of the Giant planets, which are targets for robotic exploration in the coming decades.

Keywords: Cold Atom Interferometry, Gravity gradiometry, Radio Science, Space geodesy, Phobos origin

1. Introduction

Gravity field measurements play a fundamental role in exploratory missions to small bodies, insofar as they help predict their dynamical behaviour and -in combination with shape models- reveal their internal mass distribution, shedding light on formation theories leading to their accretion (Lissauer and de Pater (2013)). This is especially true for irregular bodies with high degrees of interior heterogeneity, whereby a thorough description of the gravity field is needed to execute proximity operations. Radio Science (RS) stands out as the established method for interplanetary gravity recovery via detection of its gravitational signatures on the spacecraft's trajectory. Nonetheless, the weak signatures of small bodies, coupled with the prominent influence of confounding accelerations hinder the attainable resolution of the gravity field solutions.

Ongoing maturement in quantum technology (Bongs et al. (2019) and references therein) has promoted Cold Atom Interferometry (CAI) as a strong contender for the next generation of gravity sensors (Haagmans et al. (2020)). Leveraging on the wave-particle duality of atoms, CAI uses quantum interference to measure their reactivity to inertial forces. The sensitivity scales quadratically with the measurement time, which is drastically extended in microgravity as the atoms are in free-fall. This has encouraged numerical studies assessing their potential as spaceborne gravity gradiometers (Carraz et al. (2014); Douch et al. (2018); Trimeche et al. (2019)) benchmarking the recovered gravity field solution to that obtained via the Gravity field and steady-state Ocean Circulation Explorer (GOCE) (Rummel et al. (2010)). In fact, GOCE has highlighted the main drawbacks of electrostatic-based gradiometers, notably their poor accuracy at low frequencies and their complex time-varying calibration (Siemes et al. (2019)). These issues are mitigated with CAI-based Gradiometry (CG) as its working principle and lack of mechanical parts guarantee absolute measurements with an intrinsic long-term stability and repeatability, suppressing the need for re-calibration (Barrett et al. (2013)).

In light of the above considerations, Phobos is examined as a science case for a thorough gravity field investigation. Astronomical observations and the RS experiments from Mars EXpress (MEX) flybys in 2010 and 2013 (Witasse et al. (2014)) provided constraints for Phobos' mass (Pätzold et al. (2014)) and topography (Willner et al. (2014)), with the corresponding density suggesting a fractured and porous moon filled with

Email address: m.k.plumaris@student.tudelft.nl (Michael Plumaris)

either water-ice or voids or a combination thereof. These clues prompted studies (LeMaistre et al. (2019); Dmitrovskii et al. (2022); Guo et al. (2021); Yang et al. (2019)) linking its geodesic observables to various formation hypotheses. Indeed, the origin of Phobos -and its twin Deimos- remains elusive, with hypotheses of an asteroidal capture (Pajola et al. (2013)), disruption of a common parent (Bagheri et al. (2021), co-accretion (Safranov et al. (1986)), or post-collisional re-accretion of ejecta material (Canup and Salmon (2018)). Ambiguities associated with each theory make it impossible to converge towards a definite answer, yet the latter would contribute to our understanding of terrestrial moons and of the solar system as a whole (Rosenblatt (2011)). Moreover, in the prospect of human explorer missions projected for the 2030s, these moons could serve as staging bases for refuelling transiting spacecraft, teleoperating critical machinery and developing habitable infrastructure ahead of planetary landings (Nallapu et al. (2020)). In essence, Phobos' physical properties are known just well enough to define a mission strategy, whilst maintaining strong grounds for a geodesic investigation. Its small-body nature suggests that CG can significantly bolster the RS gravity field solution, and therefore constitutes a suitable framework for this study.

It is worth mentioning that the Japanese Martian Moons Exploration (MMX) mission (Campagnola et al. (2018)), envisaged for launch in 2024, plans to explore Phobos and return $>$10g of regolith material just $>$2cm beneath the surface (Usui et al. (2020)). Nonetheless, the MMX instrument configuration is geared for remote observations rather than geodesic sensing. And whilst a detailed laboratory sample analysis might pinpoint the most likely formation hypothesis, it is unclear whether such samples will be representative for the entire body. In fact, different spectra (red and blue) have been observed on the two hemispheres of Phobos (Rosenblatt (2011)) which could be attributed to spatial/compositional variations in its surface properties or perhaps to a fine layer of 'alien' material (Pieters (2010)). Hence, detailed measurements of its deep interior will serve to interlink MMX's remote and in-situ observations to paint a more comprehensive picture of Phobos' origin.

This work aims to investigate the potential of CG in strengthening the RS experiment for gravity field recovery of small bodies, using Phobos as a science case. Due to the challenging dynamical environment and different nature of the two experiments, a broad class of orbits is considered. A covariance analysis is adopted to evaluate the relative contribution of RS and CG in the gravity field solution, for a mission duration of one week. The manuscript is organised as follows. Section 2 provides an overview of the key geodesic measurements for constraining Phobos' interior. The dynamical model and orbit strategies are presented in Section 3, focussing on how the uncertainties associated with the former influence the robustness of the latter and the corresponding orbit determination solution. Section 4 summarises the principle of CAI and its implementation in two competing gradiometer concepts. The methodology used to assess the performance of RS and CG for gravity field recovery is outlined in Section 5. Finally, Section 6 presents the geodesic parameter accuracies for both methods and compares them to the imposed science goals. Section 7 draws upon the main conclusions for the current study.

The numerical simulations undertaken in this work have relied on the interlinking the *Tudat* software developed at the Astrodynamics & Space Missions department of the Delft University of Technology [1] and the code for processing GOCE' gravity gradiometry measurements, detailed in Siemes (2008).

2. Phobos Science Goals

Phobos is nearing Mars at a rate of 1.8m per century, meaning it will either crash into it in 50 million years, or, most likely, crumble into a ring of debris (Bagheri et al. (2021)). Before that happens, one must recollect the key geodesic observables to constrain its origin, and reflect on the clues provided by their current estimates. This will contextualise our understanding of the moon and guide the simulation setup.

2.1. Interior Models and Porosity

Rosenblatt (2011) scrutinise the evidence which prompted the development of conflicting theories on the origins of the Martian moons. Surface reflectance spectra match those of primitive low-albedo asteroids (Witasse et al. (2014); Pajola et al. (2013)) which have escaped from the belt. If these originate from beyond the snow line, water ice is expected to make up a significant part of the body, as is the case for Ceres (Konopliv et al. (2018)). Nonetheless, even in the presence of water ice, a capture scenario would require unexpectedly high tidal dissipation rates to account for their current near-circular, near-equatorial orbits around Mars. Bagheri et al. (2021) reinforce this hypothesis by combining geophysical and tidal-evolution modelling to propose that both moons originate from the disintegration of a common progenitor, that possibly formed in situ. This hypothesis is consistent with RS data from the 2013 MEX flyby (Pätzold et al. (2014)) which supports a high degree of porosity, a natural consequence of debris re-accretion at Mars' orbit. Perhaps, this is a case of post-collisional re-accretion of ejecta material from Mars itself (Canup and Salmon (2018)). In light of these arguments, LeMaistre et al. (2019) contrive four heterogeneous interiors for Phobos: a loosely-held *rubble pile* structure, a *heavily fractured* interior, a *porous compressed* family or an *icy moon*. Phobos' shape is discretised into 500m-length cubes, filled in accordance with density expectations for each interior. The resulting distributions for their geodesic observables were computed. Comparing these values to the homogeneous case and to each other, the scientific goals needed to constrain Phobos' origin were established.

The models' ranges for interior density and/or macro-porosity are indicative of a second-generation body. This hypothesis is strongly supported by the large Stickney impact which should have had major consequences on the interior, unless the original body were composed of highly porous material or contained a lot of water, as to absorb the impact energy and relax (LeMaistre et al. (2019)). Thence, porosity represents a

[1] Documentation: `https://tudat-space.readthedocs.io`

key clue in distinguishing the models, and may be expressed as follows for a monolithic interior:

$$p = \frac{\rho_{rock}}{\rho_{bulk}} = \frac{\rho_{rock}}{M/V} \tag{1}$$

MMX samples will constrain ρ_{rock}, so the porosity estimate will be affected by the volume uncertainty (currently 0.6%, Willner et al. (2014)) or the GM uncertainty (0.01%, Pätzold et al. (2014)). It is noted that detailed surface observations may lead to the development of complex mixtures of voids and boulders (amending eq. (1)) as recently done for Bennu (Scheeres et al. (2019a)) to provide evidence of a rubble pile asteroid.

2.2. Gravity Field

The gravitational potential of a celestial body is commonly expressed as a spherical harmonic expansion (Kaula (1966)):

$$V(r,\phi,\lambda) = \frac{GM}{r}\sum_{n=0}^{\infty}\sum_{m=0}^{n}\left[\left(\frac{R}{r}\right)^{l} \times \bar{P}_{nm}(\sin\phi)\left(\bar{C}_{nm}\cos m\lambda + \bar{S}_{nm}\sin m\lambda\right)\right] \tag{2}$$

where (r,λ,ϕ) indicate the observer's spherical coordinates in the Body-Fixed Frame (BFF), R the reference radius, $\bar{P}_{nm}$ the normalised Legendre functions of degree n and order m, and $\bar{C}_{nm}, \bar{S}_{nm}$ the associated spherical harmonic coefficients. For highly irregular bodies, alternative formulations for the potential are often adopted. Polyhedron discretisation (Werner and Scheeres (1996)) relies on the knowledge of interior density, which can be assumed homogeneous or assigned empirically. This was done by LeMaistre et al. (2019) who subsequently derived the equivalent harmonics via closed-form expressions (Werner (1997)). This formulation is useful for planning manoeuvres close to the surface, namely hovering, landing and ascent. The present work makes use of spherical harmonics to be consistent with literature, and because the considered orbits lie well outside the circumscribing sphere of Phobos, which guarantees convergence of the series.

Table 1 summarises the working models for Phobos' gravity field. That of LeMaistre et al. (2019) features the highest spatial resolution, and thus forms the basis for this study.

Degree-1 coefficients distinguish the Centre of Mass (CoM) and Centre of Figure (CoF), hence non-zero values are indicative of density heterogeneity. This phenomenon can be linked to the impact crater at Stickney: a heavily fractured interior would present a local decrease in density, whereas the porous compressed would show the opposite. A 1% accuracy on C_{11} and S_{11} would suffice to distinguish them (LeMaistre et al. (2019)), albeit this must be accompanied by an improvement in the ephemeris accuracy, currently dominating their uncertainty (Willner et al. (2014)). *Degree-2* harmonics reflect the radial mass distribution inside a body, conditioning its Moment of Inertia (MoI) as shown in eq. (3). Non-zero values for order-1 coefficients indicate a departure from the principal rotation axis. Although all heterogeneous families display this feature, none is uniquely distinguishable. On the other hand, a 5% fix on C_{20} and C_{22} would be sufficient to corroborate the degree-1 findings and possibly reveal an icy moon interior (LeMaistre et al. (2019)). However, a higher accuracy would be highly beneficial in characterising the density layers within Phobos (models analysed in Dmitrovskii et al. (2022)) and reinforcing the findings on libration, MoI and surface deformations. Comparing the *higher degree* coefficients to the respective homogeneous values reveals the local mass distributions. Some icy models exhibit lower density at the surface (due to evaporation) whereas the heavily fractured and porous compressed present an asymmetrical pattern. Overall, LeMaistre et al. (2019); Dmitrovskii et al. (2022) suggest that the rubble pile and icy moons would be hardest to differentiate due to their well-mixed interiors (5-10% coefficient overlap up to degree-10), whilst the others are uniquely distinguishable (10-40% overlap).

2.3. Moment of Inertia, Libration and Love Numbers

The MoI link the degree-2 harmonic coefficients to the body's rotational behaviour (Lambeck (1982)):

$$I_{ij} = I\delta_{ij} + MR^2\begin{bmatrix} \frac{1}{3}C_{20} - 2C_{22} & -2S_{22} & -C_{21} \\ -2S_{22} & \frac{1}{3}C_{20} + 2C_{22} & -S_{21} \\ -C_{21} & -S_{21} & -\frac{2}{3}C_{20} \end{bmatrix} \tag{3}$$

with δ_{ij} the Kronecker delta for i,j⊂x,y,z. This equation is under-determined (5 coefficients, 6 MoI) hence additional information on the rotational state must be provided. Phobos is locked in spin-orbit resonance on a near-equatorial orbit about Mars, but a small longitudinal libration θ persists (see Figure 4) driven by the gravitational torque, determined via I_{zz} and the eccentricity e. This is manifested in three types of observations:

- Secular and periodic variations in Phobos' orbit. Dynamical fitting can decompose the radial ($\hat{\boldsymbol{\rho}}$) and tangential ($\hat{\boldsymbol{t}}$) force responsible for these variations in terms of the gravity field and libration: (Jacobson and Lainey (2014)):

$$\mathbf{F}_0 = \frac{3}{2}GM\left(\frac{R^2}{r_{Ph,M}^4}\right)\left[(-C_{20} + 6C_{22}\cos 2\theta)\,\hat{\boldsymbol{\rho}} + 4C_{22}\sin 2\theta\hat{\mathbf{t}}\right] \tag{4}$$

- Oscillations in Phobos' synchronous rotation as inferred via kinematic analysis of its landmark positions by Willner et al. (2010); Burmeister et al. (2018)

- Perturbations in the spacecraft dynamics as the gravity field is tied to the BFF, which will act mainly via the C_{22} term, as C_{20} is longitudinally-symmetric

The insight obtained from constraining the MoI and the degree-2 coefficients are closely aligned. Interestingly, Matsumoto et al. (2021) derive that errors in θ and C_{20} and C_{22} equally influence the MoI uncertainties, meaning the obtained accuracy on θ should match that of C_{20} and C_{22}.

Finally, the ability of Phobos to deform in response to tidal forcing is expressed by the Love Number k_2. Its magnitude expresses the elasticity and viscosity profile, which may distinguish a rubble pile and monolithic interior (Dirkx et al. (2014))

Group	Method	Remarks
Jacobson and Lainey (2014)	Dynamical fitting of all astronomic observations, assume Willner et al. (2010) libration value	High correlations between C_{20} and C_{22}. Rejects heavily fractured and supports porous compressed interior at 3σ
Pätzold et al. (2014)	RS experiment from MEX flyby in 2010	Insufficient accuracy due to an unfavourable flyby geometry
Yang et al. (2019)	Includes 2013 MEX flyby and homogeneous a-priori regularisation	Better accuracy and lower correlation. Supports porous compressed interior and Guo et al. (2021) lighter core model
Willner et al. (2014) LeMaistre et al. (2019)	Based on degree-45 shape model with assumptions on interior density	Modelled, not observed. Complete up to degree-10. Basis for this study.

Table 1: Working models for Phobos' gravity field

and corroborate studies propagating Phobos' orbit backward in time (Bagheri et al. (2021)). Inferring the imaginary part of k_2 via the time-varying influence of degree-2 harmonics would be challenging, as for synchronously locked bodies the permanent tide overshadows the time-varying component (Dirkx (2015)). Its influence on the libration amplitude modulation is also extremely subtle (Yang et al. (2020) find 0.5mdeg). The most evident manifestations of k_2 are the tidally-induced surface deformations on Stickney crater's rim, spanning from 10cm to 1mm depending on the interior (Dmitrovskii et al. (2022)).

3. Dynamical Model and Orbit Design

This section describes the dynamical model of the Mars-Phobos system (summarised below) and the orbit strategy needed to cope with the high uncertainties associated with the former.

Mars	
Gravitational parameter	$42828.37 km^3/s^2$
Gravity field model	Genova et al. (2016)
Rotation model	Konopliv et al. (2016)
Phobos	
Gravitational parameter	$7.11 \cdot 10^{-4} km^3/s^2$
Gravity field model	LeMaistre et al. (2019)
Rotation model	Synchronous
Ephemeris	Lainey et al. (2021)
Radius	14 km
Semi-major axis	9378 km
Orbital period	7h 39m
Eccentricity	0.0151
Inclination wrt equator	1.072°
Start epoch	Jan 1^{st} 2030
Frame origin	Mars CoM
Frame Orientation	J2000 Ecliptic

Table 2: Dynamical Model adopted for Phobos and Mars. Note that for Phobos' orbital elements, the mean osculating values are reported.

3.1. Mission Setup

An overview of the setup driving the investigation is visible in Figure 1: only two methodological distinctions are highlighted here, the full setup is described in Section 5. Phobos' ephemeris (Lainey et al. (2021)) rests on the assumption of a *homogeneous interior*, which is deemed the most statistically representative of all interiors and is unaffected by high correlations on its degree-2 harmonics (see Table 2). Hence this is implemented for orbit design and parameter estimation. The *heterogeneous interiors* are subsequently adopted to assess the maintainability of the candidate orbits, which will constrain the length of the data arcs in the RS experiment (Section 5.4). Another distinction is that RS includes the determination of the spacecraft and Phobos state, which are mapped as external noise on the CG measurements to strengthen the fidelity of the experiment. On the other hand, CG only contributes towards the gravity field solution. By relating to the science goals outlined in the previous section, the extent to which both experiments can constrain Phobos' origin will finally be addressed.

3.2. Dynamical Model

The equations of motion are integrated using a fixed step, variable-order Adams-Bashforth-Moulton integrator (Montenbruck and Gill (2000)) and include these accelerations:

- Spherical harmonics of Mars up to degree-10
- Spherical harmonics of Phobos up to degree-10, including the mutual influence on its own orbit
- Point-mass attraction from the Sun and Deimos
- Cannonball-type solar radiation pressure (spacecraft only)

The accuracy gained from the inclusion of additional terms would be overshadowed by the uncertainty in Phobos' gravity field. Due to the higher-order perturbations, the spacecraft dynamics around Phobos will depend on the start epoch, though only slightly. For practical purposes a date in the future is chosen which guarantees a favourable observation geometry with Earth's ground stations. Since the latest estimate for Phobos' libration ($\theta = 1.09^\circ$, Lainey et al. (2021)) obtained via dynamical fitting does not agree with a homogeneous interior, its rotation model was assumed to be fully locked. Consequently, the time-varying influence of the longitudinally-asymmetric C_{22} is omitted, yet the retrograde orbit geometry seeks to minimise the destabilising influence of this term (see Figure 2). Hence, this assumption does not invalidate the orbit selection. This work

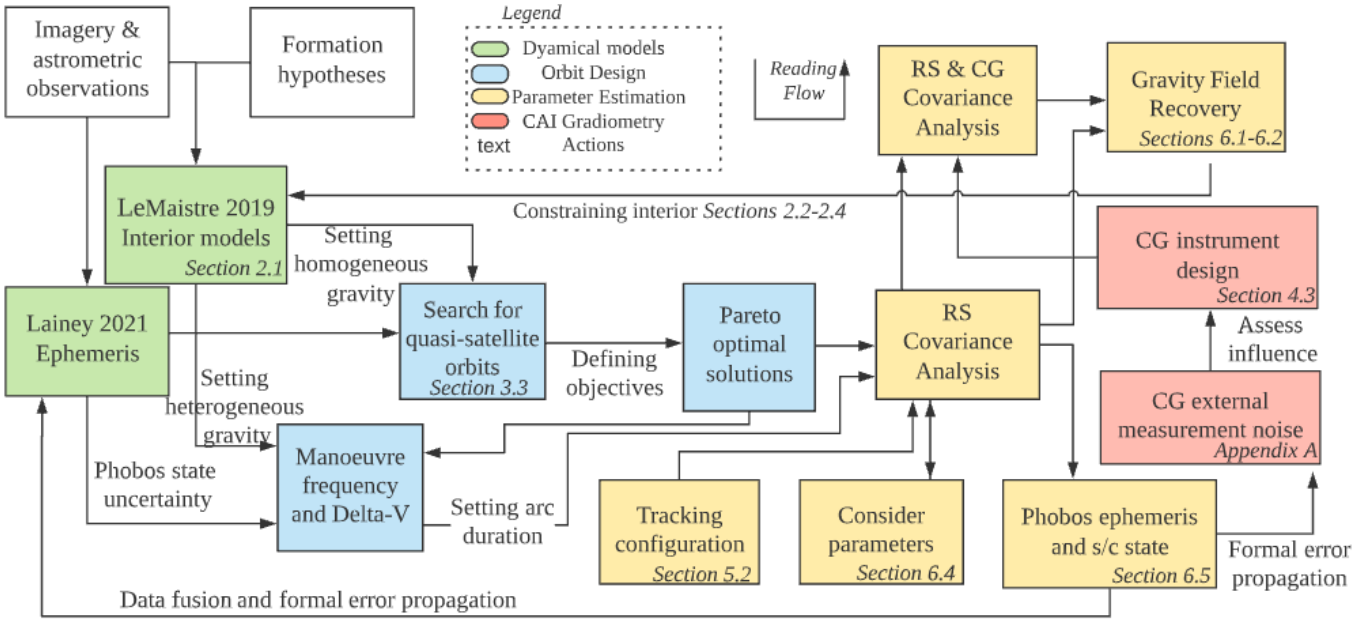

Figure 1: Flowchart summarising the methodology adopted in this work and the relevant sections in the paper.

uses the latest spice ephemeris (Lainey et al. (2021)) which reflects the knowledge of the Martian system and is computationally efficient for the orbit design phase. Yet it is critical to note that during parameter estimation (Section 5.4) Phobos is numerically propagated, as this enables a robust estimation of its state and propagation of its associated uncertainty. As we do not model libration a secular drift appears between the spice-retrieved and propagated Phobos (last term in eq. (4)) inducing in a 300m difference in state w.r.t. Mars after one week.

3.3. Quasi-Satellite Orbits

Phobos lies closer to its primary's surface than any other planetary moon, which entails strong tidal perturbations from Mars as well as its own non-sphericity (Scheeres et al. (2019b)). This prohibits the use of Keplerian orbits, and instead one must resort to Quasi-Satellite Orbits (QSO) whereby Mars is the dominant attractor, and Phobos is orbited in the sense of relative motion. In light of the MMX mission, Chen et al. (2020); Baresi et al. (2020); Pushparaj et al. (2021) have advanced QSOs and maintenance strategies. To gain a physical understanding of the dynamics for planning efficient manoeuvres, these typically adopt the elliptic Hill formulation for a time-invariant system, or omit higher-order terms of Phobos' gravity field. This is incompatible with the present experiment, which is less concerned with constructing a high-fidelity orbit strategy for Phobos, focussing instead on the performance of CG in recovering the full harmonic spectrum for small bodies. To this end, a larger variety of orbital geometries is considered here.

A grid search with a differential corrector step (details in Chen et al. (2020)) set out to find a set of initial conditions leading to orbits which stay bound to Phobos for one week. This timespan can guarantee an acceptable geodetic solution accuracy, without incurring excessive costs in terms of orbit maintenance and computational runtime. The search yielded a total of 7000 suitable initial conditions; to make this number compatible with parameter estimation without sacrificing the diversity in orbital geometries, these solutions were classified in accordance with three objectives:

1. Proximity, expressed by the mean distance between Phobos' CoM and the spacecraft ($\overline{r}$). Close orbits are expected to perform well in the estimation as the gravitational influence on the spacecraft is more pronounced.
2. Coverage, computed as the mean euclidean norm of all ground track points mapped in latitude and longitude space ($\overline{euc}$). This is desired to better observe the moon's surface and decorrelate the influence of individual harmonics.
3. Stability, expressed by the largest modulus of the eigenvalues of the state transition matrix $\mathbf{\Phi}$ after one period. This matrix expresses the linear mapping of the spacecraft state after one period, and its eigenvalues indicate the stability to initial perturbations. This quantity has been normalised by the number of revolutions to ensure a fair comparison across the orbits, i.e. $\lambda_n = max(\sqrt[revs]{|\lambda_i(\mathbf{\Phi})|})$

A non-dominated objective sorting algorithm yielded a subset of 102 optimal solutions, also known as a Pareto Front (PF). This is depicted in Figure 2 with three representative orbits. "low" orbits generally have an unfavourable coverage and a precarious stability, "high" orbits display the opposite, and "medium" orbits somewhere in between. Finally, a sensitivity analysis was performed to investigate the robustness of the PF solutions with regards to injection and dynamical model errors. The associated maintenance budgets were validated against those obtained from the above literature.

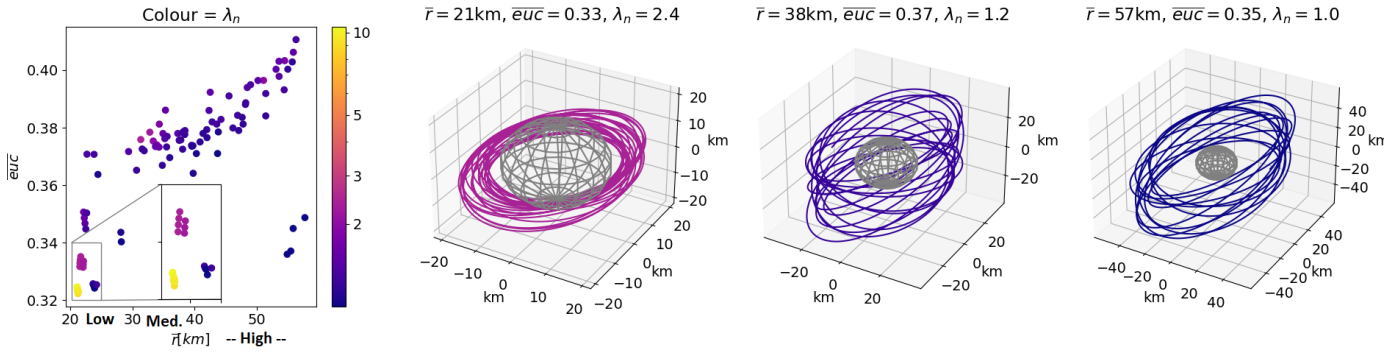

Figure 2: Pareto Front for the non-dominated objective space of proximity, coverage, and stability. Three sample trajectories (low, medium and high) are plotted in the BFF. The motion is retrograde (clockwise) as to curtail the destabilising effect of the C_{22} term which is "averaged out" in space due to the large relative angular motion between the spacecraft and Phobos (Scheeres (2012))

4. Cold Atom Interferometry

This section summarises the working principle of CAI gradiometry, focussing on the advantages and limitations entailed by space application. Operational modes are contextualised in the framework of the mission to produce an ensemble of CAI configurations. Only the Mach–Zehnder type interferometer with Raman diffraction is treated here, schematised in Figure 3.

4.1. Measurement Sequence

Atom Cloud Preparation. A magneto-optical trap (MOT) captures the atomic cloud and cools it to extreme temperatures T_k that are needed to manifest the wave duality of atoms. For utmost sensitivity temperatures below $0.4nK$ are required, possible via Bose Einstein Condensates (Carraz et al. (2014)). Upon their release, the velocity spread of the atomic cloud σ_v is:

$$\sigma_v = \sqrt{\frac{T_k \cdot k_B}{m_{at}}} \tag{5}$$

with k_B the Boltzmann constant and m_{at} the mass of the atomic source. A common choice is ^{87}Rb due to its stable hyperfine structure which can be treated as two-level system (Barrett et al. (2013)). The product $\sigma_v.T$ will constrain the diameter of the laser pulse, typically $< 1cm$.

Pulse Sequence. The atomic source is injected into the interference chamber with velocity $\mathbf{v_t} = 2.5cm/s = 4\mathbf{v_{rec}}$, i.e. four times the photon recoil velocity. The underlying principle of CAI is the momentum conservation between the atoms and the light field: the absorption (emission) of a photon with Raman momentum vector $\hbar\mathbf{k}$ will result in a momentum recoil of $\hbar\mathbf{k}$ (-$\hbar\mathbf{k}$), with $|k| = 4\pi/780nm$ (Barrett et al. (2013)). Due to the Raman interaction, the atomic clouds receive a $2\mathbf{v_{rec}}$ kick in the opposite direction. The first pulse acts as a beamsplitter, causing an equal superposition of quantum states propagating freely along two paths. A second pulse applied at time T fully inverts the states of the two populations, delivering photon recoils to both clouds to rejoin them at time 2T. The last Raman pulse closes the interferometer sequence, during which a phase difference ϕ_{acc} has been accumulated as a result of the different gravitational acceleration g acting on the paths.

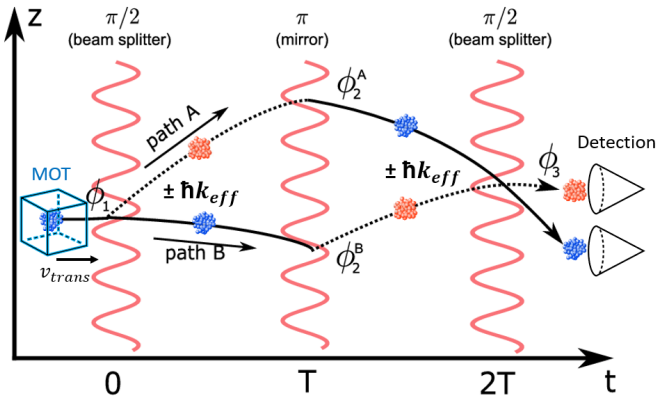

Figure 3: Three-pulse sequence via Raman transitions, adapted from Hauth et al. (2014). The lines indicate the classical trajectories of the atoms under the influence of gravity, representing two-level internal states

Detecting Gravity and Rotation. At the output ports, interference fringes are detected by monitoring the normalised population in the two hyperfine states. The associated phase difference readouts are $\phi_{acc} = -kgT^2$. The T^2 dependency highlights the readout accuracy gained by operating CAI in microgravity. Moreover, CAI gravity measurements are absolute, and require no calibration as opposed to the classical electrostatic gradiometers on GOCE (Frommknecht et al. (2011)). However, the rotation Ω experienced by the CAI setup, coupled with the non-zero $\mathbf{v_t}$, give rise to an additional phase shift due to the Sagnac effect (Barrett et al. (2013)). This and the thermal expansion of the atomic cloud (eq. (5)) result in trajectories that do not close perfectly at the third beam splitting pulse, which negatively effects the quality of the readout measurements expressed by the gradiometer contrast. Section 4.2 outlines the strategies which can mitigate this effect.

Gradiometry. An additional pulse may be added, separating the initial cloud by a baseline d, such that two measurements are obtained in gradiometric fashion. This suppresses common vibration noise sources such as light shifts and magnetic field gradients (Carraz et al. (2014)), enhancing the gradiometric sensitivity by a factor $\sqrt{2}$, defined in the frequency spectrum as:

$$\sigma_\gamma = \sigma_{\Delta\phi} \frac{\sqrt{2}}{kT^2 d} \sqrt{t_m} \tag{6}$$

where the total measurement time is $t_m = 2T + 1s$ required for cooling. It is commonly assumed that the sensitivity to phase readouts is limited by the detection noise at the quantum projection limit, $\sigma_{\Delta\phi} \propto 1/\sqrt{N_{atoms}}$, although it is worth mentioning that ongoing efforts (Gross (2012)) are striving for "squeezed" atomic states that could theoretically achieve $\sigma_{\Delta\phi} \propto 1/N_{atoms}$. Note that the noise spectrum is flat for frequencies $f < 1/t_m$, then it degrades by a factor $(2T.f)^{1/2}$ (Carraz et al. (2014)).

4.2. Interferometer Phase Shift

The impact of physical perturbations on the phase readouts are investigated to address the need for compensation mechanisms as suggested by Trimeche et al. (2019). The Gradiometer Reference Frame (GRF), fixed to the satellite as illustrated in Figure 4, is orbiting at a nearly constant frequency Ω_{orb} with respect to the dominant attractor, in this case Mars[2]. For the sake of simplicity, this work assumes $\Omega_y = \Omega_{orb}$ and $\Omega_{xy} = 0$. In reality, this is not the case due to strong third-body perturbations and, to a lesser extent, non-conservative forces. Nonetheless, Ω_y dominates the conversion of the gradiometric measurements from the GRF to the BFF (see Section 5.5), hence this approach correctly deals with the influence of rotations at the leading orders. We discuss in the following the cases with and without compensation for rotation and gradient dephasing.

Without Compensation. Due to the Sagnac effect, the uncertainty in δv_t imprints a rotation-induced dephasing $\delta\phi$ on the interferometer flight and nadir axes. The loss of contrast is negligible if the separation is much smaller than the coherence length of the atomic wavepackets (Trimeche et al. (2019)). Using the De Broglie wavelength, this requirement is expressed in terms of T_k as reported in Table 3. A secondary effect concerns the dephasing induced by the gravity gradient, for which a similar temperature limit and contrast loss can be derived (Roura et al. (2014)). To ensure a reliable detection, the combined effect of dephasings must be kept below the quantum projection limit.

With Compensation. An effective means of ensuring a fixed orientation in the frame of the atoms consists in actively tilting the first and the last retro-reflecting mirrors by an angle $\pm\theta_m = \pm\Omega_y T$ (see Figure 4). This method calls for external star trackers and gyrometers for measuring angular velocity. Any error in the latter will translate to a misalignment $\delta\theta = \delta\Omega_m T$, with the associated dephasing reported in Table 3. The downside of retro-reflecting mirrors are the stringent dynamic requirements for operation, limiting CAI measurements to a single axis. Gravity gradient compensation mechanisms, demonstrated by D'Amico et al. (2017), rely on an adequate tuning δk of the Raman wavevector at the second pulse. This offsets their influence across the gradiometric phase, nevertheless, small fluctuations persist (Trimeche et al. (2019)).

[2]Although Phobos's gravity field will prevail for the low orbits, coincidentally, $\Omega_{orb,Mars} \approx \Omega_{orb,Phobos}$ hence the same rotation is experienced.

	No Compensation	Compensated
	Any $\Omega_{orb,y,m}$ $\delta k = 0$	$\Omega_m = \Omega_y + \delta\Omega_m$ $\delta_k = kV_{zz}T^2/2$
Sagnac noise [rad] negligible for $T_k < \frac{m}{16k_B k^2 \Omega_y^2 T^4}$	$4k\delta v_t(-\Omega_m$ $+\Omega_y)T^2$	$4k\delta v_t \delta\Omega_m T^2$
Gradient noise [rad] negligible for $T_k < \frac{m}{4k_b k^2 V_{zz}^2 T^6}$	$2kd(V_{zz}$ $-\Omega_m^2 + \Omega_y^2)T^2$	$4kd\delta\Omega_m\Omega_y T^2$

Table 3: Leading phase errors for differential CAI measurements

Concerning the operatinoal modes, *inertial pointing* ($\Omega_{xyz} \approx 0$) has been investigated by Douch et al. (2018) for CG on Earth. To maintain the readout noise below 1mrad, spurious rotation rates must be kept below $\Omega < 1.5\mu rad/s$ (Carraz et al. (2014)) which is extremely challenging from an engineering standpoint, especially considering the strong third body perturbations by Phobos. This concept is therefore abandoned in favour of *nadir pointing*, for which $\Omega_y = \Omega_{orb}$. Despite it being limited to a single axis, Douch et al. (2018) have demonstrated that the benefits of 3-axis measurements are concentrated around high-degree harmonics, which is beyond the scope of exploratory missions. It is important to emphasise that nadir pointing does not constrain the axis orientation, but merely its uniqueness. Since the nature of the problem does not suggest a prevailing axis for which the gravity signal will be stronger[3], numerical simulations will cover all three cases. The CAI orientation which leads to the best gravity field solution will be selected. The mitigation strategy outlined above is applicable to both nadir and flight directions, which are influenced by Ω_y. The cross-track axis remains unaffected, meaning a simplified setup composed of fixed and parallel mirrors can be used (Trimeche et al. (2019)). Nonetheless, the nature of the problem suggests that this axis will underperform as it will mostly point away from to Phobos, as demonstrated by the coplanar orbits in Figure 4.

The measurement time t_m is highlighted as a key trade-off parameter. Extending it is beneficial for the overall sensitivity (eq. (6)) but it exacerbates the dephasing induced by rotation. Given that each measurement is averaged along the orbital path, longer measurements may not be able to resolve the finer harmonics. Finally, a large t_m comes at the expense of a more voluminous instrument, given that the baseline must accommodate two counter-propagating clouds, $d/2 \geqslant 2v_{rec}$, and the length should be $> 2Tv_t$ as illustrated in Figure 3.

4.3. CAI Concepts

Based on Table 3, eq. (5) and eq. (6) two CAI configurations are generated as part of this study, with characteristics outlined in table 4. CAI 1 reaches ultracold atomic temperatures via

[3]This may sound counter-intuitive as one could expect that the gradiometer must be aligned with the celestial body's CoM to sense a signal. This is not necessarily the case. In fact, the cross-track axis for GOCE received, on average, half the signal strength compared to the nadir axis (personal communication).

Delta Kick collimation techniques (Kovachy et al. (2015)) curtailing the need for rotation compensation. This yields a relatively simple setup with a high measurement rate, albeit with a limited sensitivity. CAI 2 is based on rotation compensation that imposes an attitude and tilt-mirror control of $1\mu rad/s$ and $5\mu rad$ along the y axis, respectively. This requirement is within the capabilities of fiber optic gyrometers of the ASTRIX 200 class and commercially-available star trackers. The incurred complexity offers a sensitivity competitive with that of low-noise axes of GOCE ($10mE/\sqrt{Hz}$, Rummel et al. (2010)).

	CAI 1	**CAI 2**
N_{atoms}	10^4	$5 \cdot 10^5$
T_k	1pK	1nK
T	2.6s	5s
σ_γ	$0.462E\sqrt{Hz}$	$37.5mE\sqrt{Hz}$
Comp.	None	$\delta\Omega_m = 1\mu rad$
Size chamber	$70x13cm^2$	$50x25cm^2$
Laser $\varnothing$	1.55mm	$0.25\mu m$
Weight	163.7kg	170.2kg
Power	480W	560W

Table 4: CAI gradiometry concepts

Weight and power estimates are adopted from the feasibility study ESA (2018) which features comparable instrument dimensions and sensitivity[4]. These estimates are deemed impractical for interplanetary missions, nonetheless, ongoing technological developments are expected to significantly reduce these values. In fact, Devani et al. (2020) aim to produce 10^7 laser-cooled atoms for on a CubeSat platform weighing just over 4 kg and consuming 40 W, albeit for higher atomic temperatures.

Although CAI gradiometers have yet to reach full maturity, numerous existing applications (Bongs et al. (2019)) are enhancing the TRL of its constituents. Yu et al. (2006) were capable of $\sigma_\gamma = 40E/\sqrt{Hz}$ with a TRL of 5 in 2015, whereas Bienstock (2020) projected reaching $\sigma_\gamma < 1E/\sqrt{Hz}$ on ground (which translates to $\approx 10^{-5}E/\sqrt{Hz}$ is microgravity) and a TRL of 5 by 2021. With NASA's Cold Atom Lab successfully producing BECs on the ISS (Elliott et al. (2018)), there are high hopes that the ambitious CAI endeavours will prove successful.

5. Methodology

This section outlines the setup of the numerical simulations for gravity field recovery. The underlying mechanism for parameter estimation is introduced, followed by a description of the tracking settings and a summary of the sought parameters. In accordance with the sequence in Figure 1, the RS experiment is described first, as it can be performed independently, whereas CG requires an estimate for the spacecraft and Phobos states.

[4]Personal communication yielded scaling factors which reduce the mass and power estimates compared to Earth concepts, due to the absence of magnetic shielding and a less demanding cooling mechanism for CAI 2.

5.1. Covariance Analysis

The sought gravity field harmonics influence Phobos' dynamics, meaning that a batch estimator would entail the re-integration of the equations of motion and variational equations at each iteration, which is not ideal considering the vast number of orbits. Moreover, given that RS tracking is an ineluctable part of all missions, the *relative* contribution of CG plays a stronger role than the *absolute* accuracy of the gravity field solution. A covariance analysis is particularly suited here as a quick and effective means of comparing the formal errors obtained via different types of measurements, but with the same dynamical model. It also enables flexibility in constraining the true-to-formal error ratio for both RS (Section 6.4) and CG (Appendix A). The formal errors σ_i are obtained from the diagonal of the covariance matrix $\boldsymbol{P}$ (Montenbruck and Gill (2000)):

$$\begin{aligned} \boldsymbol{P} &= \left(\boldsymbol{P}_{apr.}^{-1} + \boldsymbol{H}^{\mathrm{T}}\boldsymbol{W}\boldsymbol{H}\right)^{-1} \\ \sigma_i &= \sqrt{\boldsymbol{P}_{ii}} \end{aligned} \tag{7}$$

with $\boldsymbol{H}$ the Jacobian matrix and $\boldsymbol{W}$ the diagonal weight matrix for uncorrelated measurements. The latter holds true for most tracking observables and CAI measurements (which are absolute in nature). The orbital geometry cannot guarantee a full coverage which may lead to ill-posedness in the estimation, especially for low-power harmonics (see Figure 8). This is avoided by introducing a priori knowledge via $\boldsymbol{P}_{apr.}$. A potent strategy to account for the effect of unmodelled, systematic errors is to setup a *consider* covariance analysis. A number of consider parameters are appended to the estimation process without actually being estimated, but whose uncertainty is mapped onto the formal errors (Montenbruck and Gill (2000)):

$$\boldsymbol{P_C} = \boldsymbol{P} + \left(\boldsymbol{P}\boldsymbol{H}^T\boldsymbol{W}\right)\left(\boldsymbol{H_c}\boldsymbol{C}\boldsymbol{H_c}^T\right)\left(\boldsymbol{P}\boldsymbol{H}^T\boldsymbol{W}\right)^T \tag{8}$$

here, $\boldsymbol{H_c}$ is the Jacobian matrix for the so-called consider parameters (listed in Table 5) whose covariance is the diagonal of $\boldsymbol{C}$. In contrast to eq. (7), where σ_i reduce with $1/\sqrt{N_{obs}}$, the systematic terms in eq. (8) are essentially constant for a given data arc and tracking configuration, hence they limit the attainable solution accuracy (Montenbruck and Gill (2000)).

5.2. Tracking Data

Tracking is performed via a combination of radiometric measurements originating from ground stations in Norcia (Australia), Robledo (Spain) and Goldstone (USA), as well as angular landmark positions obtained via optical imagery.

Doppler observables are modelled with a random noise of $30\mu m/s$ at $60s$ integration time, which is typical for a two-way X-band system at favourable Sun–Earth–Mars angles (Konopliv et al. (2014); Genova et al. (2016)). The integration time can be tuned to balance the measurement volume and noise, which reduces with $\approx 1/\sqrt{t_{int}}$. Range observables, being an absolute measure of distance, are sensitive to random errors as well as biases (Thornton and Border (2003)), hence closely-spaced measurements can present correlations. Based on X-band performances (Iess et al. (2014); Scheeres et al. (2019a)) a $2m$ random noise and bias is set, and a cadence of 300s. The

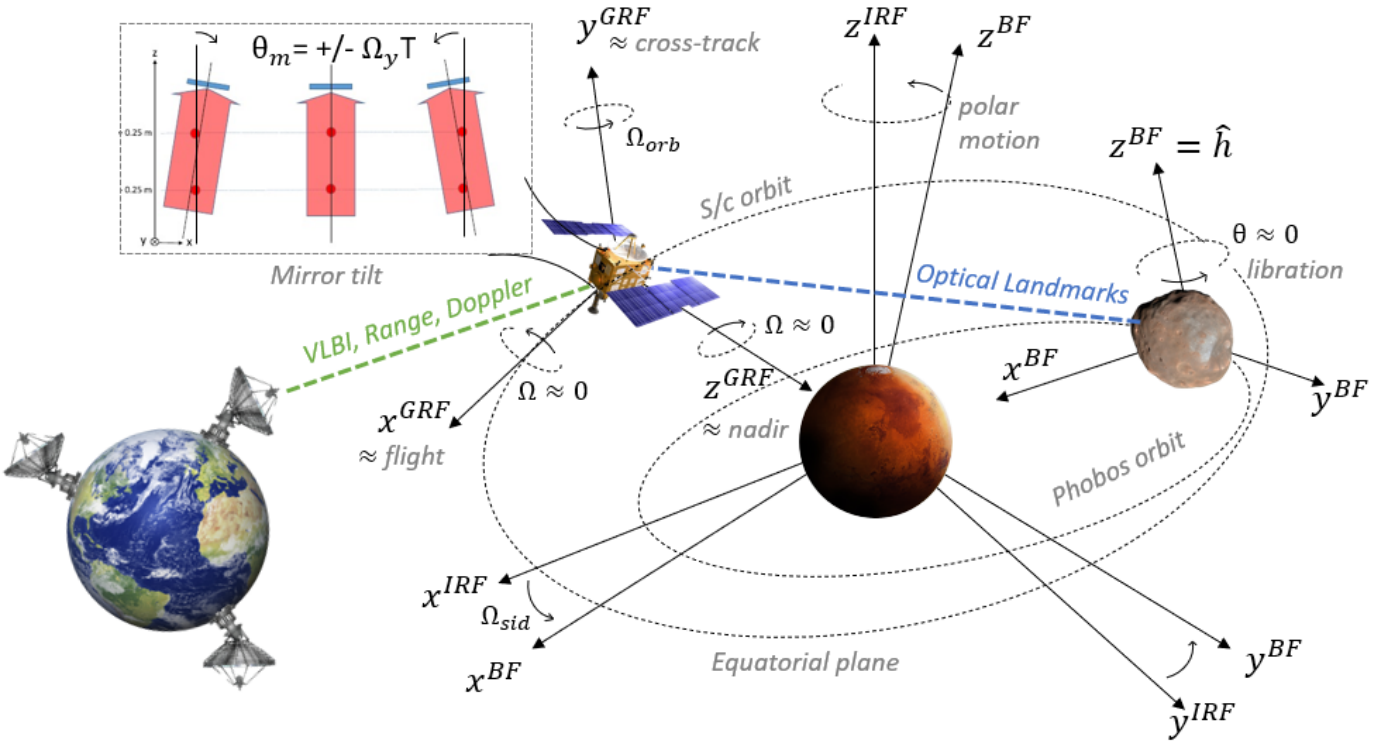

Figure 4: Illustrating the reference frames, rotations and tracking observables. Note that the bodies and their orbits are not to scale.

spacecraft's angular position is determined via Very Long Baseline Interferometry (VLBI), whose bias and noise levels are set to $1.5nrad$ with a cadence of $300s$ (Duev et al. (2016)).

Optical landmark tracking is very effective for targets that present distinctive surface features, such as craters or boulders. Measurements display a strong sensitivity in the direction perpendicular to the line-of-sight, strongly supporting the retrieval of shape, rotation and ephemeris models as done for Eros (Miller et al. (2002)) Vesta (Konopliv et al. (2014)) and Bennu (Goossens et al. (2021)). This data is influenced by uncertainties in the spacecraft position and camera pointing, which are hard to decouple, since -unlike Doppler- angular observables are insensitive to the radial position of the camera. Yet, merging optical and radiometric data is difficult as the former are dependent on the a priori knowledge of the shape and ephemeris of the body (Park et al. (2019)). To this end, the effect of different pointing errors and biases of (0.1-0.5° as for MEX, Burmeister et al. (2018)) is investigated in Section 6.3. 25 landmarks are scattered in latitude ranges $\pm 60°$, in accordance with Phobos' shape models (Willner et al. (2010)). Similar to Vesta, images are captured every 5-10 min which is a slightly optimistic assumption to compensate for the short mission duration. Since the spacecraft will tend to align with Mars, gimbals or pointing calibrations will be needed for imagery, yet these are deemed feasible as the relative velocity w.r.t. Phobos is of a few m/s.

Parameter Name	**Symbol**	**a priori st. dev**
Phobos initial state	r_{Ph}, v_{Ph}	$100m, 0.3mm/s$
Phobos landmarks	r_{lnd}	12 m from shape models Witasse et al. (2014)
Phobos gravitational parameter	GM	$0.7km^3/s^2$ from flyby Pätzold et al. (2014)
Phobos spherical harmonics	C_{nm}, S_{nm}	from heter. models LeMaistre et al. (2019)
S/c initial states	r_{Sc}, v_{Sc}	$50m, 3cm/s$ from MMX Baresi et al. (2020)
S/c radiation pressure coeff.	C_r	0.1 from Vesta & Eros missions
S/c momentum wheel desaturation	ΔV_{des}	0 due to symmetric thrusting at mid-arc
Optical biases	β_b	0.1-0.5°
Range biases	ρ_b	2m
VLBI biases	α_b	1.5nrad
Ground station positions*	r_{GS}	*1-5-10mm
S/c empirical accelerations *	a_{emp}	10nm/s *1-0.01-0.05nm/s^2

Table 5: Estimated science (top) and mission (bottom) parameters. Consider parameters are marked with an asterisk. Note that the empirical acceleration is also estimated as a regular parameter.

5.3. Estimated Parameters

The full list of estimated (and consider) parameters with their a-priori regularisation (covariance) is reported in Table 5.

Setting a priori constraints for the gravity field is complicated by the lack of empirical evidence for the gravity spectra of small bodies. In fact, only Eros (Miller et al. (2002)), Vesta (Kono-

pliv et al. (2014)) Ceres (Konopliv et al. (2018)) and Bennu (Scheeres et al. (2019a)) have both gravity and shape models accurately described. The Kaula rule for gravity is typically used for this intent, but Ermakov and Bills (2018) show that it becomes invalid for bodies with $R < 40km$, due mainly to the variability at low degrees, which are dominated by unordered processes such as impact cratering. They suggest the most valid scaling for the gravity spectrum relies on shape models and interior density assumptions, as long as the former are of higher order and that a conservatively high value for the radius is chosen. Therefore, the maximum standard deviation of the spherical harmonics from the heterogeneous ensembles were set as a-priori values for the gravity spectrum. Most values originate from the porous compressed models, which exhibit the largest spread. For the CG experiment (Section 6.2), the full 10x10 spectrum could be inferred, whereas for the RS-only case (Section 6.1) this has lead to an ill-posed estimation. Hence, the spectrum for RS was truncated to degree-6, with the covariance forcing higher terms to zero. As reported by the circled markers in Figure 6, this is where the formal errors cross the a-priori values for a majority of orbits, whilst still ensuring a tolerable condition number for the gravity field columns in the inversion.

Two sets of consider parameters have been included. Firstly the Earth-based ground station positions, which are affected by uncertainties at the mm level (Kosek et al. (2020)) even after correction for tidal and antenna deformation effects. Secondly the empirical accelerations, which absorb any unmodelled forces that cannot suitably be described due to limited knowledge of the spacecraft's time-varying orientation, material properties, and surface temperatures (Montenbruck and Gill (2000)). Here, one is concerned with risk that empirical accelerations will mask the gravity signal from high degrees. These are modelled as 3-axis constant and sinusoidal components with amplitudes as with missions to Eros and Mars (for axes that are unaffected by drag, Genova et al. (2016)). Their lowest covariance values matches that of OSIRIS-REx at Bennu, which is deemed optimistic, yet feasible in case that a detailed panelled thermal radiation model is available.

5.4. Hybrid-Arc Parameter Estimation

Parameter estimation is performed concurrently in a single inversion, entailing a hybrid-arc approach whereby the dynamics of the spacecraft and Phobos are integrated in a multi-arc and single-arc fashion, respectively (Fayolle et al. (2021), to be submitted). This offers the distinct advantage of incorporating the dynamical couplings thus reducing the risk of misattributing a signal in the spacecraft's dynamics to Phobos' dynamics (Dirkx et al. (2018)) which is significant as both are dominated by Mars' gravity. For the spacecraft, long arcs may lead to convergence issues due to the build up of unmodelled forces, whereas short arcs may deteriorate the solution quality as not all effects are captured correctly. Arcs may also be sectioned at the manoeuvre times (Genova et al. (2016); Konopliv et al. (2016)) as to avoid having to estimate the associated velocity increments, a choice which is further validated in Section 6.1.

5.5. Gradiometry

The CAI sequence outlined in Section 4.1 delivers point-wise gravity gradient measurements Vij along the xyz axes in the GRF. These are related to the gravitational potential V (eq. (2)) via the observational equation for gradiometry:

$$\begin{bmatrix} V_{xx} & V_{xy} & V_{xz} \\ V_{xy} & V_{yy} & V_{yz} \\ V_{xz} & V_{yz} & V_{zz} \end{bmatrix}^{GRF} = \boldsymbol{R} \frac{\partial^2 V^{LNOF}}{\partial x_i \partial x_j} \boldsymbol{R}^T \tag{9}$$

although V is tied to the BFF, its second-order partial derivatives (elaborated in Freeden et al. (2015)) are easily computed in the Local North-Oriented Frame (LNOF). Hence the gradients must undergo a sequence of rotations $\boldsymbol{R} : GRF \rightarrow IRF \rightarrow BFF \rightarrow LNOF$ (Siemes (2012)). Since we do not have access to real measurements, the simulator takes a gravitational model and the noise-free time series of the satellite orbit and attitude to set up $\boldsymbol{H} = \partial V_{ij}/\partial C_{nm}, S_{nm}$ and $\boldsymbol{W_{ii}} = 1/\sigma_\gamma^2$.

Four external noise sources affect gradiometry. Attitude control errors limit the ability to overcome attitude disturbances. Attitude knowledge errors hinder the process of geolocating the observables to Phobos' CoM. For their assessment one must consider rotational dynamics and attitude quaternions for calibration (Siemes et al. (2019)) which is beyond the scope here. Instead, a covariance analysis (details in Appendix A) was implemented to verify that positioning and dynamical model errors do not compromise the fidelity of the CG experiment.

6. Results & Discussion

This section presents the outcome of the numerical simulations for the RS-only and combined experiments. The full gravity spectrum obtained via the "best" orbit for each experiment is shown in Figure 5 and 10, respectively. A detailed analysis will follow, but the completion of the science goals can already be inferred from these figures. Finally, for the RS case, the relative contribution of tracking data types and the influence of consider parameters is evaluated, followed by a qualitative discussion on the improvement of Phobos' ephemeris and libration.

6.1. Gravity Field Recovery, Radio Science only

Figure 6 presents the simulation results of the RS gravity field experiment for all orbits in the PF. The figure of metric is selected as the (root-mean-square) formal error of the spherical coefficients, grouped per degree. This is reported as an absolute value as opposed to being normalised, the reason being as follows. The estimation is performed assuming a homogeneous interior, whereas the actual Phobos will present more heterogeneity. Hence, the real coefficients will display a stronger signature meaning the resulting solution accuracy will likely be higher. Normalising the formal errors of the spherical coefficients by their homogeneous values would thus be slightly misleading. Nonetheless, this is done in Figure 5 and 10 and reported as (x%) in the following discussion, as it is the only way of relating to the science goals outlined in Section 2. It should also be noted that VLBI and range data have been omitted as they have a negligible contribution (details in Section 6.3) and

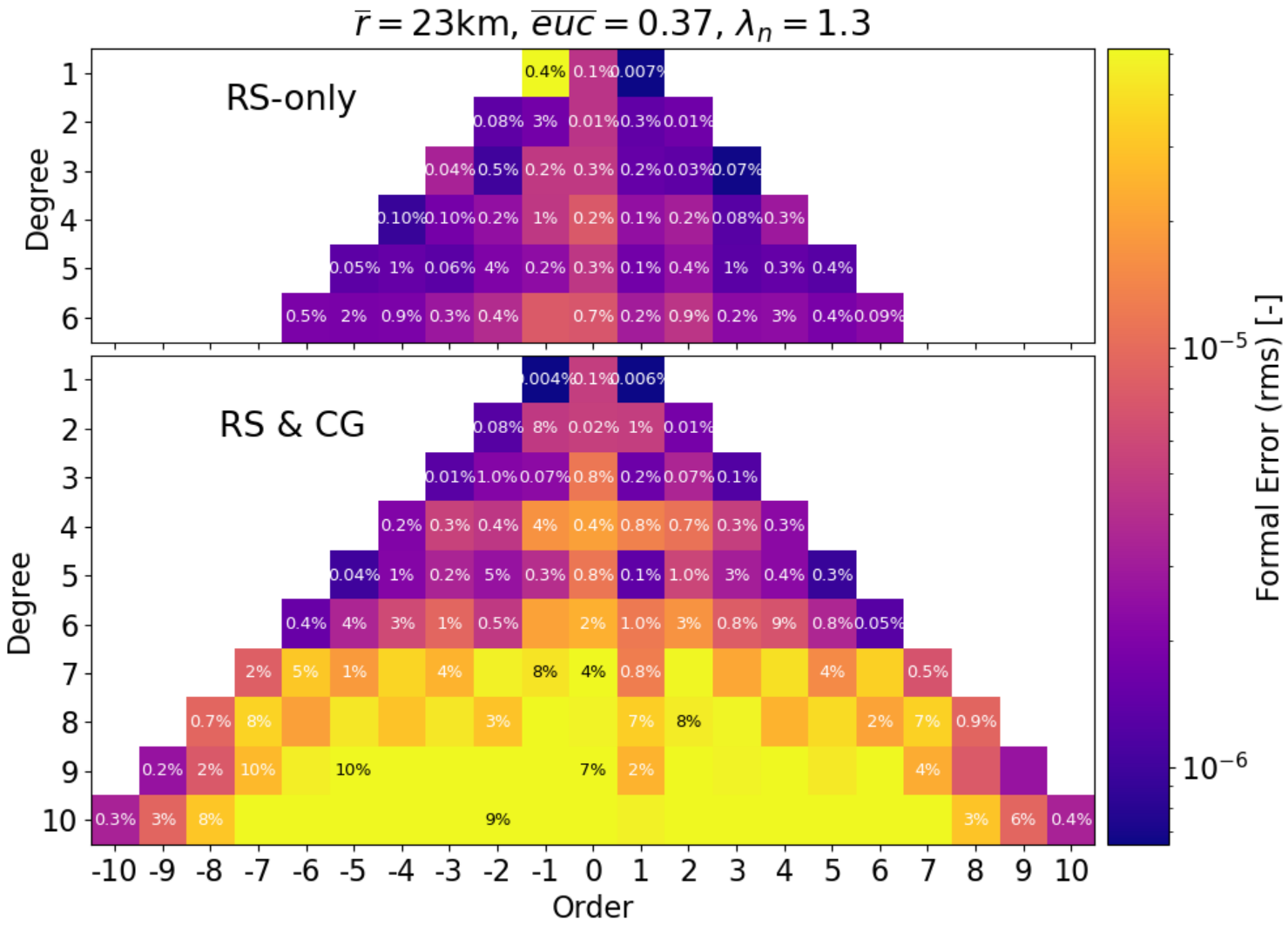

Figure 5: Formal errors for the gravity spectrum obtained via the best orbit in the RS experiment, marked by a star in Figure 6. This leads to the highest accuracy for degrees 1 to 3, and entails low maintenance costs. Errors are reported as absolute (colour) and homogeneous-normalised (percentage) values. Missing percentages indicate a formal error greater than 100%, some of which correspond to harmonics with very small magnitudes in the homogeneous model (see Figure 8). Note that the true errors for the top pyramid could increase by a factor 4-6 due to the influence of systematic uncertainties (see Figure 12) and a reduction in tracking capacity.

that the true error could be a factor 2-3 higher due to the influence of systematic uncertainties (described in Section 6.4).

Two general remarks can be drawn from Figure 6. First, RS seems extremely competitive as it can achieve an accuracy of 10^{-5} (0.01% w.r.t. homogeneous) for degrees 1 to 6, provided that the orbit altitude is kept low. Second, it is seen that the region of highest accuracy gradually moves to smaller values of $\bar{r}$ for higher degrees. Evidently, the finer wavelengths can only be detected closer to Phobos. Hence the selection this this metric to create the PF is deemed valid. The coverage metric is also effective: orbits with low $\overline{euc}$ underperform even at low altitudes, and tend compensate the loss in accuracy by relying additionally on a-priori values, as reflected by the circled markers (clearly visible for degree-3). The condition number for the overall inversion is between 10^9 and 10^{12} across the entire PF, which is reasonable for interplanetary missions. As depicted in Figure 7 the correlations driving up this number mainly concern the state of Phobos and the spacecraft (only values for a single arc are shown). The condition number for the gravity field parameters is between 10^3 and 10^5, which is quite favourable. Let us now focus more attentively on the individual harmonics.

Degree-1 coefficients are resolved to 10^{-4} (0.01%) translating to an uncertainty in the CoM position of $14m$. At low orbits an accuracy of 10^{-5} is made possible by the fact that the optical bias is better resolved with Doppler data (details in Section 6.3). Figure 7 demonstrates that only S_{11}, which expresses

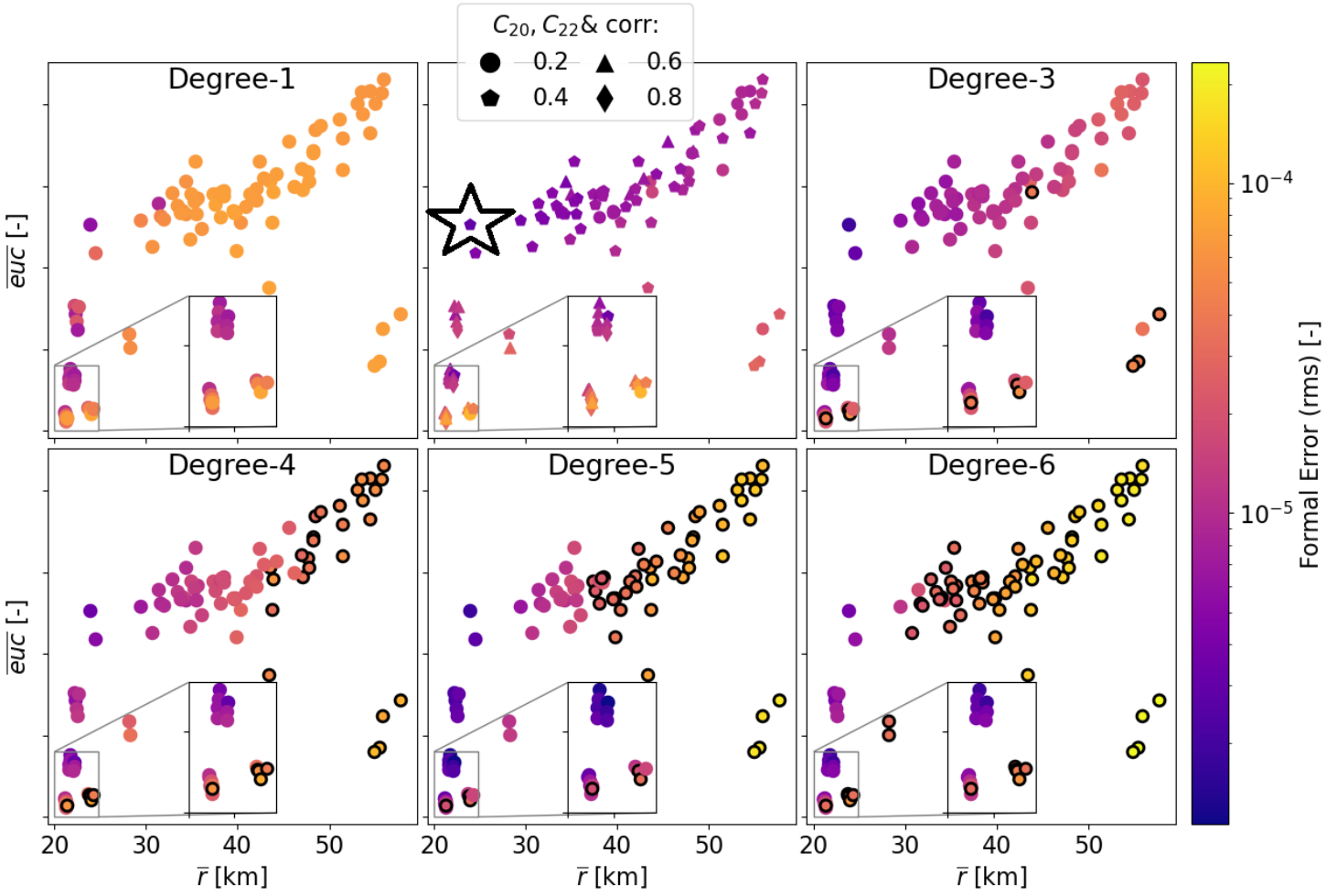

Figure 6: Gravity field recovery via RS at 24h/day tracking capacity. Horizontal and vertical axes indicate coverage and proximity of the orbital solutions. The formal error root-mean-square is grouped per degree. Shapes reflect the correlation between C_{20} and C_{22}, and the circled markers indicate that the formal errors *cross the a-priori* standard deviations. The star denotes the best orbit in terms of accuracy across degrees 1 to 3

the CoM position along y_{BFF} (see Figure 4) features high correlations with the state estimates. This is because this gravitational signature could be misinterpreted as Phobos approaching the spacecraft, since the orbital motion occurs primarily in this (tangential) direction. Nonetheless, degree-1 estimates are actually conservative since the real Phobos will feature more heterogeneity, meaning their signatures will be larger [5].

Degree-2 harmonics are inferred accurately to 10^{-5} (0.001%) for most orbits. In combination with degree-1, these would certainty (dis)prove a heavily fractured or porous compressed interior, and differentiate most ice-rock mixtures generated by Dmitrovskii et al. (2022). Note that C_{21}, S_{21} and S_{22} are excluded as they are of lower scientific importance (consult Section 2.2) and display a smaller signature (see Figure 8) meaning they would exacerbate the formal errors. Here, coverage plays a primary role for both the accuracy and correlation: the lowest planar orbits cannot distinguish C_{20} from C_{22}, as reflected by the markers' shapes. Since the influence of C_{20} is focused at the equator, where most of Phobos' mass is concentrated, this coefficient presents a strong correlation to GM (entries in Figure 7). Still, one has to be careful with generalising correlations along the PF: due to the limited timeline of the mission, coupled with the short arcs of low orbits, the individual orbit geometry has a strong influence on the results.

Degrees 3 to 6 are constrained to 10^{-5} at low altitudes in combination with a good coverage, which is required to capture Phobos' gravity variations at non-equatorial latitudes as these harmonics are located here. It must be reckoned that the inclusion of these terms significantly increases the condition number for the inversion. This is attributed to the fact that degree-2 and 4 coefficients display a similar temporal signature for satel-

[5]The homogeneous shape of Phobos was derived from the control points analysis of Willner et al. (2010) which is tied to the origin of the reference system defining Phobos' ephemeris. Hence the degree-1 coefficients adopted here are small, yet they are not zero (Xian et al. (2012)).

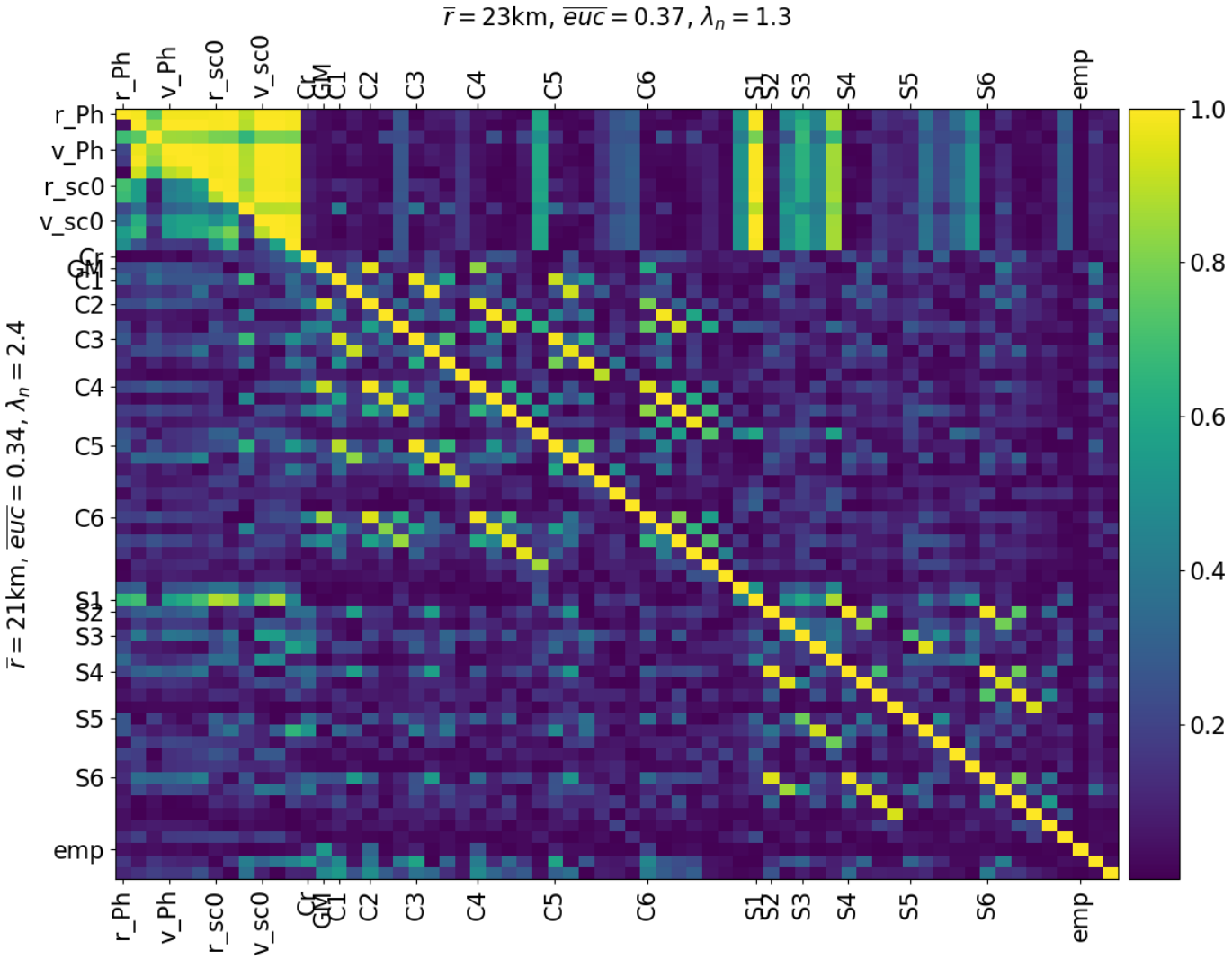

Figure 7: Correlation matrix for (reduced set of) parameters in the RS experiment. Upper-right and lower-left triangles concern the best orbit for the RS and combined experiment, respectively. The tangential component of Phobos' state w.r.t. Mars can best be decorrelated in the lower, planar orbit. The cosine spherical harmonics (2,4), (5,3) and (6,4) with the same order are highly correlated. Landmark positions (not shown here) correlate mainly with the optical biases.

lites in a (near-)circular and (near-)equatorial orbit (Dirkx et al. (2019)), as confirmed by Figure 7. The same behaviour is visible for degrees 3 and 5, as well as degrees 4 and 6 of the same order. The inclusion of additional terms would bias more solutions towards the a-priori values, which should not be further restricted due to the high degree-to-degree variability in the heterogeneous models.

Porosity for a monolithic interior can be accurately described via the RS experiment, as the GM can be constrained to within 0.0001% uniformly across the PF (not shown here). Assuming the same field of view as MEX (18°, Jaumann et al. (2007)) and nadir pointing, we compute the surface fraction that can be mapped via each orbit. We find that the low orbits generally observe 50-75% of the surface, whereas the high orbits map 90% of it. The surface curvature has been neglected, yet this simplification has an limited influence as the orbit altitude is close to the radius of Phobos. For the same radial resolution as OSIRIS-REx's PolyCam (1m scaled from Smith et al. (2013)) this yields a relative volume uncertainty of 0.01%, meaning this is still the dominant error affecting the porosity, provided the sample density obtained from MMX is representative.

Overall, the RS gravity is well suited for recovering Phobos' gravity field, which is encouraging in the prospect of the MMX mission. The best orbit in terms of overall accuracy (denoted by the star in Figure 6) stands at the vertex of the front, and leads to the formal errors plotted in Figure 5. Comparing these percentages to the spherical coefficient overlap between the various interiors (LeMaistre et al. (2019) Figures 12-13) it is concluded that most models can be distinguished, except for the rubble pile and icy "evenly distributed" sub-family. The latter only exhibit significant deviations w.r.t. the homogeneous models at degrees 7 to 9. Nevertheless, porosity can provide additional clues to discriminate the former, if the interior is monolithic.

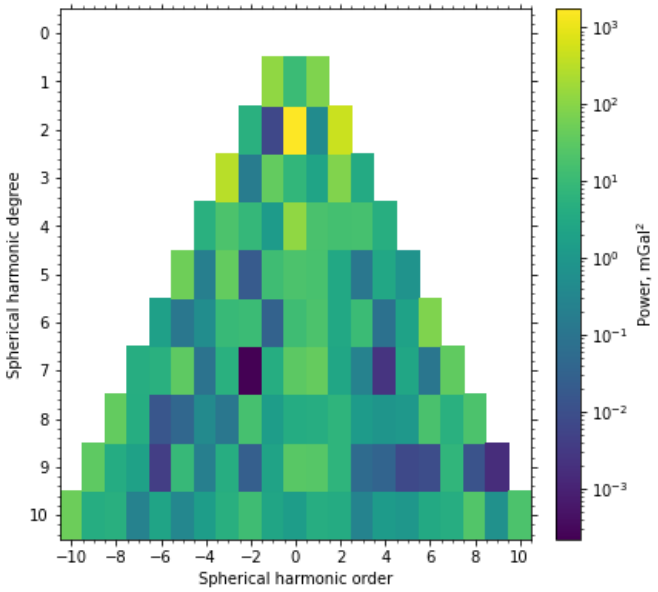

Figure 8: Power spectrum of Phobos' homogeneous gravity field

A two-step sensitivity analysis on the tracking settings was performed to investigate the robustness of the RS experiment. First, the arc duration was extended to test if the inclusion of additional tracking data would favour the estimation of higher harmonics. This was not the case, and instead proved to exacerbate the influence of systematic errors. Shortening the arcs did not yield benefits either: evidently, the gravity field signatures are best captured with 1-2 days of tracking. The present model relies on a state-of-the-art tracking system, with ground stations distributed uniformly around the globe, operating 24/7. Letting aside the associated costs of operation, this configuration is quite optimistic insofar as the spacecraft cannot continuosly be tracked from Earth. In fact, the MMX design team reserves 8h/day for tracking, telecommanding and telemetry downlink (Matsumoto et al. (2021)). Therefore, the complexity of the tracking system was alleviated. One option would be to reduce the number of ground stations from 3 to 2. However, due to planetary occultation by Mars (and visibility conditions at Earth) this may lead to blackout periods. Due the short mission timeline, may unfairly target some arcs more than others. Instead, the tracking time within each arc was reduced to 50% capacity, which mimics the strategy of actual missions whereby observation times are planned ahead to guarantee visibility. Although an average of 12h/day is relatively optimistic for interplanetary missions, it is deemed reasonable during exploratory phases, where a lot of information is gathered on the gravity field for manoeuvre planning. Moreover, this is feasible if high-gain antenna pointing is not required, as is the case for Mars. Interestingly, the tracking time reduction worsens the estimation accuracy by a factor 2 in most cases, which is close to what one might expect from a theoretical point of view (formal errors worsen with $\sqrt{2}$, see Section 5.1), albeit the optical tracking remains unaffected. The accompanying variation in condition number is unordered: for some orbits it worsens due to the reduction in observations, whereas for others it actually improves as a-priori values gain more weight. Since a 12h/day tracking capacity is both competitive and realistic, this setting is selected in the remainder of the experiment.

6.2. Gravity Field Solution with CAI Gradiometry

The two CG reported in Table 4 were tested individually along three instrument orientations, for each orbit in the PF, resulting in a vast set of of experiments. Considering that each estimation involves a degree-10 gravity field, a number of steps had to be taken to condense these into Figure 9.

First, the CAI 1 concept was abandoned as it performed consistently worse than CAI 2 in terms of accuracy. Evidently, its larger measurement volume does not outweigh the superior sensitivity of the latter. Consequently, this suggests that extending the mission timeline would not have a strong influence on the results, as the formal error improvement has reached an asymptotic limit $1/\sqrt{N_{obs}}$. Given that a higher measurement rate is not beneficial, and that the formal errors (for uncorrelated measurements) scale linearly with the instrument's sensitivity (eq. (7)), the estimates shown hereafter will experience a linear improvement as the sensitivity is enhanced. Alternatively one may contemplate relaxing the time required for atomic cooling, which will significantly reduce the power demand in Table 4. Finally, since Figure 6 indicates that RS is highly capable of recovering Phobos' gravity field up to degree-3, only the measurement orientation leading to the highest accuracy for degree-4 and above was selected. With regards to the latter, it was noted that the performance of the cross-track axis is poor, as hypothesised in Section 4.2. The nadir and along-track directions, on the other hand, display a similar efficacy. With this in mind, one may focus on the individual harmonics more attentively.

Degree-1 coefficients are improved by one order of magnitude by means of gradiometric observables, resulting in an accuracy of 10^{-5}. These are not shown here, the reason being as follows. Although theoretically a CoM fix to 1.4m is achievable, realistically, this knowledge will be overshadowed by the uncertainty in Phobos' ephemeris. Thence, for all intents and purposes, this improvement is insignificant from a science perspective. Nonetheless, it is important to note that the correlation which existed in S_{11} for RS has now been removed (the full matrix is reported in Appendix B).

Degree-2 harmonics gain a factor 10-15 in accuracy w.r.t. the RS-only case across the PF, yielding an accuracy below 10^{-7}. Whether or not this enhancement will contribute to the science goals remains to be further investigated. Perhaps the C_{22} estimate would be sufficient to discern k_2 as outlined in Section 2.3. Comparing the markers' shapes with Figure 6, it is evident that CG is highly effective for decorrelating C_{20} and C_{22}.

The most significant contribution of gradiometry resides in the retrieval of the gravity spectrum at *high-degrees*. The retrieval accuracy ranges from 10^{-5} to 10^{-6} (0.01%) for the orbits which guarantee a favourable correlation and proximity. Other orbits lead to high errors for degrees 7 to 9 (<100%) as reflected by the circled markers. This is mainly attributed to the indistinguishable low-power coefficients that are present at these degrees (see Figure 8). The condition number for the gravity field terms is between 10^5 and 10^7, namely two orders

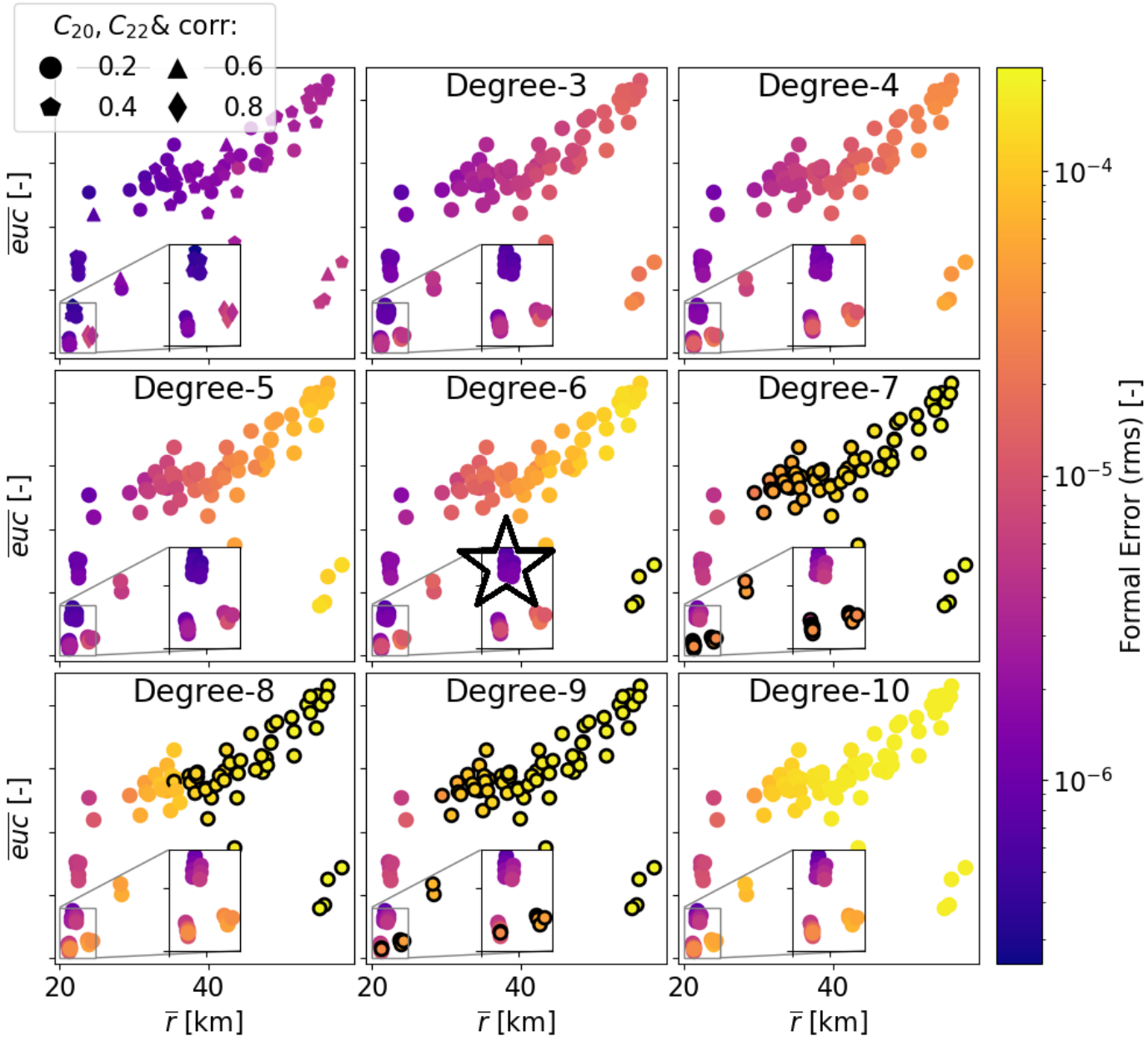

Figure 9: Gravity field recovery for combined experiment. RS tracking is 12/h day, CG sensitivity is σ_γ =0.462mE$\sqrt{Hz}$ with measurements every 11s. Shapes reflect the correlation between C_{20} and C_{22}. In contrast to Figure 6, here all the formal errors stay below the a-priori standard deviations, hence the circled markers indicate that the formal errors *cross the homogeneous* values. The star denotes the best (family of) orbits in terms of accuracy across degrees 4 to 10.

worse than for RS, yet tolerable nonetheless. As the number of estimated coefficients grows by a factor 2.5, this increase is unsurprising. Once again, the primary correlations affect the cosine harmonics of the same order, with the addition of degrees 7 and 9, as well as degrees 8 and 10. Finally, whereas RS presents the lowest correlations at close proximity, for CG this occurs at the vertex of the PF. Evidently, a uniform coverage gains importance if the full spectrum is to be sampled.

The superiority of CG over RS in recovering the finer harmonics was hypothesised by Bills and Ermakov (2019), who derive analytical expressions to compare the error spectra of both methods. These rest on a number of simplifying assumptions, yet they serve to illustrate the scaling of formal errors as

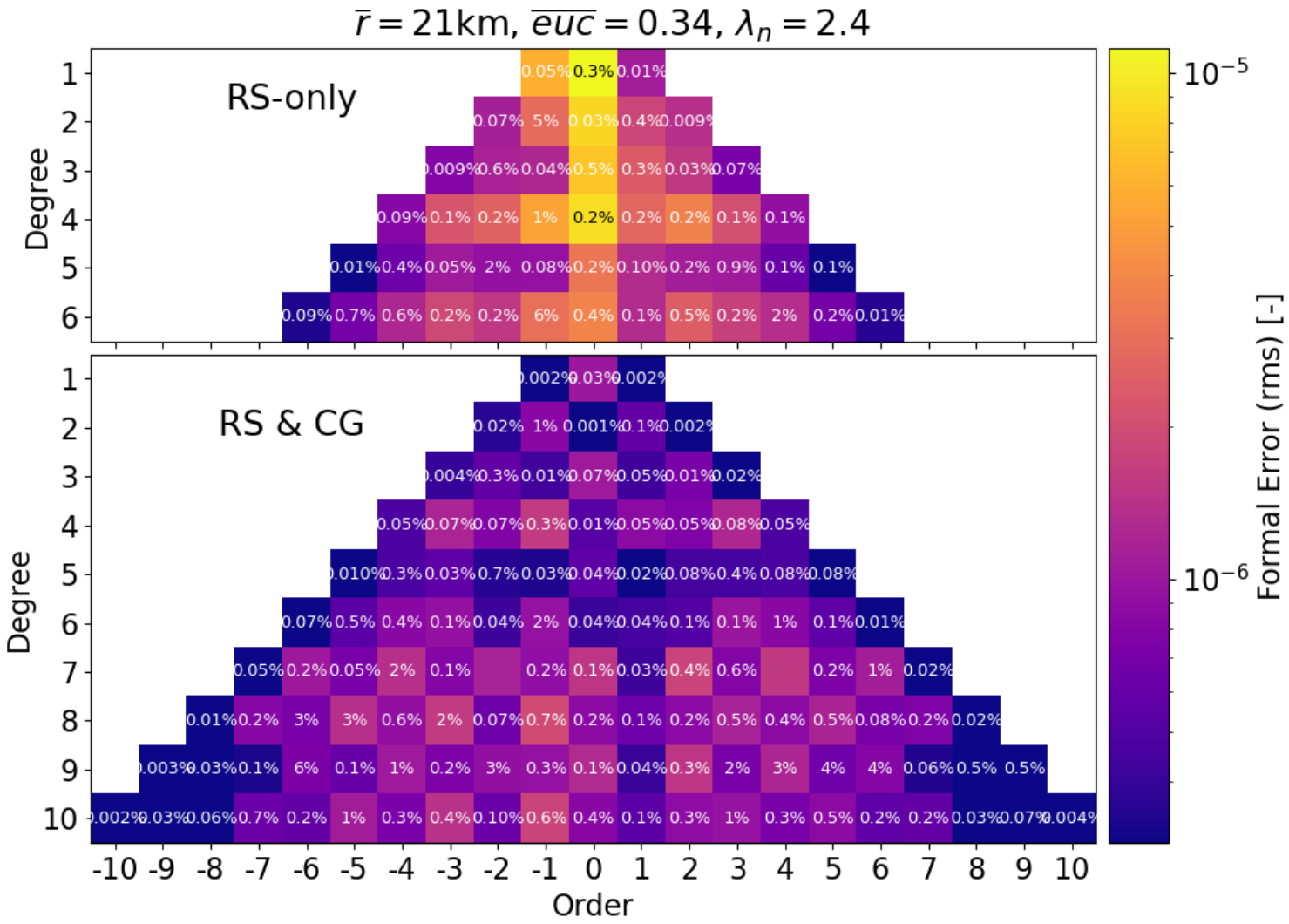

Figure 10: Formal errors for the gravity spectrum obtained via the best orbit in the combined experiment, marked by a star in Figure 9. This is more unstable compared to Figure 5, but the gain in accuracy across the entire spectrum outweighs the associated maintenance costs. Note that the true errors for the top pyramid could increase by a factor 2-3 due to the influence of systematic uncertainties (see Section 6.4).

a function of harmonic degree n:

$$\frac{\sigma_n^{grad}}{\sigma_n^{RS}} = \left(\frac{\sigma_\gamma}{\sigma_{\dot{\rho}}}\right)\left(\frac{r}{n_{orb}}\right)\left(\frac{\sqrt{O(n^2)}}{\sqrt{O(n^4)}}\right) \tag{10}$$

with $\sigma_{\dot{\rho}}$ the Doppler noise, n_{orb} the spacecraft mean motion and $O(n^x)$ a power series of leading order x. This final term confirms the superiority of gradiometry at finer wavelengths (notice how the accuracy does not drop across Figure 9). The middle term in eq. (10) suggests that gradiometry is harshly affected by an increase in orbital altitude, which was the reason for GOCE's low altitude ($\approx 259km$) in spite of the adverse atmospheric environment. As a physical analogy, one can imagine that RS is incapable of detecting finer wavelengths, as these do not impart detectable signatures on the trajectory. Conversely, by differencing two closely-spaced accelerations, CG maintains a strong sensitivity to the high-frequencies of the gravitational signal.

The gravity field solution obtained via the best orbit in the combined experiment (star in Figure 9) is shown in Figure 10. The accuracy gain from CG is immediately visible from the shading of the bottom pyramid. With this configuration, all overlapping factors between the heterogeneous and homogeneous interiors of LeMaistre et al. (2019) can be resolved. In combination with shape models, Phobos' internal mass distributions would be inferred, settling its origin once in for all.

6.3. *Contribution of Tracking Data Types*

The design of the onboard tracking segment must weigh logistical constraints and science return, thence one should investigate the added contribution of each data type. This is shown

in Figure 11 whereby the formal errors have been normalised w.r.t. the "nominal" Doppler-only case, due the different physical scales of the estimated parameters. At first glance one learns that the inclusion of other data types yields a maximum improvement of 10% w.r.t. the nominal case for all parameters aside from the landmark positions, which can only be obtained via optical measurements (hence these are shown separately).

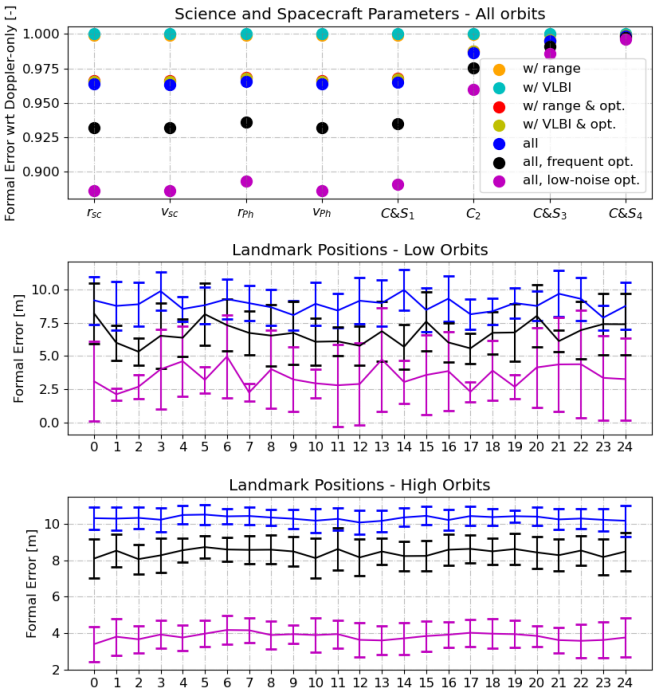

Figure 11: Top: orbit-averaged contribution of tracking data types on formal errors w.r.t. Doppler-only case for all parameters. Others: influence of optical instrument performance (noise and image frequency) on landmark position accuracy. Markers and lines show mean, bars show maximum/minimum values.

The superiority of Doppler data for recovering the geodesic parameters is evident. This is due to the small characteristic period of the gravity signal, hence its spherical harmonic signatures can only be observed in closely-spaced Doppler measurements (Dirkx (2015)). This effect exacerbates for the higher degrees, which feature a smaller period, as reflected by the narrowing of the markers. Another reason contributing to the superiority of Doppler is related to the observational geometry. The orbit planes of the spacecraft are close to that of Phobos, featuring small inclinations ($< 30°$) with respect to Mars' equator. Consequently, the orbit plane is viewed edge-on from the Earth, meaning velocity changes are effectively captured in the line-of-sight direction. This effect is more pronounced for the low, mostly planar orbits hence the higher estimation accuracy (see Figure 6). The addition of VLBI and range ("hidden" behind the former) yield no benefit. Since VLBI measures linear position perpendicular to the line-of-sight with an accuracy in the order of 100m, its contribution to the gravity field coefficients is negligible (Dirkx et al. (2018)). In light of these considerations, range and VLBI data were omitted in this experiment.

Optical landmark tracking, on the other hand, is extremely useful in improving the state of the spacecraft and Phobos. Since the CoF can better be distinguished from the CoM, this is accompanied by an improvement in the degree-1 harmonics, which also propagates in the higher-degree spectrum. For the nominal camera performance (blue markers) a 3% improvement in Phobos' state translates to a 2% improvement in C_{20} and C_{22}. This finding agrees with the experiment by Yang et al. (2019), who (inversely) determine that a 2% improvement in Phobos' CoF position reduces the uncertainty of all degree-2 coefficients by 0.52%. In contrast to Doppler data, the performance of optical tracking has been found to depend strongly on the orbit altitude. In the low orbits many landmarks are missed hence their estimation accuracy is not uniform, as reflected by the error bars in the middle plot. In contrast, the visibility entailed by the high orbits allows capturing the same landmark multiple times. This is highly beneficial for deriving shape and rotational properties as it enables "differenced" landmark observations independent of a-priori shape models (Goossens et al. (2021)). At high orbits, the camera performance plays a stronger role because the noise (particularly the bias) scales with altitude. This is harder to estimate with Doppler data, which is sensitive to the radial distance from Phobos, as its gravity influence is now weaker. It is therefore not surprising that OSIRIS-REx at Bennu is fitted with three cameras, each tailored to operate in a specific mission phase. The high orbits perform global mapping and shape determination while the closer ones focus on sample-site characterisation (Smith et al. (2013)). To mimic this behaviour and enforce competitiveness across the orbits, the optical performance was adjusted with altitude: low orbits capture more images, whereas high orbits benefit from a lower noise.

6.4. *Influence of Consider Parameters*

The relative degradation in estimation accuracy due to the influence of systematic uncertainties is reported in Figure 12. Here, the averaged values across the PF are shown (since the trend is similar) although it should be noted that higher orbits are worse affected as their overall formal errors are larger.

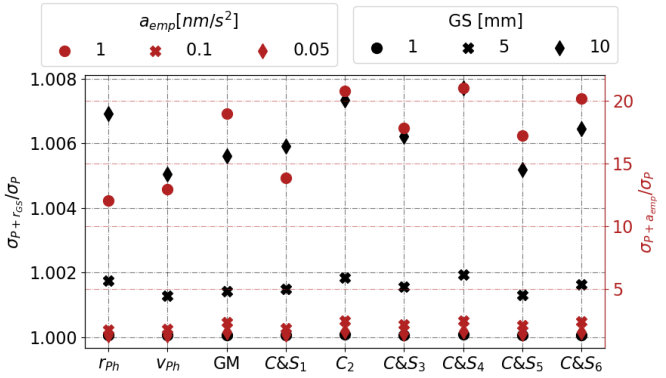

Figure 12: Formal error ratio: with and without consider parameters, namely ground station position (left axis) and empirical acceleration (right axis)

Evidently the ground station position uncertainty has a very limited influence. This is primarily due to the fact that absolute

measurements (range and VLBI) have been disregarded. The only concern is Phobos' state estimate (also affecting the low degree harmonics) that could degrade by ≈1% for an uncertainty of $1cm$. Nonetheless, the latter is rather pessimistic of what can be achieved nowadays (Dirkx et al. (2014) use $5mm$). Moreover, the current setup employs a single ground station at a time, which amplifies the effect of this error.

The risk associated with the mismodelling of empirical accelerations is severe, with formal errors degrading by a factor 2-3 in the best-case scenario. Interestingly, this matches the empirical (a-posteriori) true-to-formal error ratios for small-body missions to Eros (Miller et al. (2002)) and Vesta (Konopliv et al. (2014)) which were 2 and 3 for gravity field parameters, respectively. The worst-case scenario aggravates the errors by an order of magnitude, which is similar to the ratio determined for Mars orbiters (Genova et al. (2016)) where atmospheric drag is responsible for systematic uncertainties. This stresses the need for a high-fidelity modelling of non-conservative forces (mainly the radiation pressure) as this has a confounding influence in small-body environments, particularly for lighter spacecraft. Here, the spacecraft dimensions are undefined, hence empirical accelerations are included as regular parameters to prevent the formal errors from being overly optimistic. Generally, in the low orbits the along- and cross-track empirical accelerations correlate with the radiation pressure (see Figure 7, bottom left) as their influence is confounded with gravity. At high orbits the effect of radiation pressure is more distinguishable. This is why for OSIRIS-REx the orientation and thermal diffusive properties were detailed so finely that the estimation of empirical accelerations could be omitted in the lowest orbit, as to avoid masking the gravity signal (Scheeres et al. (2019a)).

Two further experiments were pursued. Firstly, the amplitude of empirical accelerations was reduced by an order of magnitude ($0.1nm/s^2$). This had little effect on the results, as these could still be resolved to 1%, and their systematic influence remained unvaried. Finally, the arc lengths were extended to the full duration of the mission. As expected, this severely aggravated the systematic errors (by a factor 10) due to the build-up of non-conservative forces. One may therefore conclude that empirical accelerations must be modelled to below the nm/s^2 level as these constitute a significant threat to the RS experiment, especially for the higher orbits. If this is not possible, one must resort to a gradiometer for direct gravity measurements, or an accelerometer to measure stochastic forces and remove their confounding influence in orbit determination, as done for Bepi-Colombo at Mercury (Genova et al. (2011)).

6.5. *Ephemeris and Libation*

A precise recovery of Phobos's gravity field must be accompanied by an exhaustive modelling of its ephemeris, insofar as any uncertainty in the latter will cause significant aliasing in the spherical coefficients (Yang et al. (2019)). It is found that Phobos' radial and tangential position w.r.t. Mars. can be constrained to $1m$ for the planar orbits. These are also best suited for decorrelating Phobos' velocity from its tangential position (see Figure 7). The estimates are hardly affected by a reduced tracking time, as they rely primarily on optical observables. Higher-coverage orbits are more effective in reducing the out-of-plane uncertainties in Phobos' orbit, nonetheless, these have a limited influence on the evolution of its ephemeris.

Given that the dynamics of Phobos are mostly linear, the formal error on its state is propagated via state transition matrices. One might therefore expect a linear relationship between the formal error at t_0 and the ephemeris uncertainty at time t. Nonetheless, as illustrated by eq. (4), any mismodelling in its libration and gravity field will exacerbate over time, degrading the ephemeris, particularly for the radial and tangential components. Conversely, strong estimates for these parameters would consolidate the ephemeris via dynamical adjustment, as performed by Jacobson and Lainey (2014); Lainey et al. (2021).

Overall, modelling the long-term improvement in Phobos' ephemeris requires data fusion in the form of past astronomical observations, which is beyond the scope of this analysis. Nevertheless, Figure 11 illustrates that optical imagery is highly effective in constraining landmark positions, even for a short mission duration of one week, which would enable a control point analysis (as done in Burmeister et al. (2018)) to provide an independent measurement on libration. Coupled with the strong accuracy can be achieved on the $C_{2,0}$ and $C_{2,2}$ harmonics, this provides confidence in the ability to reinforce the ephemeris of this complex yet fascinating moon.

7. Conclusions

This work addresses the potential of CG as a means of strengthening the RS gravity field experiment, using Phobos as a science case. The interior models by LeMaistre et al. (2019) served as guidance for outlining the key geodesic observables needed to constrain Phobos' origin. The proximity and coverage of the orbital solutions are identified as being strong drivers for the estimation quality, yet these metrics clash with the orbital stability (see Figure 2). Thence, high-fidelity simulations must verify their maintainability in the face of strong perturbations associated with Phobos' dynamical environment.

Provided that empirical accelerations can be modelled below the nm/s^2 level, RS is able to infer the 6x6 spherical harmonic spectrum to an accuracy of 0.1-1% w.r.t. the homogeneous interior values, as shown in Figure 5. If this correlates to a density anomaly beneath the Stickney crater, RS be sufficient to constrain Phobos' origin, especially if supported by a strong estimate for porosity and libration. Yet, a significant overlap is present in the harmonics for the rubble pile and icy moon interiors (or a combination thereof), making their spectra indistinguishable up to degree-6. The most significant deviations occur at degrees 7 to 9, which can only be detected via CG flying at a low orbit. As illustrated in Figure 10, this would enable recovering the 10x10 spectrum to an accuracy below 0.1% for most coefficients, constraining Phobos' origin once in for all. Nonetheless, technological advancements will be needed to alleviate the power and weight entailed by CG configurations as to enhance their competitiveness in an instrument trade-off.

Finally, it has been qualitatively discussed that the proposed mission is set to enhance the dynamical fitting of Phobos's ephemeris by reducing the uncertainties associated with C_{20}

and C_{22} and providing an independent estimate for libration. This would facilitate a return to the moon and provide additional clues on to its orbital evolution.

The dynamical environment of Phobos is quite extreme, but in many ways similar to that of other moons in the solar system. The advent of the JUpiter ICy moons Explorer mission (JUICE) (Grasset et al. (2013)) will characterise the icy moons' gravitational spectra at higher degrees, where the contribution of CG looks most promising. To this end, the methodology outlined in this work may serve as a foothold to contemplate the role of CG in bolstering the geodesic investigation of future exploratory missions to small moons, particularly those of the Giant planets, which are targets for robotic exploration in the coming decades.

References

Bagheri, A., et al., 2021. Dynamical evidence for Phobos and Deimos as remnants of a disrupted common progenitor. Nature Astronomy doi:10.1038/s41550-021-01306-2.

Baresi, N., Dei Tos, D.A., Ikeda, H., Kawakatsu, Y., 2020. Trajectory design and maintenance of the martian moons exploration mission around Phobos. Journal of Guidance, Control, and Dynamics 0, 1–12. URL: https://doi.org/10.2514/1.G005041.

Barrett, B., et al., 2013. Mobile and remote inertial sensing with atom interferometers. arXiv: Atomic Physics 188, 493–555.

Bienstock, B., 2020. Mass change DS DO community telecon. URL: https://science.nasa.gov/science-red/s3fs-public/atoms/files/Mass-Change-DS-DO-Study-Introduction-TAGGED.pdf.

Bills, B., Ermakov, A., 2019. Simple models of error spectra for planetary gravitational potentials as obtained from a variety of measurement configurations. Planetary and Space Science 179, 104744. URL: http://www.sciencedirect.com/science/article/pii/S003206331830432X.

Bongs, K., et al., 2019. Taking atom interferometric quantum sensors from the laboratory to real-world applications. Nature Reviews Physics 1. doi:10.1038/s42254-019-0117-4.

Burmeister, S., et al., 2018. Determination of Phobos' rotational parameters by an inertial frame bundle block adjustment. J Geod , 963–973doi:https://doi.org/10.1007/s00190-018-1112-8.

Campagnola, S., Yam, C.H., Tsuda, Y., Ogawa, N., Kawakatsu, Y., 2018. Mission analysis for the Martian Moons Explorer (MMX) mission. Acta Astronautica 146, 409–417. doi:https://doi.org/10.1016/j.actaastro.2018.03.024.

Canup, R., Salmon, J., 2018. Origin of Phobos and Deimos by the impact of a Vesta-to-Ceres sized body with Mars. Science Advances 4. doi:10.1126/sciadv.aar6887.

Carraz, O., Siemes, C., Massotti, L., Haagmans, R., Silvestrin, P., 2014. A Spaceborne Gravity Gradiometer Concept Based on Cold Atom Interferometers for Measuring Earth's Gravity Field. Microgravity Science and Technology 26. doi:10.1007/s12217-014-9385-x.

Chen, H., Canalias, E., Hestroffer, D., Hou, X., 2020. Effective stability of quasi-satellite orbits in the spatial problem for Phobos exploration. Journal of Guidance, Control, and Dynamics 43, 2309–2320. doi:10.2514/1.G004911, arXiv:https://doi.org/10.2514/1.G004911.

Devani, D., et al., 2020. Gravity sensing: cold atom trap onboard a 6U cubesat. CEAS Space Journal 12, 539–549. doi:10.1007/s12567-020-00326-4.

Dirkx, D., 2015. Interplanetary laser ranging:A nalysis for implementation in planetary science missions. PhD dissertation. Delft University of Technology.

Dirkx, D., Mooij, E., Root, B., 2019. Propagation and estimation of the dynamical behaviour of gravitationally interacting rigid bodies. Astrophysics and Space Science 364. doi:10.1007/s10509-019-3521-4.

Dirkx, D., Vermeersen, L., Noomen, R., Visser, P., 2014. Phobos laser ranging: Numerical geodesy experiments for martian system science. Planetary and Space Science 99, 84–102. doi:https://doi.org/10.1016/j.pss.2014.03.022.

Dirkx, D., et al., 2018. Laser and radio tracking for planetary science missions: a comparison. Journal of Geodesy 93, 2405–2420. doi:10.1007/s00190-018-1171-x.

Dmitrovskii, A.A., Khan, A., Boehm, C., Bagheri, A., van Driel, M., 2022. Constraints on the interior structure of Phobos from tidal deformation modeling. Icarus 372, 114714. doi:https://doi.org/10.1016/j.icarus.2021.114714.

Douch, K., Wu, H., Schubert, C., Müller, J., Pereira dos Santos, F., 2018. Simulation-based evaluation of a cold atom interferometry gradiometer concept for gravity field recovery. Advances in Space Research 61, 1307–1323. doi:https://doi.org/10.1016/j.asr.2017.12.005.

Duev, D.A., et al., 2016. Planetary radio interferometry and doppler experiment (pride) technique: A test case of the mars express Phobos fly-by. A&A 593, A34. doi:10.1051/0004-6361/201628869.

D'Amico, G., Rosi, G., Zhan, S., Cacciapuoti, L., Fattori, M., Tino, G., 2017. Canceling the gravity gradient phase shift in atom interferometry. Physical Review Letters 119. doi:10.1103/PhysRevLett.119.253201.

Elliott, E., Krutzik, M., Williams, J., Thompson, R., Aveline, D., 2018. NASA's Cold Atom Lab CAL: system development and ground test status. npj Microgravity 4. doi:10.1038/s41526-018-0049-9.

Ermakov, A., Bills, B., 2018. Power laws of topography and gravity spectra of the solar system bodies: Topography and gravity power laws. Journal of Geophysical Research: Planets 123. doi:10.1029/2018JE005562.

ESA, 2018. Study of a CAI gravity gradiometer sensor and mission concepts, preliminary design: Reiteration. doc number: CAI-TN3.

Fayolle, M., Dirkx, D., Lainey, V., Gurvits, L., Visser, P., 2021. Coupled and decoupled strategies for spacecraft's and natural bodies' state estimation - application to the JUICE mission. EPSC Abstracts doi:https://doi.org/10.5194/epsc2021-364.

Freeden, W., Nashed, M., Sonar, T., 2015. Handbook of Geomathematics: Second Edition. doi:10.1007/978-3-642-54551-1.

Frommknecht, B., Lamarre, D., Meloni, M., Bigazzi, A., Floberghagen, R., 2011. GOCE level 1b data processing. Journal of Geodesy 85, 759–775. doi:10.1007/s00190-011-0497-4.

Genova, A., Goossens, S., Lemoine, F.G., Mazarico, E., Neumann, G.A., Smith, D.E., Zuber, M.T., 2016. Seasonal and static gravity field of Mars from MGS, Mars Odyssey and MRO radio science. Icarus 272, 228–245. doi:https://doi.org/10.1016/j.icarus.2016.02.050.

Genova, A., Marabucci, M., Iess, L., 2011. Mercury radio science experiment of the mission BepiColombo.

Goossens, S., Rowlands, D.D., Mazarico, E., et al., 2021. Mass and shape determination of (101955) Bennu using differenced data from multiple OSIRIS-REx mission phases. The Planetary Science Journal 2, 219. URL: https://doi.org/10.3847/psj/ac26c4, doi:10.3847/psj/ac26c4.

Grasset, O., Dougherty, M., Coustenis, A., Bunce, E., Erd, C., et al., 2013. Jupiter icy moons explorer (JUICE): An ESA mission to orbit Ganymede and to characterise the Jupiter system. Planetary and Space Science 78, 1–21. doi:10.1016/j.pss.2012.12.002.

Gross, C., 2012. Spin squeezing, entanglement and quantum metrology with Bose–Einstein condensates. Journal of Physics B: Atomic, Molecular and Optical Physics 45, 103001. doi:10.1088/0953-4075/45/10/103001.

Guo, X., Yan, J., Andert, T., Yang, X., Pätzold, M., Hahn, M., Ye, M., Liu, S., Li, F., Barriot, J.P., 2021. A lighter core for Phobos? Astronomy and Astrophysics 651. doi:10.1051/0004-6361/202038844. cited By 0.

Haagmans, R., Siemes, C., Massotti, L., Carraz, O., Silvestrin, P., 2020. Esa's next-generation gravity mission concepts. Rendiconti Lincei. Scienze Fisiche e Naturali 31. doi:10.1007/s12210-020-00875-0.

Hauth, M., Freier, C., Schkolnik, V., Peters, A., Wziontek, H., Schilling, M., 2014. Atom interferometry for absolute measurements of local gravity. Proceedings of the International School of Physics "Enrico Fermi" 188, 557–586. doi:10.3254/978-1-61499-448-0-557.

Iess, L., Di Benedetto, M., James, N., Mercolino, M., Simone, L., Tortora, P., 2014. Astra: Interdisciplinary study on enhancement of the end-to-end accuracy for spacecraft tracking techniques. Acta Astronautica 94, 699–707. doi:10.1016/j.actaastro.2013.06.011.

Jacobson, R., Lainey, V., 2014. Martian satellite orbits and ephemerides. Planetary and Space Science 102, 35 – 44. doi:https://doi.org/10.1016/j.pss.2013.06.003. Phobos.

Jaumann, R., Neukum, G., Behnke, T., Duxbury, T., Eichentopf, K., Flohrer, J., et al., 2007. The high-resolution stereo camera (HRSC) experiment on Mars EXpress: Instrument aspects and experiment conduct from interplanetary

cruise through the nominal mission. Planetary and Space Science 55, 928–952. doi:https://doi.org/10.1016/j.pss.2006.12.003.
Kaula, W.M., 1966. Theory of Satellite Geodesy : Applications of Satellites to Geodesy. Dover Publications.
Konopliv, A., Park, R., Folkner, W., 2016. An improved JPL mars gravity field and orientation from mars orbiter and lander tracking data. Icarus 274. doi:10.1016/j.icarus.2016.02.052.
Konopliv, A., et al., 2018. The Ceres gravity field, spin pole, rotation period and orbit from the dawn radiometric tracking and optical data. Icarus 299, 411–429. doi:https://doi.org/10.1016/j.icarus.2017.08.005.
Konopliv, A.S., et al., 2014. The Vesta gravity field, spin pole and rotation period, landmark positions, and ephemeris from the dawn tracking and optical data. Icarus 240. doi:https://doi.org/10.1016/j.icarus.2013.09.005.
Kosek, W., Popinski, W., Wnek, A., Sosnica, K., Zbylut-Gorska, M., 2020. Analysis of systematic errors in geocenter coordinates determined from GNSS, SLR, DORIS, and GRACE. Pure and Applied Geophysics 177. doi:10.1007/s00024-019-02355-5.
Kovachy, T., Hogan, J.M., Sugarbaker, A., Dickerson, S.M., Donnelly, C.A., Overstreet, C., Kasevich, M.A., 2015. Matter wave lensing to picokelvin temperatures. Phys. Rev. Lett. 114, 143004. doi:10.1103/PhysRevLett.114.143004.
Lainey, V., Pasewaldt, A., Robert, V., Rosenblatt, P., Jaumann, R., Oberst, J., Roatsch, K., Willner, R., Ziese, W., 2021. Mars moon ephemerides after 14 years of mars express data. Astronomy & Astrophysics doi:https://doi.org/10.1051/0004-6361/202039406.
Lambeck, K., 1982. The earth's variable rotation: Geophysical causes and consequences. 449 pp. isbn 0 521 22769 0. Geological Magazine 119, 219–220. doi:10.1017/S0016756800025929.
LeMaistre, S., Rivoldini, A., Rosenblatt, P., 2019. Signature of Phobos' interior structure in its gravity field and libration. Icarus 321, 272 – 290. doi:https://doi.org/10.1016/j.icarus.2018.11.022.
Lissauer, J.J., de Pater, I., 2013. Cambridge University Press.
Matsumoto, K., et al., 2021. MMX geodesy investigations: science requirements and observation strategy (unpublished). Earth, Planets and Space .
Miller, J., et al., 2002. Determination of shape, gravity, and rotational state of asteroid 433 eros. Icarus 155, 3 – 17. doi:https://doi.org/10.1006/icar.2001.6753.
Montenbruck, O., Gill, E., 2000. Satellite Orbits: Models, Methods and Applications. Springer-Verlag Berlin Heidelberg.
Nallapu, R., et al., 2020. Trajectory design of perseus: A cubesat mission concept to Phobos. Aerospace 7, 1–31. doi:10.3390/aerospace7120179.
Pajola, M., et al., 2013. Phobos as a d-type captured asteroid, spectral modeling from 0.25 to 4.0μm. The Astrophysical Journal 777, 127. doi:10.1088/0004-637X/777/2/127.
Park, R., Vaughan, A., Konopliv, A., Ermakov, A., Mastrodemos, N., Castillo-Rogez, J., et al., 2019. High-resolution shape model of Ceres from stereophotoclinometry using DAWN imaging data. Icarus 319, 812–827. doi:https://doi.org/10.1016/j.icarus.2018.10.024.
Pieters, C., 2010. Compositional implications of the color of Phobos. First Moscow solar system symposium 123, 43 (abstract).
Pushparaj, N., Baresi, N., Ichinomiya, K., Kawakatsu, Y., 2021. Transfers around Phobos via bifurcated retrograde orbits: Applications to martian moons exploration mission. Acta Astronautica 181, 70–80. doi:https://doi.org/10.1016/j.actaastro.2021.01.016.
Pätzold, M., et al., 2014. Phobos mass determination from the very close flyby of Mars Express in 2010. Icarus 229, 92 – 98. URL: http://www.sciencedirect.com/science/article/pii/S0019103513004508.
Rosenblatt, P., 2011. The origin of the martian moons revisited. Astron Astrophys Rev 19. doi:https://doi.org/10.1007/s00159-011-0044-6.
Roura, A., Zeller, W., Schleich, W.P., 2014. Overcoming loss of contrast in atom interferometry due to gravity gradients 16, 123012. doi:10.1088/1367-2630/16/12/123012.
Rummel, R., Yi, W., Stummer, C., 2010. GOCE gravitational gradiometry. Journal of Geodesy 85, 777–790. doi:10.1007/s00190-011-0500-0.
Safranov, V.S., Pechernikova, G.V., Ruskol, E.L., Vitjaev, A.V., 1986. Protosatellite Swarms. University of Arizona Press. pp. 89–116. URL: http://www.jstor.org/stable/j.ctv1v3gr3r.7.
Scheeres, D., 2012. Orbital Motion in Strongly Perturbed Environments. Springer.
Scheeres, D., Mcmahon, J., French, A., Brack, D., Chesley, S., Farnocchia, D., Takahashi, Y., et al., 2019a. The dynamic geophysical environment of (101955) Bennu based on osiris-rex measurements. Nature Astronomy 3, 1. doi:10.1038/s41550-019-0721-3.
Scheeres, D., Van wal, S., Olikara, Z., Baresi, N., 2019b. Dynamics in the Phobos environment. Advances in Space Research 63, 476–495. doi:https://doi.org/10.1016/j.asr.2018.10.016.
Siemes, C., 2008. Digital Filtering Algorithms for Decorrelation within Large Least Squares Problems. PhD dissertation. University of Bonn.
Siemes, C., 2012. GOCE gradiometer calibration and level 1b data processing.
Siemes, C., Rexer, M., Haagmans, R., 2019. GOCE star tracker attitude quaternion calibration and combination. Advances in Space Research 63, 1133–1146. doi:https://doi.org/10.1016/j.asr.2018.10.030.
Smith, P., Rizk, B., Kinney, E., Fellows, C., Drouet d'Aubigny, C., Merrill, C., 2013. The osiris-rex camera suite (ocams). In Lunar and Planetary Institute Science Conference Abstracts 44, 1690–.
Thornton, C.L., Border, J.S., 2003. Range and Doppler Tracking Observables. John Wiley & Sons, Ltd. pp. 9–46. URL: https://onlinelibrary.wiley.com/doi/abs/10.1002/0471728454.ch3.
Trimeche, A., Battelier, B., Becker, D., Bertoldi, A., Bouyer, P., Braxmaier, C., et al., 2019. Concept study and preliminary design of a cold atom interferometer for space gravity gradiometry. Classical and Quantum Gravity 36. doi:10.1088/1361-6382/ab4548.
Usui, T., Bajo, K.I., Fujiya, W., Furukawa, Y., Koike, M., Miura, Y., Sugahara, H., Tachibana, S., Takano, Y., Kuramoto, K., 2020. The importance of Phobos sample return for understanding the mars-moon system. Space Science Reviews 216. doi:10.1007/s11214-020-00668-9. cited By 3.
Werner, R.A., 1997. Spherical harmonic coefficients for the potential of a constant-density polyhedron. Computers and Geosciences 23, 1071 – 1077. doi:10.1016/S0098-3004(97)00110-6.
Werner, R.A., Scheeres, D.J., 1996. Exterior gravitation of a polyhedron derived and compared with harmonic and mascon gravitation representations of asteroid 4769 castalia. Celestial Mechanics and Dynamical Astronomy 65, 313–344. doi:10.1007/BF00053511.
Willner, K., Oberst, J., Hussmann, H., Giese, B., Hoffmann, H., Matz, K.D., Roatsch, T., Duxbury, T., 2010. Phobos control point network, rotation, and shape. Earth and Planetary Science Letters 294, 541–546. doi:https://doi.org/10.1016/j.epsl.2009.07.033.
Willner, K., et al., 2014. Phobos' shape and topography models. Planetary and Space Science 102, 51–59. doi:https://doi.org/10.1016/j.pss.2013.12.006. Phobos.
Witasse, O., Duxbury, T., Chicarro, A., Altobelli, N., Andert, T., Aronica, A., et al., 2014. Mars express investigations of Phobos and Deimos. Planetary and Space Science 102, 18–34. doi:https://doi.org/10.1016/j.pss.2013.08.002. Phobos.
Xian, S., Konrad, W., Jürgen, O., JinSong, P., Shuhua, Y., 2012. Working models for the gravitational field of Phobos. Science China: Physics, Mechanics and Astronomy 55, 358–364. doi:10.1007/s11433-011-4606-4.
Yang, X., et al., 2019. The low-degree gravity field of Phobos from two Mars Express flybys, in: European Planetary Science Congress (EPSC-DPS Joint meeting), Genève, Switzerland. pp. EPSC–DPS2019–1521. URL: https://hal.archives-ouvertes.fr/hal-03155678.
Yang, Y., Yan, J., Guo, X., He, Q., Barriot, J., 2020. An elastic model of Phobos´libration. A&A 636, A27. doi:10.1051/0004-6361/202037446.
Yu, N., Kohel, J., Kellogg, J., Maleki, L., 2006. Development of an atom-interferometer gravity gradiometer for gravity measurement from space. Applied Physics B 84, 647–652. doi:10.1007/s00340-006-2376-x.

Appendix A. Influence of External Noise on Gradiometry

Given that the main gravity signal is that of Mars, from which the modulation due to Phobos must be extracted, one must consider the noise on the gravity gradients associated with Mars' gravity field. To this end, a covariance propagation is set up:

$$\boldsymbol{P}(V_{ij}) = \boldsymbol{H}\boldsymbol{P}(C_{nm}, S_{nm})\boldsymbol{H}^T \tag{A.1}$$

noting that the Jacobian is computed with respect to Mars' gravity field. Figure A.13 illustrates that the dominant noise contribution arises from the orbital eccentricity, acting via the C_{00}

term, as the spacecraft comes closer to Mars. The nadir (z) axis is the worst affected as it is aligned with Mars hence it receives the strongest signal. Still, the noise is far below the gradiometric sensitivity ($\sigma_\gamma \approx 10^{-12} s^{-2}$). A secondary noise source arises from the uncertainty in the spacecraft state with respect to Mars. This is assessed as follows:

$$\boldsymbol{P}(V_{ij}) = (\boldsymbol{H} - \boldsymbol{H_{pert.}})[C_{nm}, S_{nm}] \tag{A.2}$$

whereby the perturbed Jacobian is afflicted by the uncertainty in the spacecraft state w.r.t. Mars, obtained via formal error propagation. This too is orders below the gradiometric sensitivity, meaning that even if empirical acceleration uncertainties will degrade the spacecraft state estimate (see Figure 12) the gradiometer measurements will remain unaffected. Thence, the true-to-formal error ratio for CG is expected to be close to unity.

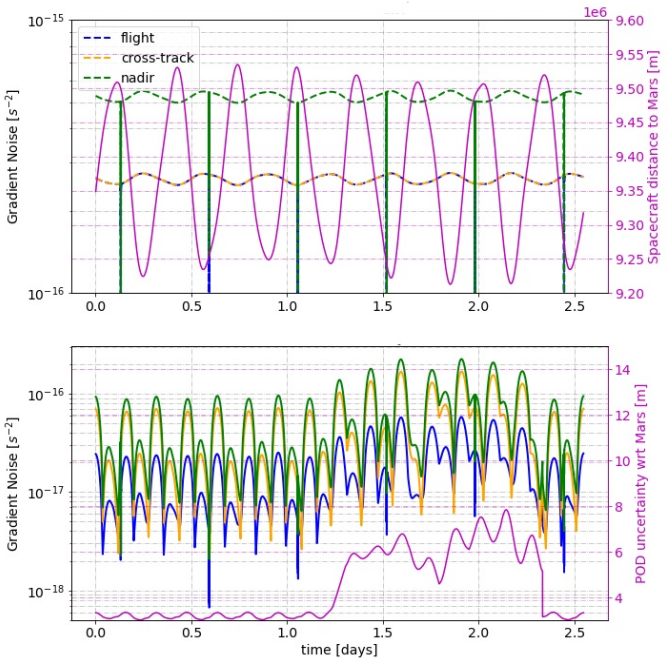

Figure A.13: Top: gradient noise from Mars gravity field uncertainty. A single orbit is representative for the entire front, since all orbits are similar in the Mars-fixed frame. Bottom: gradient noise from spacecraft state uncertainty, for the worst-case orbit. Note that the arc length is 2.2 days, and tracking ends after 1.1 days (50% capacity) hence the uncertainty is highest at this point.

Appendix B. Additional Figures

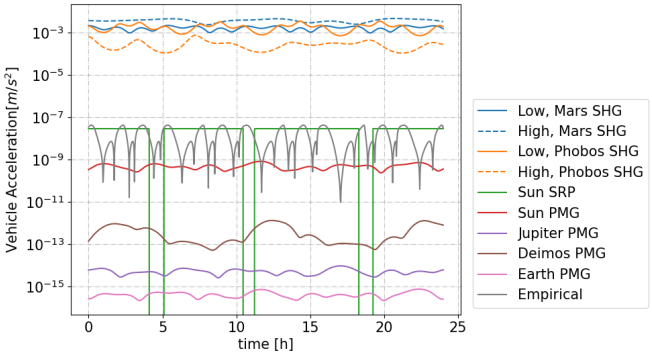

Figure B.14: Accelerations experienced by the spacecraft. Only in the very low orbits ($\bar{r} < 23$km) does Phobos' gravity prevail over Mars'. Empirical accelerations are modelled sinusoidally in radial, along- and cross-track components with an amplitude such that they can absorb errors in solar radiation pressure models (steps represent occultations by Mars). The point-mass gravity by the Earth and Jupiter can safely be omitted.

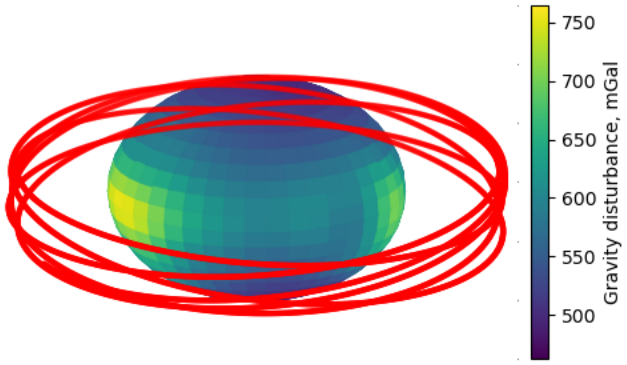

Figure B.15: Phobos' gravity anomaly w.r.t. the point mass case, attributed mainly the the degree-2 harmonics of the homogeneous spectrum (Figure 8). The disturbance acts at diametrically opposite sides of the moon, which tends to de-circularise the orbit and is therefore distinguishable in Doppler data.

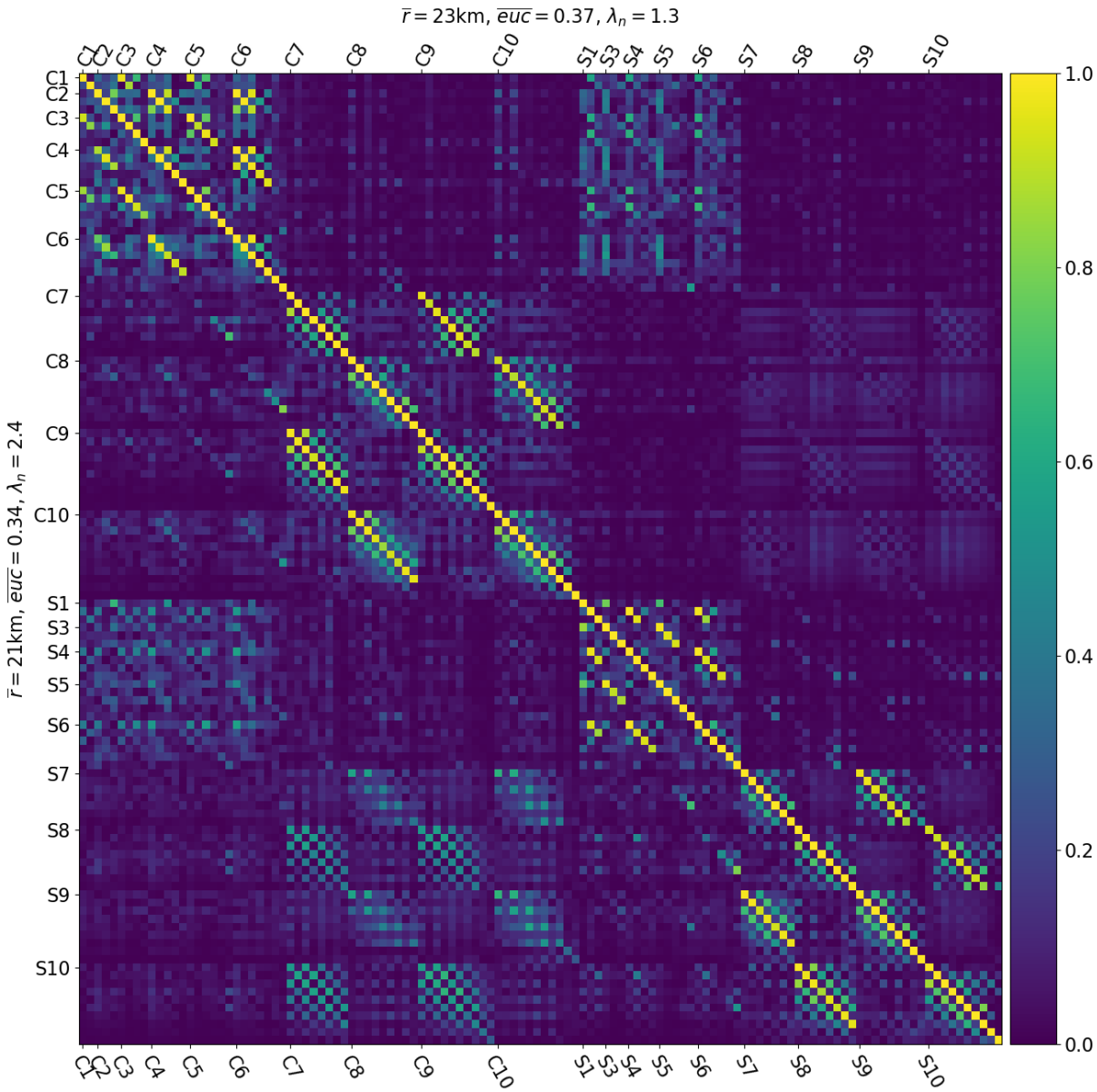

Figure B.16: Correlation matrix for spherical harmonics estimated via CG. Upper-right and lower-left triangles concern the best orbit for the RS and combined experiment, respectively. Similarly with the RS case, the cosine harmonics (2,4), (5,3) and (6,4) of the same order are highly correlated as they display a similar signal. The overall correlation for the cosine spherical harmonics is slightly worse in the higher orbit. Proximity is evidently a strong driver for minimising correlations. This behaviour true across the PF: as one lowers the altitude, the correlations generally reduce.

3

Conclusions & Recommendations

This chapter draws upon the manuscript findings to explicitly answer the research questions formulated in the introduction, and reflects on recommendations for future work.

3.1. Conclusions

The sub-questions are addressed first as to construct the framework to answer the main research question.

- **Given Phobos' challenging dynamical environment, what are the possible orbital strategies, and how do these rank in terms of maintainability?**

  Based on a homogeneous interior for Phobos, a vast selection of orbital solutions has been found. These have been categorised by three objectives to yield a more manageable subset and to favour a quantitative assessment of their behaviour. The state transition matrix eigenvalues were chosen as an a-priori indicator of stability. Since this correlates well with the position deviation induced by the injection and dynamical model errors, this choice of objective is deemed valid. Based on these errors, the manoeuvre frequency and ΔV were computed as a-posteriori indicator of maintainability, relating to the stability over a period of one week. It is found that the high and medium orbits score favourably in terms of maintainability, and the ΔV values agree with literature. A small set of high orbits are at risk of escaping the Mars-Phobos system, yet this can be mitigated by defining a smaller threshold for triggering a manoeuvre. The low orbits seem much more challenging to maintain, the reason being twofold. Firstly, due to the high variability assumed for Phobos' gravity field, which is the primary source of dynamical uncertainty. The second is attributed to the two-impulse burn strategy adopted in this work, which is extremely inefficient in terms of ΔV, thus yielding higher values than suggested in literature. Nonetheless, this orbital region is not necessarily prohibited, as an actual mission will gradually converge inwards as the gravitational potential is resolved. Consequently, the orbital front can be progressively updated, enabling an efficient planning for maintenance strategies.

- **How does the choice of orbit influence the geodesic solution obtained via RS and CG?**

  Proximity and coverage were selected as a-priori indicators for the performance of the geodesic investigation. These were found to be conflicting objectives, as closer orbits tend to be circularised in two dimensions by Phobos' irregular gravity field as influence of degree-2 harmonics grows. Distant orbits, on the other hand, behave in accordance with the elliptic three-body model, enabling excursions to higher latitudes and thus a higher coverage (see Figure 2 in the paper). Overall, proximity is found to be the main driver for the geodesic solution accuracy of both experiments; this was expected as RS benefits from the distinguishable signature of Phobos' gravity on the spacecraft trajectory, and CG relies on sampling Phobos' gravitational signal. In fact, an accurate fix on the higher gravity spectrum can only be obtained via CG flying at altitudes comparable to the moon's radius. Coverage displays a very strong correlation with the condition number of the gravity field columns in the correlation matrix for the *combined* estimation. In the RS only case, this correlation is not as visible. From this evidence, one may deduce that coverage plays a significant role in distinguishing the spherical harmonics as more terms are included in the estimation. It must be noted, however, that the favourable correlation entailed by high-coverage orbits is partly an artefact, as the estimation compensates for the reduction in

gravitational signal by relying more heavily on the a-priori regularisation. Thence, any generalisation across the orbital front is discouraged by the diversity in orbital geometry and the highly irregular gravity field. Nevertheless, this does not invalidate the choice of objectives for the present analysis; in fact, the orbits leading to the best correlations -for both experiments- lie at the vertex of the front, balancing coverage and proximity.

- **To what extent can RS alone constrain Phobos' origin?**

  The dominant influence of degree-2 harmonics acts equatorially on diametrically opposite faces of the moon, imparting a signature on the spacecraft's trajectory which is effectively distinguished due to the edge-on orbit geometry as seen from Earth. This and the small characteristic period of Phobos' gravitational spectrum contribute to the efficacy of Doppler measurements in recovering the low harmonic coefficients. As these are indicative of the deformation caused by the Stickney impact, a strong fix on their values would be sufficient in discriminating between a porous compressed or a heavily fractured interior, which have drastic ramifications on Phobos' origin. Independent estimates for libration and monolithic porosity would provide additional evidence to validate this distinction.

  Nonetheless, this science case relies heavily on the geodesic manifestations proposed by LeMaistre et al., 2019, who stress that well-mixed interiors would complicate matters significantly, since these models present a 5-10% coefficient overlap up to degree-10, whereas the best orbits for RS can resolve up to degree-6. Dmitrovskii et al., 2022 reinforce this statement by suggesting that the homogeneous, ice-rock mixture, and negative density gradient models are impossible to distinguish without access to the full harmonic spectrum. Nevertheless, if altimetry is supported by an extremely accurate orbit determination solution (10cm to 1mm), the detection of tidal deformations on the Stickney crater's rim would support the presence of a layered interior, which points towards an icy water presence (Dmitrovskii et al., 2022) .

- **What is the optimal CG instrument configuration to reinforce the geodesic solution obtained via RS?**

  Careful evaluation of noise sources affecting CAI measurements resulted in two possible arrangements: one requires extremely low atomic temperatures whereas the second operates tilt mirrors for rotation compensation. The latter significantly outperformed the former, stressing a sharp gradiometric sensitivity over a high measurement rate. Looking at the covariance formulation, two reciprocal deductions are obtained from this. First, the formal error reduction with additional observations has reached an asymptotic limit, suggesting that a longer mission timeline would not overturn the outcome of this investigation. Consequently, above reduction is linear with an increase in gradiometric sensitivity, granting additional flexibility to the design of future missions considering the use of CG: the measurement rate may be tuned with the timeline to prevent overshooting this asymptotic limit, and ensuring that an enhancement in gradiometric sensitivity contributes directly contribute towards the geodesic accuracy.

  With the addition of gradiometric measurements, most of the $10x10$ harmonic spectrum can be resolved within 0.1% accuracy (w.r.t. the homogeneous values) with a favourable correlation. Consequently, this would provide strong evidence to unambiguously constrain Phobos' origin, even for the case of a well-mixed interior. Nevertheless, technological advancements will be required to reduce the mass & power entailed by CG operation, as to strengthen its competitiveness in an instrument trade-off.

- **Based on the present study, is it possible to draw generic conclusions on the applicability of CG in other small-body missions?**

  Due to the innate complexity of interplanetary instrument trade-offs, the suitability of CG must be supported by robust numerical evidence. Still, the present study has highlighted numerous aspects which may strongly favour or discourage the inclusion of CG in future missions, such as competitiveness of radiometric tracking and the dynamics the target body.

  The accuracy of radiometric tracking is remarkable, yet its disadvantages should be kept in mind, the first being the high cost associated with operations. Secondly, for utmost accuracies, dual-frequency antennas are required onboard the spacecraft. Finally, uniform coverage cannot be guaranteed if occultation periods are frequent, as is the case for the Moon. Depending on the specific mission case, one may leverage on these drawbacks to opt for the direct measurements offered by CG.

  The dynamical environment considered here shows parallels to that of other small moons, albeit Phobos' is the harshest of them all (as derived by Scheeres, 2012). A compelling case could be made for the

icy moons, which have attracted much scientific interest (Cable et al., 2021; Grasset et al., 2013). These enable more leeway in the orbital design, facilitating a higher polar coverage, which might give CG the edge in estimating the higher portions of the harmonic spectrum. Moreover, additional sources of systematic uncertainties may confound the RS method, as for instance atmospheric drag on Ganymede or plume drag on Enceladus. But by far the most fundamental aspect relates to the geospatial distribution of the harmonic powers, as these could impart indistinguishable signatures on the spacecraft trajectory. For icy moons, isostatic compensation along with viscous relaxation weaken the influence of degree-2 harmonics (Hemingway et al., 2018). This aspect must be confronted with the orbital geometries to (dis)favour the competitiveness of RS as opposed to CG. Certainly, to contemplate the inclusion of the latter, strong grounds for an in-depth geodesic investigation must be present. Perhaps the science return of JUICE (Grasset et al., 2013) will encourage this as studies will attempt to relate the fascinating visible phenomena to the deep interior.

Leveraging on the advantages entailed by small-body environments for Gradiometers based on Cold Atom Interferometry, to what extent can these instruments strengthen the Radio Science geodesic experiment to constrain Phobos origin?

Whilst it is true that small bodies present a favourable scaling for the inclusion of CG, their challenging dynamical environments limit the choice of orbital strategies. Thence, maintenance requirements should be carefully evaluated against the science return of the geodesic experiments. In Phobos' case the observational geometry and characteristic period of its gravity signal designate radio science as highly competitive for constraining the low end of Phobos' gravity spectrum. In case of a prevalent density anomaly below the Stickney crater, this may provide sufficient evidence to pinpoint Phobos' origin. Yet, in the case of a rubble pile or icy moon interior (or a combination thereof), one must recover the higher ends of the spectrum before concluding on the former. This is only possible via direct measurements provided by gradiometry, which can recover the $10x10$ gravity field with accuracies below 0.1% w.r.t. the homogeneous interior values. Nevertheless, technological advancements will be required to alleviate the logistical challenges associated with Cold Atom Interferometry for spaceborne gradiometry.

3.2. Recommendations for future work

Due to time constraints and limitations associated with the numerical methods employed in this work, several points have been identified as deserving further investigation. These are briefly summarised hereby in decreasing order of importance.

- This work is primarily concerned with the contribution of gradiometry, hence the geodesic discussion focused on the conclusions drawn from spherical harmonics. Nonetheless, librational information would corroborate the conclusions drawn from degree-2 and lead to an improved Phobos ephemeris. A control-point analysis goes beyond the possibilities of conceptual mission design. Nevertheless, the dynamical model and RS estimation could be expanded to include libration estimates from a given set of landmarks, or from its signature on the spacecraft trajectory. The spacecraft initial state(s) w.r.t. Phobos could be estimated to the dm-level for the majority of the low orbits. This suggests exploring altimetry crossovers on the Stickney crater rim for determining tidal deformations, thus obtaining a formal error of Phobos' k_2 as means of probings its interior rigidity (Dmitrovskii et al., 2022).

- High-fidelity simulations will be needed to ensure that the proposed orbits can cope with operational constraints and the high uncertainties tied to Phobos' gravity field. Regarding the latter, an efficient manoeuvre algorithm could be implemented to yield a realistic ΔV budget, such as a time-varying controller (Baresi et al., 2020). This would support the promotion of particular orbits as opposed to others. Most importantly, this would provide constraints on the overall mission duration; consequently, the CG instrument design could be reviewed to maximise its the geodetic solution accuracy.

- The solar radiation pressure has been identified as the main driver of systematic uncertainties for parameter estimation. Since the spacecraft characteristics are unknown a simple cannonball model was implemented. Future work may wish to consider rotational dynamics for a reference wing-box structure, as this would justify the upgrade to a panelled radiation model. Consequently, this would enable a reformulation of the empirical accelerations as to better evaluate their confounding influence on the RS experiment.

A

Integrator & Propagator Selection

One must resort to numerical integration methods for determining the orbit of the spacecraft, since no closed-form analytical solutions exist that can incorporate all the perturbing forces. The following integrators are available on *tudat*: Euler, Runge-Kutta (RK), Runge-Kutta-Fehlberg (RKF), Dormand-Prince (DP), Adams-Bashforth-Moulton (ABM), and Bulirsch-Stoer (BS). Each integrator presents an inherent accuracy, computational complexity and numerical stability, hence one must reflect on the conceptual nature of the problem to balance these characteristics judiciously. Euler and BS are preliminarily discarded, as the former is unfit to simulate complex dynamics and the latter is better suited for longer propagations with sparse outputs (Dirkx and Cowan, 2020). The following integrators are considered viable candidates:

- RK with fixed step sizes [50,75,100,150,200,300]s
- RFK 4(5) & RKF 5(6) & RFK 6(7) & RFK 7(8) with absolute and relative tolerances [10^{-16},10^{-14},10^{-12}, 10^{-10},10^{-8},10^{-6}]
- DP8(7) with absolute and relative tolerances [10^{-16},10^{-14},10^{-12}, 10^{-10},10^{-8},10^{-6}]
- ABM variable order, variable step size with with absolute and relative tolerances [10^{-12},10^{-10},10^{-8}, 10^{-6},10^{-4},10^{-2}]
- ABM order 6 & ABM order 8 & ABM order 10 variable step size with with absolute and relative tolerances [10^{-12},10^{-10},10^{-8},10^{-6},10^{-4},10^{-2}]
- ABM with variable order, fixed step sizes [50,75,100,150,200,300]s

A.1. Requirement Definition

Due to highly perturbed dynamical environment, a small deviation on the nominal state of a few m can quickly exacerbate, leading to an entirely different trajectory. In light of the spacecraft's close proximity to Phobos (the orbital altitude is comparable to the radius) this deviation would offthrow the geodesic estimation, which is undesired. At the same time, a mm-level accuracy on the trajectory would be pointless, as it would be overshadowed by the high uncertainties associated with Phobos' gravity field. Furthermore, in searching for optimal trajectories a relatively large design space is scanned, meaning the computational time should be kept to a minimum. This suggests the use of variable step-size integrators, which extend the step size in regions with less dynamical variations to reduce the computational effort. Nonetheless, Mars being the dominant attractor, the orbit is reasonably circular and Keplerian, with third-body perturbations from Phobos. Thence, one should not expect a considerable improvement in computational efficiency from variable-step integrators. Moreover, manoeuvres have to be performed with a certain frequency, making long time steps undesirable in guaranteeing a fair comparison across many orbits. A preliminary analysis was conducted for setting up an upper bound on the integration error. A coarse grid search yielded a set of initial conditions leading to trajectories that neither crash nor escape for a week. The diversity of these orbits is representative of the optimal front used throughout this work (section 3.2 of the paper) as to guarantee the validity of this experiment. Given that the spacecraft dynamics are mostly linear, the state transition matrix

Φ provides a reliable means of propagating the effect of uncertainties on the initial state. It was found that an initial error of $1cm$ does not grow beyond $1m$ after one week of propagation. This is well below the dynamical modelling uncertainty and within the postfit orbit determination accuracy, whilst being computationally inexpensive. Hence, a $1cm$ accuracy requirement for the integrators was selected.

A.2. Benchmark Selection

To analyse the behaviour of a set of integrators, a benchmark solution must be generated. This must reflect the 'truth model' to a high degree of confidence, meaning it will involve very strict integration tolerances. The defining characteristic of a benchmark solution is the minimisation of the overall integration error, composed of the *truncation error*, which reflects the inherent mathematical limitation of the integrator, and the *numerical (round-off) error*, which arises from the limited precision of floating-point arithmetic (Dirkx and Cowan, 2020). Given that the former behaves in a predictable manner whilst the latter is erratic in nature, one may tune the integration step via Richardson extrapolation to find the regime which minimises the combined influence of both. A RK integrator is the most reasonable choice for a benchmark integrator as it enables tuning the time step in a predictable manner as to meet the above requirement.

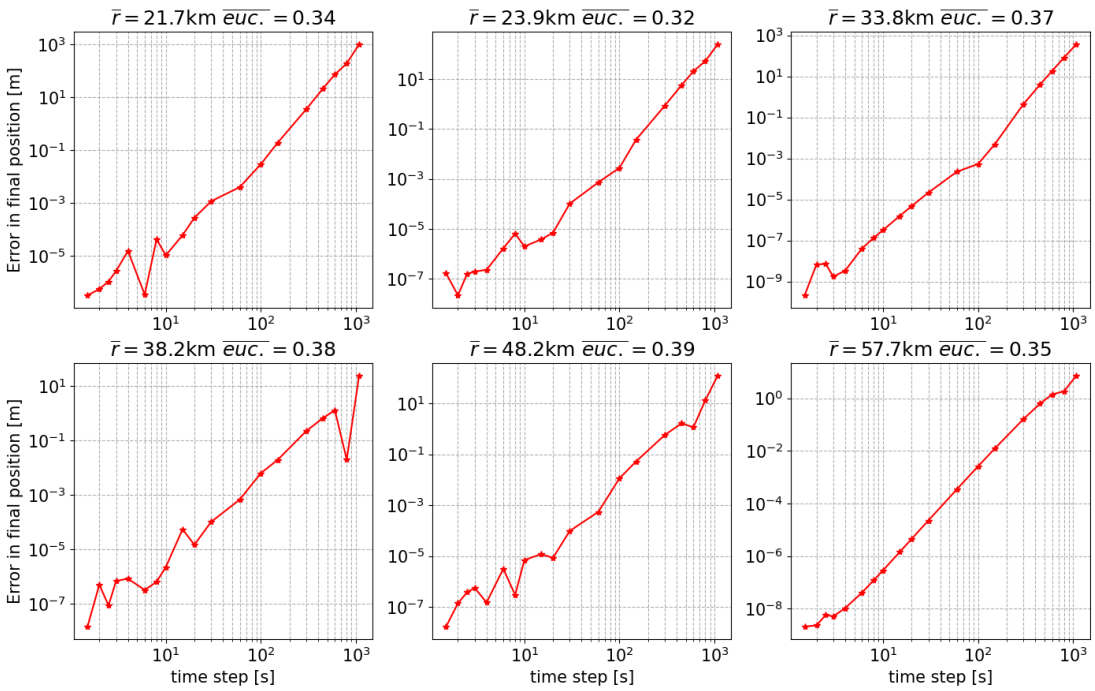

Figure A.1: Richardson extrapolation to select the benchmark solution time step

Figure A.1 compares the error obtained for various time steps with the one obtained for $h = 1s$. This has been performed across six orbits sampled uniformly from the coarse grid search mentioned above. It is seen that $h = 10s$ lies in at the bottom of the linear integration error regime, without incurring round-off errors. Three additional strategies have been performed to validate this selection. Starting from t_0, the orbits have been propagated forwards for 1 week. Then, the final state has been propagated backwards until t_0. The difference in position at each intermediate epoch is reported in Figure A.2 (blue). Secondly, a RE scheme with a smaller time step of $9s$ was performed (cyan), as well as a run using an Encke propagator (magenta). In all cases, the integration error which never surpasses $0.01cm$, hence the benchmark solution is deemed validated.

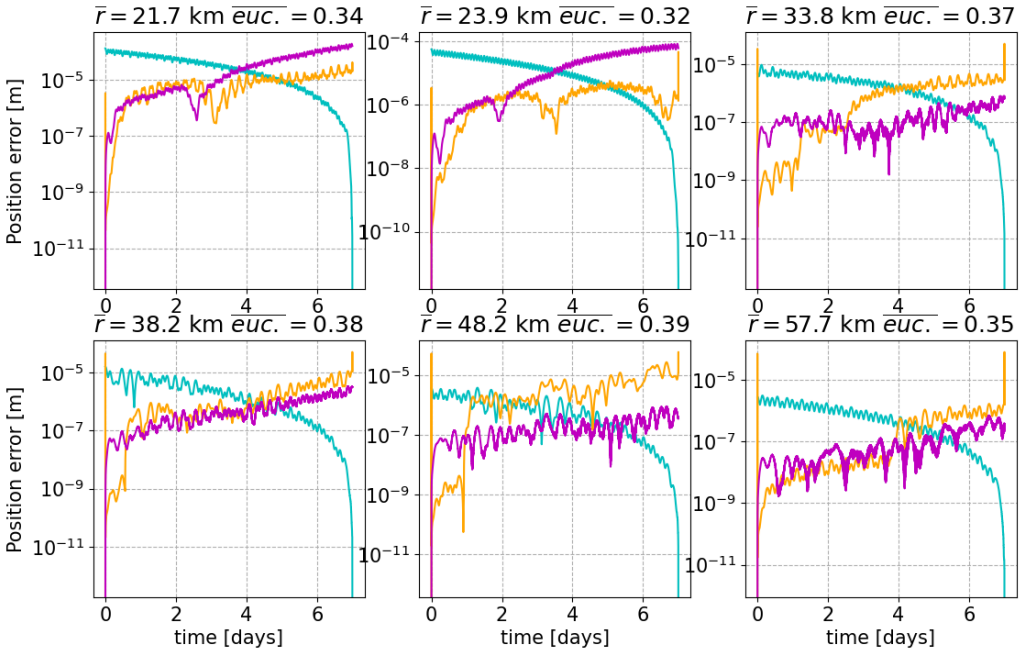

Figure A.2: Benchmark validation: forward and backward propagation difference in state (cyan), slightly smaller time step (orange) and Encke propagator (magenta)

A.3. Integrator Selection

The performance of each integrator is driven by the solution accuracy w.r.t. the benchmark and the computational effort, as shown in Figure A.3. DP8(7) and RFK7(8) perform poorly, as these are best suited for orbits with high eccentricities (Dirkx and Cowan, 2020) and for highly varying dynamics in general, as for instance during re-entry studies with distinct orbital and atmospheric phases. The variable-step ABM display unpredictable trend lines, driven by their tendency to get "stuck" at very small timesteps (Dirkx and Cowan, 2020). The RK4 performs well regardless of the orbit, but not as efficiently as the variable-order fixed-step ABM. This was to be expected, as ABM is suited for low-to-moderate eccentricities (Dirkx and Cowan, 2020), and a fixed time step is adequate when the dynamics show little variation over time, as is the case here. Thence, this integrator with a time step of $75s$ is selected for propagating the spacecraft dynamics, as it guarantees an error below the $cm-$level. It is also mentioned that a similar -albeit slightly more limited- investigation was performed for Phobos, which had to be propagated for 1 year to assess the evolution of the formal error (journal section 6.5). A time step of $400s$ was sufficient to keep the integration error below $100m$, which represents the 1-σ formal error on its latest ephemeris (Fayolle et al., 2021).

A.4. Propagator Selection

One may also leverage on the physicality of the problem to formulate the equations of motion in different ways, as this may facilitate their propagation and curtail numerical errors. All the propagators offered in *tudat* are considered for the problem: Cowell (Cartesian states, default setting), Encke, Gauss Modified Equinoctial Elements (GMEE), Unified State Model -Quaternions (USM-Q), Unified State Model -Modified Rodrigues Parameters (USM-MRP) and Unified State Model- Exponential Map (USM-EM).

Given that the initial conditions display an inclination of 0° as expressed in the Body-Fixed Frame (BFF) (see Figure 4 of the journal), this leads to singularities in the USM and MEE, leading to excessively long computational times. Only Cowell and Encke performed admissibly. The Encke formulation exploits the Keplerian element stability, which is why it outperforms Cowell in orbits that are further from Phobos. Nonetheless, this advantage is very small, hence Cowell was retained as it was preferred to prioritise an accurate propagation of the close, highly perturbed orbits.

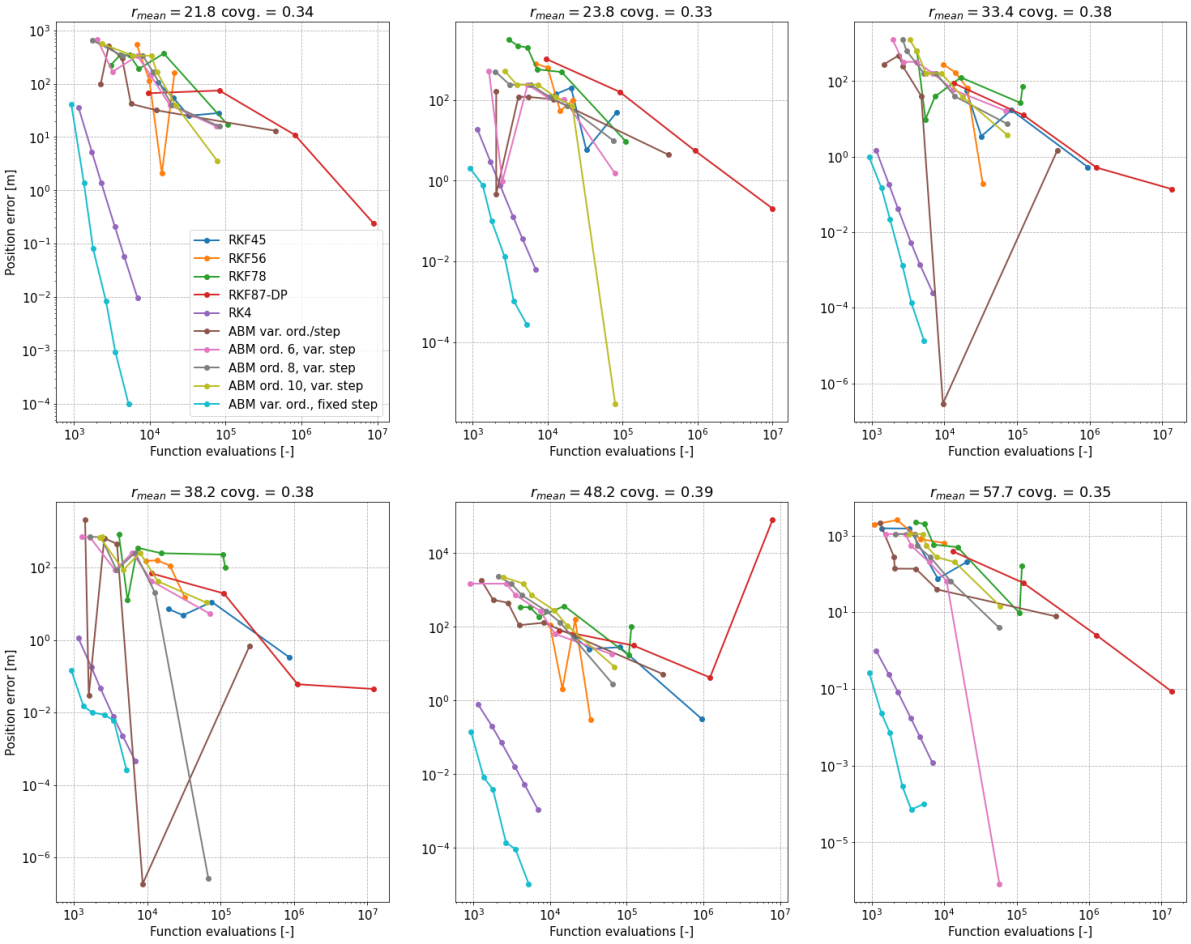

Figure A.3: Integrator performance comparison: final position error w.r.t. benchmark solution and total number of function evaluations, one-week propagation

B

Validation Strategy

This chapter outlines the steps taken to validate the numerical methodology adopted in this work. The simulations have relied on the interlinking of the *tudat* software developed at the Astrodynamics & Space Missions department of Delft University of Technology, [1] and the code for processing the GOCE gravity gradiometry measurements according to the *time-wise* approach (Siemes, 2008). *Tudat* was used for orbit propagation and to conduct the RS experiment. This software features verification tests upon installation, and has been used extensively for publications (Dirkx et al., 2018; Dirkx et al., 2014) and MSc theses. Thence, validating the software itself is deemed unnecessary. However, to ensure that the dynamical models employed in this work are implemented correctly, the Phobos and spacecraft orbits are validated in section B.1 and section B.2, respectively. The observation models and parameter estimation for the RS experiment is validated in section B.3. The gradiometry code is also deemed highly reliable, as it has lead to present state-of-the-art gravity field models for Earth, yet its implementation is validated in section B.4.

B.1. Validating Phobos' Orbit

The Keplerian motion drawn by Phobos around Mars exhibits variations primarily attributed to the Mars aspherical gravity field and the Sun, which are captured in the ephemeris of Lainey et al., 2021. To enhance the fidelity of the parameter estimation, Phobos' state has been numerically propagated in *tudat* with accelerations as listed in section 3.2 of the paper.

The agreement between the propagated Phobos and that retrieved by spice kernels is investigated in Figure B.1 in spherical coordinates w.r.t. Mars. After one week of propagation, the difference in absolute position is of 300m which is tolerable considering the scale of the semi-major axis (9378km). This discrepancy stems primarily from the fact that Lainey et al., 2021 model the forced libration in Phobos' orbit which we do not, causing a secular drift in Phobos' along track component ($\hat{\boldsymbol{t}}$ term in equation 4 in the manuscript) reflected by the drift in longitude. The difference in radial component ($\hat{\boldsymbol{r}}$) displays a periodicity as well as a small drift (note that due to the orbital eccentricity the radius does not reflect absolute position).

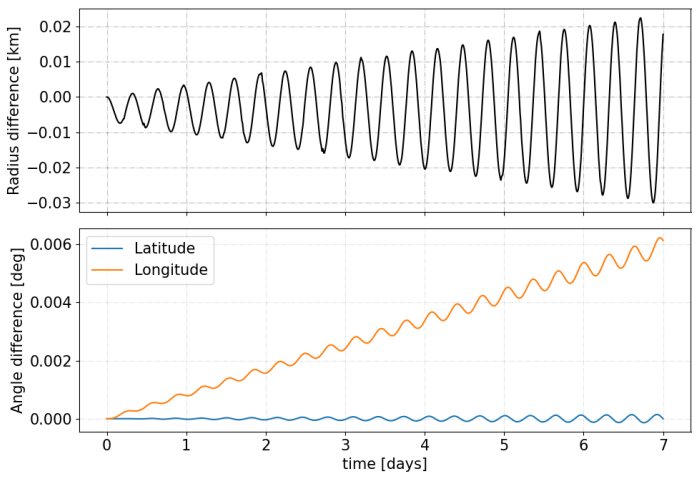

Figure B.1: Phobos Lainey et al., 2021 ephemeris vs *tudat* propagation

[1] Documentation and user guide can be found at: https://tudat-space.readthedocs.io/en/latest/

B.2. Validating the Orbital Front

Various studies (Baresi et al., 2020; Chen et al., 2020; Pushparaj et al., 2021) have tackled the problem of finding suitable QSOs for the exploration of Phobos. As mentioned in section 3.3 of the paper, these rely on assumptions which are incompatible with our experiment. Nonetheless, these provide guidance in setting up the numerical orbit search and validating the orbital characteristics.

The numerical search grid was set up in accordance with suggestions provided in literature. Firstly, the sought initial condition for x_0 (in Phobos' BFRF, see Figure 4 in the paper) were set to negative values, which produces retrograde orbits (against the direction of Phobos' orbit). These are beneficial insofar as the destabilising effect of $C_{2,2}$ is averaged out in space due to the large relative angular motion between the spacecraft and Phobos (Scheeres, 2012). Secondly, the search space was bounded according to the expected behaviour of the orbits. Far from Phobos, the spacecraft trajectory resembles an elliptical orbit as described by the Hill equations. Here the effect of Phobos' eccentricity is more pronounced, which induces out-of-plane deviations. To maintain (pseudo) stability their orbital period must be resonant with the period of Phobos around Mars (Scheeres et al., 2019). As orbits move closer to Phobos its aspherical gravity takes effect, circularising the orbits in one plane.

The above strategy yielded a number of Pareto-optimal solutions in the multidimensional objective space as defined in Section 3.3 of the manuscript. Six orbits were selected for validation purposes: their defining characteristics were compared to those obtained by Chen et al., 2020 for near-identical starting conditions. The sets of values are reported in Table B.1, and orbit 4 is also plotted in Figure B.2 and B.3 for visualisation purposes. The orbital selection is deemed validated as the values display a good agreement, aside from the stability index which is consistently higher in *tudat*. This stems from the fact that our dynamical model includes the Sun, Deimos & Earth and Phobos' degree-10 gravity field at a specific epoch, whereas Chen et al., 2020 use a time-invariant formulation and truncate Phobos' gravity at degree-2. Even so, it will be shown in Appendix C that most of the orbits generated here can easily be maintained in the full dynamic model.

Orbit Number	Amplitude [km]	Resonance ratio	Period [days]	Stability index
1	21.8 x 30.7 x 0.1	7:9	1.66	1.02
	21.5 x 30.4 x 0.1	7:9	1.65	6.77
2	24.7 x 36.8 x 0.1	4:5	1.03	1.19
	24.5 x 37.1 x 0.1	4:5	1.04	2.77
3	30 x 53 x 18	6:7	1.74	1.06
	31 x 54 x 18	6:7	1.76	1.98
4	32.9 x 56 x 26.8	13:15	3.89	1.05
	32.5 x 55 x 26.6	13:14	3.86	1.66
5	25.6 x 46.5 x 21.3	5:6	1.44	1.18
	25 x 46.1 x 21.8	5:6	1.43	2.19
6	28 x 53.4 x 25.2	6:7	1.78	1.09
	27.6x x53 x 25.2	6:7	1.77	1.13

Table B.1: Characteristics for 6 orbits used for validation. In each cell, top values are for Chen et al., 2020 and bottom are for *tudat*.

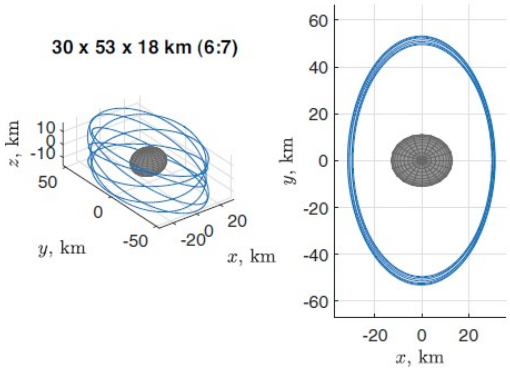

Figure B.2: 3D image of orbit 4 (Chen et al., 2020

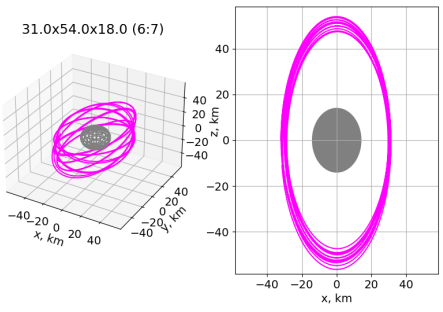

Figure B.3: 3D image of orbit 4 in *tudat*

B.3. Validating the Radio Science Experiment

Radio science experiments were performed for small-body missions to Eros (Miller et al., 2002), Vesta (Konopliv et al., 2014), Ceres (Konopliv et al., 2018) and Bennu (McMahon et al., 2018). The latter was selected to validate the present implementation as it is deemed the most manageable in terms of computational time (9 days) and includes a consider covariance analysis. The main differences between Bennu and Phobos relate to the small size of the former ($R = 262.5m$) as well as the absence of a dominating primary body.

The DE424 spice kernel forms the basis for Bennu's ephemeris and rotation model. A homogeneous interior for Bennu is assumed to model the gravity field, and introduced as a-priori regularisation (1-σ uncertainty derived from shape). The accelerations consist of Bennu's spherical gravity up to degree-8 and the Sun's point-mass gravity and (cannonball) radiation pressure. The gravity field degrees 6 to 8 were included as consider parameters, whereby the Kaula rule is used to model their uncertainty. The tracking data consists of continuous Doppler measurements every $60s$ and optical images with an interval of $10m$ for the first and last tracking day. The spacecraft's near-circular polar orbit $1km$ from Bennu's CoM was validated in Figure B.4 and B.5.

The estimated parameters are the gravity field up to and including degree 5, the spin pole orientation and rotation rate (from 100 landmark positions). To accurately reconstruct Bennu's orbit the Yarkovski effect must be modelled, hence this was not estimated here. The formal errors as obtained by both independent simulations are reported in Table B.2. The set of values for the gravity field terms are consistent to within a factor 5, which is deemed satisfactory to validate this work. This discrepancy is attributed to slight differences in the radiometric tracking arrangement (ground stations unspecified in McMahon et al., 2018) and *tudat's* omittance of Bennu's ephemeris estimation. The rotation parameters are of a higher quality in McMahon et al., 2018, possibly due to more favourable landmark visibility conditions and an advanced landmark processing algorithm.

Parameter	**McMahon et al., 2018**		**This work**	
	Regular	With Consider	Regular	Consider
$RMS(\sigma_{C\&S1})$	2.767e-4	2.773e-4	2.24e-4	2.26e-4
$RMS(\sigma_{C\&S2})$	1.582e-3	1.582e-4	4.78e-4	4.85e-4
$RMS(\sigma_{C\&S3})$	4.575e-3	4.578e-3	1.08e-3	1.10e-3
$RMS(\sigma_{C\&S4})$	4.23e-3	4.23e-3	9.97e-4	9.85e-4e-3
$RMS(\sigma_{C\&S5})$	4.28e-3	4.29e-3	9.01e-4	9.12e-4
Spin Pole [°]	0.14	-	0.025	-
Ω [°/day]	6e-10	-	3.06e-8	-

Table B.2: Formal errors comparison (McMahon et al., 2018 and *tudat*) via regular and consider covariance analysis

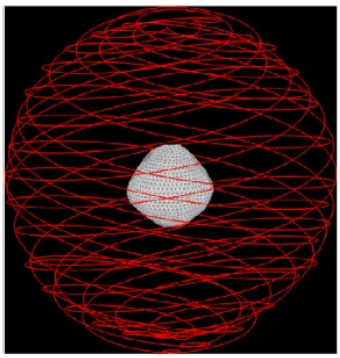

Figure B.4: 3D orbit around Bennu (McMahon et al., 2018

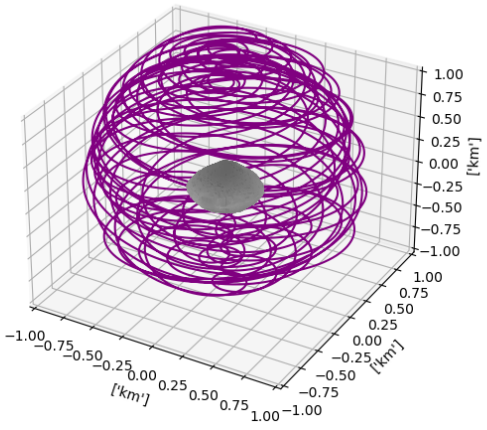

Figure B.5: 3D orbit around Bennu (*tudat*)

B.4. Validating the Gradiometry Experiment

The implementation of the code for processing gravity gradients was validated using the gravity field solution EGM GOC 2, obtained by Pail et al., 2010 from GOCE. The orbit spans from November to the end of December 2009, a 61-day period that is sufficient to ensure full coverage of the Earth. The primary methodological difference w.r.t. the Phobos case, aside from the different physical scaling of the target bodies, lies in the fact that the Earth is the dominant attractor, whereas Phobos is not. Hence, in the journal paper, the rotation $\boldsymbol{R} : GRF \rightarrow IRF$ occurs via Mars. This additional step has been validated separately by inspecting the GRF axis misalignment w.r.t. Phobos' CoM.

The time-wise processing approach was used to compute the preconditioner for conjugate gradients (W., 2018) up to degree/order 224. As opposed to computing the full Jacobian matrix, this method enables a more computationally-efficient processing scheme and a GOCE-only solution, meaning no a-priori gravity field information is needed to regularise the problem. Only the trace components V_{xx}, V_{yy}, V_{zz} were used to derive the solution, with the gradient noise set to 10, 10 and 20 $mE\sqrt{Hz}$, respectively, valid for a measurement rate of 10s (Rummel et al., 2010). The spherical harmonic formal errors (root-mean-square) as obtained from EGM GOC 2 and the present work are shown in Figure B.6.

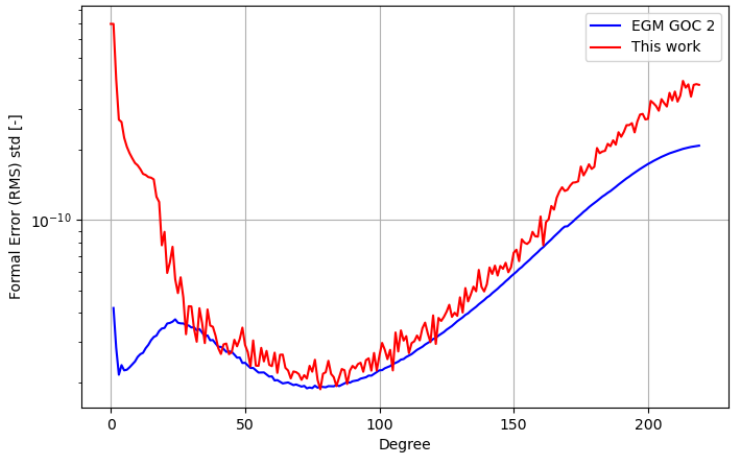

Figure B.6: Spherical harmonic formal errors (root-mean-square) for 2-month GOCE solution. Pail et al., 2010 vs this work.

A significant portion of the curves display a similar behaviour and overall magnitude. Nonetheless, a larger error is obtained here w.r.t. EGM GOC 2 at degrees below 50 and above 170. The former is mainly due to the polar gap, which leads to a poorer accuracy in the affected zonal and near-zonal coefficients. Pail et al., 2010 mitigate this aspect by introducing an independent GOCE kinematic orbit solution (from GPS measurements) complete to degree/order 50, which we do not. Since the GOCE dataset cannot estimate the full spectrum, high noise is present on the coefficients larger than 170. Pail et al., 2010 introduce Kaula regularisation for degrees 170-224, forcing the signal (and noise) to zero, whereas we do not. The remaining discrepancy is related to the orbit deviation. To reduce the computational complexity of the propagation, no drag (compensation) nor third-body perturbations were implemented here. Thence, the present orbit shows a linear drift w.r.t. the actual GOCE orbit which grows to $50km$ after 61-days. In light of the above considerations, the behaviour of the solution obtained in this work is deemed satisfactory, meaning the validation strategy is successful.

C

Orbit Sensitivity Analysis and Maintenance

The high uncertainties associated with Phobos' dynamical environment were propagated in order to assess the resulting variation on the nominal orbits. This served as a guideline to set up the parameter estimation, and to compare the maintenance costs across the Pareto front, which are subsequently validated with Baresi et al., 2020; Chen et al., 2020; Pushparaj et al., 2021.

The manoeuvre frequency and duration condition the orbit maintenance ΔV budget, as well as the length of the tracking data arcs in the RS experiment (Section 5.4 of the paper). To this end, one must consider the deviation of the actual trajectory from the nominal trajectory, which is caused by two sources of uncertainty. *Injection errors* on the spacecraft state when targeting the nominal orbit are estimated by the MMX design team as $50m$ and $3cm/s$ (Baresi et al., 2020). These derive from the uncertainty in Phobos' ephemeris[1] and the execution error in thrusting direction. *Dynamical model errors* arise due to the poorly-constrained Phobos gravity field: the maximum standard deviation of all heterogeneous interiors (LeMaistre et al., 2019) is hereby considered. These errors were propagated via the state transition and sensitivity matrices, to compute the state deviation across the Pareto front in a consistent manner, for a total of 48 hours. Assuming a two-impulse correction manoeuvre, the influence of different manoeuvre frequencies and durations was assessed in Figure C.1. Values of 24h and 2h were selected as compromise between the orbit determination accuracy and the ΔV budget required for maintenance.

Finally, for the mission duration of one week, the expected number of manoeuvres, the total ΔV and the risk of an orbit crashing or escaping the system is computed. For each orbit in the Pareto front, 50 random samples are drawn from the set of heterogeneous interiors and injection errors. Every 24h, a two-impulse correction manoeuvre lasting 2h is performed if the orbit displays a deviation larger than a certain threshold. The latter scales with the (average) orbital altitude, and is left as a free parameter in Figure C.2. Results indicate that the high orbits are relatively inexpensive to maintain: the values (ΔV = 1-5m/s per week) are slightly higher than literature ($\Delta V \approx 1m/s$) as the latter assume a time-invariant system with a homogeneous gravity field (Baresi et al., 2020; Pushparaj et al., 2021) or a dynamical model error limited to 10% on $C_{20}, C_{2,2}$ (Chen et al., 2020). The very high orbit incur a significant risk of escaping the system, hence a stringent manoeuvre threshold should be adopted. The low orbits are very costly to maintain, although the ΔV values presented here are overly conservative, since a non-optimised two-impulse manoeuvre is performed. Literature values are not comparable due to the assumptions mentioned above, and the fact that here, the full 10x10 spectrum of Phobos' gravity is varied which induces strong deviations for low orbits. It is important to stress that in a real mission, the spacecraft will first inject into high orbits, and then gradually converge inward as spherical harmonics are estimated. This way, transfer and station keeping manoeuvres can be planned effectively, curtailing the associated ΔV costs.

[1] At the present time, the formal error on Phobos' state is about $100m$ (Lainey et al., 2021). Injection errors by MMX implicitly assume that this can be reduced in the approach phase via targeting strategies.

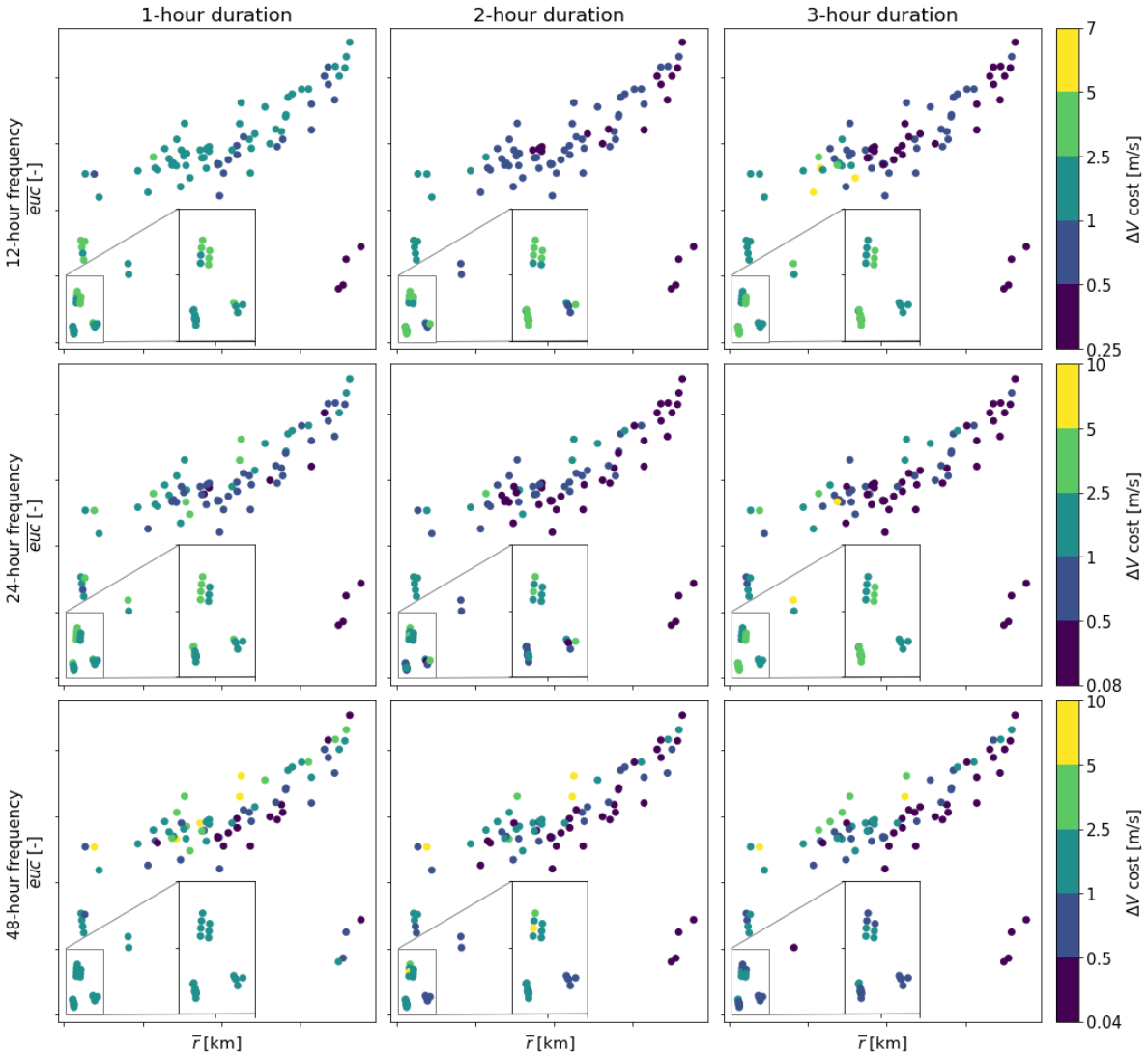

Figure C.1: Influence of arc length selection on total ΔV budget for two-day stationkeeping via two-impulse manoeuvres

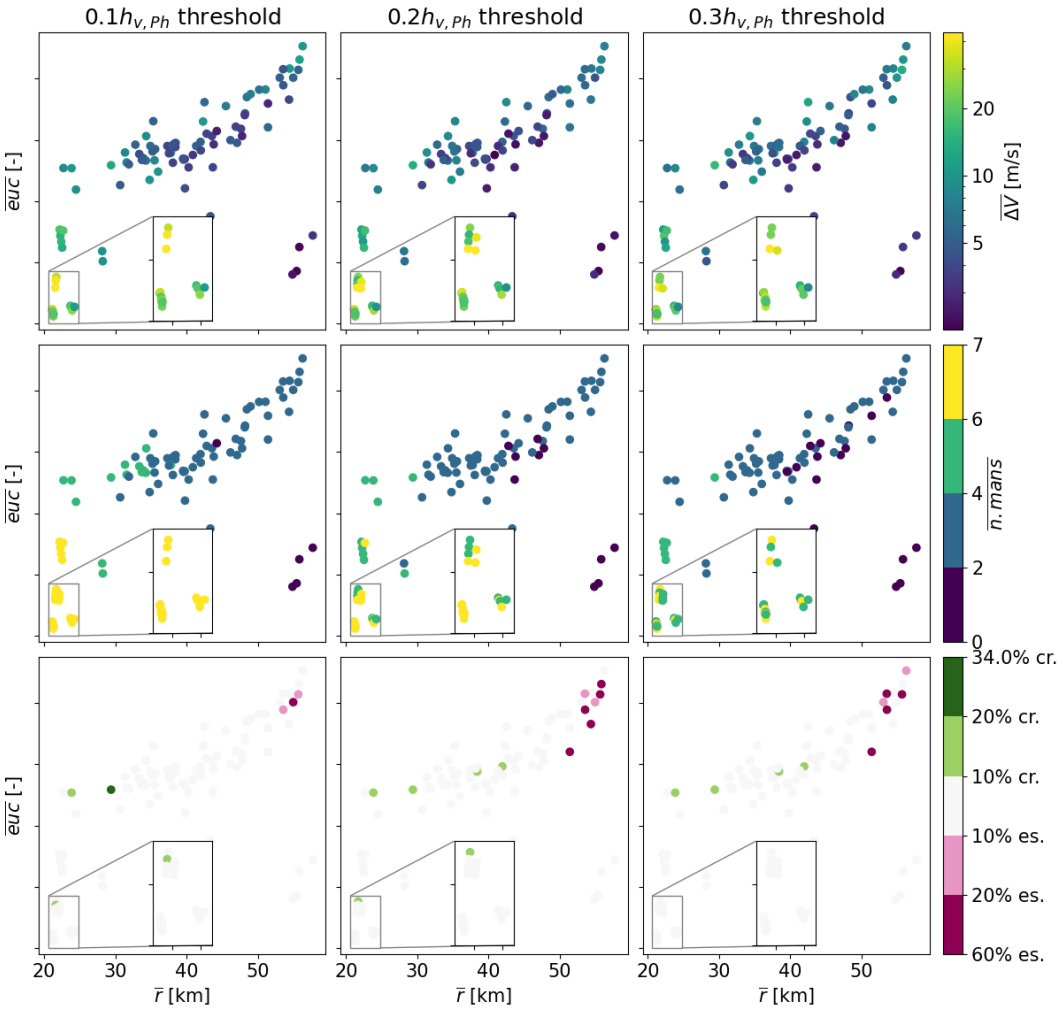

Figure C.2: Influence of altitude threshold trigger on manoeuvre frequency, total ΔV budget and risk of crash/escape. One week mission duration, two-impulse manoeuvres. Cr. = crash, es. = escape.

Bibliography

Bagheri, A. et al. (2021). Dynamical evidence for Phobos and Deimos as remnants of a disrupted common progenitor. *Nature Astronomy*. https://doi.org/10.1038/s41550-021-01306-2

Baresi, N., Dei Tos, D. A., Ikeda, H., & Kawakatsu, Y. (2020). Trajectory design and maintenance of the Martian moons exploration mission around Phobos. *Journal of Guidance, Control, and Dynamics*, *0*(0), 1–12. https://doi.org/10.2514/1.G005041

Barrett, B. et al. (2014). Mobile and remote inertial sensing with atom interferometers. *Proceedings of the International School of Physics "Enrico Fermi", 188 "Atom Interferometry"*, 493. https://doi.org/10.3254/978-1-61499-448-0-493

Bongs, K. et al. (2019). Taking atom interferometric quantum sensors from the laboratory to real-world applications. *Nature Reviews Physics*, *1*. https://doi.org/10.1038/s42254-019-0117-4

Cable, M. et al. (2021). The science case for a return to Enceladus. *Planetary Science Journal*, *2*(4). https://doi.org/10.3847/PSJ/abfb7a

Campagnola, S. et al. (2018). Mission analysis for the Martian moons explorer (MMX) mission. *Acta Astronautica*, *146*, 409–417. https://doi.org/https://doi.org/10.1016/j.actaastro.2018.03.024

Canup, R., & Salmon, J. (2018). Origin of Phobos and Deimos by the impact of a Vesta-to-Ceres sized body with Mars. *Science Advances*, *4*(4). https://doi.org/10.1126/sciadv.aar6887

Carraz, O., Siemes, C., Massotti, L., Haagmans, R., & Silvestrin, P. (2014). A spaceborne gravity gradiometer concept based on cold atom interferometers for measuring Earth's gravity field. *Microgravity Science and Technology*, *26*. https://doi.org/10.1007/s12217-014-9385-x

Chen, H., Canalias, E., Hestroffer, D., & Hou, X. (2020). Effective stability of quasi-satellite orbits in the spatial problem for Phobos exploration. *Journal of Guidance, Control, and Dynamics*, *43*(12), 2309–2320. https://doi.org/10.2514/1.G004911

Dirkx, D. et al. (2018). Laser and radio tracking for planetary science missions: A comparison. *Journal of Geodesy*, *93*(11), 2405–2420. https://doi.org/10.1007/s00190-018-1171-x

Dirkx, D., Vermeersen, L., Noomen, R., & Visser, P. (2014). Phobos laser ranging: Numerical geodesy experiments for Martian system science. *Planetary and Space Science*, *99*, 84–102. https://doi.org/https://doi.org/10.1016/j.pss.2014.03.022

Dirkx, D., & Cowan, K. (2020). *Numerical astrodynamics lecture notes: Integrator selection*.

Dmitrovskii, A. A., Khan, A., Boehm, C., Bagheri, A., & van Driel, M. (2022). Constraints on the interior structure of Phobos from tidal deformation modeling. *Icarus*, *372*, 114714. https://doi.org/https://doi.org/10.1016/j.icarus.2021.114714

Douch, K., Wu, H., Schubert, C., Müller, J., & Pereira dos Santos, F. (2018). Simulation-based evaluation of a cold atom interferometry gradiometer concept for gravity field recovery. *Advances in Space Research*, *61*(5), 1307–1323. https://doi.org/https://doi.org/10.1016/j.asr.2017.12.005

Fayolle, M., Dirkx, D., Lainey, V., Gurvits, L., & Visser, P. (2021). Coupled and decoupled strategies for spacecraft's and natural bodies' state estimation - application to the JUICE mission. *EPSC Abstracts*. https://doi.org/https://doi.org/10.5194/epsc2021-364

Grasset, O., Dougherty, M., Coustenis, A., Bunce, E., Erd, C., et al. (2013). Jupiter icy moons explorer (JUICE): An esa mission to orbit ganymede and to characterise the jupiter system. *Planetary and Space Science*, *78*, 1–21. https://doi.org/10.1016/j.pss.2012.12.002

Guo, X. et al. (2021). A lighter core for Phobos? *Astronomy and Astrophysics*, *651*. https://doi.org/10.1051/0004-6361/202038844

Haagmans, R., Siemes, C., Massotti, L., Carraz, O., & Silvestrin, P. (2020). ESAs next-generation gravity mission concepts. *Scienze Fisiche e Naturali*, *31*. https://doi.org/10.1007/s12210-020-00875-0

Hemingway, D., Iess, L., Tadjeddine, R., & Tobie, G. (2018). The interior of Enceladus. https://doi.org/10.2458/azu_uapress_9780816537075-ch004

Konopliv, A. S. et al. (2014). The Vesta gravity field, spin pole and rotation period, landmark positions, and ephemeris from the DAWN tracking and optical data. *Icarus*, *240*. https://doi.org/https://doi.org/10.1016/j.icarus.2013.09.005

Konopliv, A. et al. (2018). The ceres gravity field, spin pole, rotation period and orbit from the DAWN radiometric tracking and optical data. *Icarus*, *299*, 411–429. https://doi.org/https://doi.org/10.1016/j.icarus.2017.08.005

Lainey, V. et al. (2021). Mars moon ephemerides after 14 years of Mars EXpress data. *Astronomy & Astrophysics*. https://doi.org/https://doi.org/10.1051/0004-6361/202039406

LeMaistre, S., Rivoldini, A., & Rosenblatt, P. (2019). Signature of Phobos interior structure in its gravity field and libration. *Icarus*, *321*, 272–290. https://doi.org/https://doi.org/10.1016/j.icarus.2018.11.022

Lissauer, J. J., & de Pater, I. (2013). *Fundamental planetary science: Physics, chemistry and habitability*. Cambridge University Press.

McMahon, J. W., Scheeres, D. J., Hesar, S. G., Farnocchia, D., Chesley, S. R., & Lauretta, D. S. (2018). The osiris-rex radio science experiment at Bennu. *Space Science Reviews*, *214*, 1–41.

Miller, J. et al. (2002). Determination of shape, gravity, and rotational state of asteroid 433 Eros. *Icarus*, *155*(1), 3–17. https://doi.org/https://doi.org/10.1006/icar.2001.6753

Nallapu, R. et al. (2020). Trajectory design of perseus: A cubesat mission concept to Phobos. *Aerospace*, *7*(12), 1–31. https://doi.org/10.3390/aerospace7120179

Pail, R., Goiginger, H., Mayrhofer, R., Höck, E., Schuh, W.-D., & Brockmann, J. (2010). GOCE gravity field model derived from orbit and gradiometry data applying the time-wise method, 1–1.

Pajola, M. et al. (2013). Phobos as a d-type captured asteroid, spectral modeling from 0.25 to 4.0μm. *The Astrophysical Journal*, *777*, 127. https://doi.org/10.1088/0004-637X/777/2/127

Pätzold, M. et al. (2014). Phobos mass determination from the very close flyby of Mars EXpress in 2010. *Icarus*, *229*, 92–98. http://www.sciencedirect.com/science/article/pii/S0019103513004508

Pieters, C. (2010). Compositional implications of the color of Phobos. *First Moscow solar system symposium*, *123*, 43 (abstract).

Pushparaj, N., Baresi, N., Ichinomiya, K., & Kawakatsu, Y. (2021). Transfers around Phobos via bifurcated retrograde orbits: Applications to Martian moons exploration mission. *Acta Astronautica*, *181*, 70–80. https://doi.org/https://doi.org/10.1016/j.actaastro.2021.01.016

Rosenblatt, P. (2011). The origin of the Martian moons revisited. *Astron Astrophys Rev*, *19*. https://doi.org/https://doi.org/10.1007/s00159-011-0044-6

Rummel, R., Yi, W., & Stummer, C. (2010). GOCE gravitational gradiometry. *Journal of Geodesy*, *85*, 777–790. https://doi.org/10.1007/s00190-011-0500-0

Safranov, V. S., Pechernikova, G. V., Ruskol, E. L., & Vitjaev, A. V. (1986). Protosatellite swarms. *Satellites* (pp. 89–116). University of Arizona Press. http://www.jstor.org/stable/j.ctv1v3gr3r.7

Scheeres, D. (2012). *Orbital motion in strongly perturbed environments*. Springer.

Scheeres, D., Van wal, S., Olikara, Z., & Baresi, N. (2019). Dynamics in the Phobos environment. *Advances in Space Research*, *63*(1), 476–495. https://doi.org/https://doi.org/10.1016/j.asr.2018.10.016

Siemes, C. (2008). *Digital filtering algorithms for decorrelation within large least squares problems* (PhD dissertation). University of Bonn.

Siemes, C., Rexer, M., & Haagmans, R. (2019). GOCE star tracker attitude quaternion calibration and combination. *Advances in Space Research*, *63*(3), 1133–1146. https://doi.org/https://doi.org/10.1016/j.asr.2018.10.030

Trimeche, A. et al. (2019). Concept study and preliminary design of a cold atom interferometer for space gravity gradiometry. *Classical and Quantum Gravity*, *36*(21). https://doi.org/10.1088/1361-6382/ab4548

Usui, T. et al. (2020). The importance of Phobos sample return for understanding the Mars-moon system. *Space Science Reviews*, *216*(4). https://doi.org/10.1007/s11214-020-00668-9

W., S. (2018). Tailored numerical solution strategies for the global determination of the Earths gravity field. *Mitteil Geod Inst TU Graz*, *81*, 156.

Willner, K. et al. (2014). Phobos' shape and topography models. *Planetary and Space Science*, *102*, 51–59. https://doi.org/https://doi.org/10.1016/j.pss.2013.12.006

Witasse, O. et al. (2014). Mars EXpress investigations of Phobos and Deimos [Phobos]. *Planetary and Space Science*, *102*, 18–34. https://doi.org/https://doi.org/10.1016/j.pss.2013.08.002

Yang, X. et al. (2019). The low-degree gravity field of Phobos from two Mars EXpress flybys. *European Planetary Science Congress (EPSC-DPS Joint meeting)*, *Vol. 13*, EPSC-DPS2019–1521. https://hal.archives-ouvertes.fr/hal-03155678